BILINGUAL
PUBLISHING CO.
Pioneer of Global Academics Since 1984

02

Journal of Metallic Material Research

Volume 3 | Issue 2 | 2020 October | ISSN 2630-5135 (Online)

BPC
BILINGUAL
PUBLISHING CO.
Pioneer of Global Academics Since 1984

Editor-in-Chief

Dr. Oleg Valentinovich

Sobol, Ukraine

Editorial Board Members

Shuo Chen, United States
Changrui Wang, China
Recep Karadag, Turkey
Madhukar Eknath Navgire, India
Unal Camdali, Turkey
Jitendra Kumar Singh, Korea
Abhay Nanda Srivastva, India
Vivek Patel, India
Aybaba Hançerlİoğullari, Turkey
Bandar Abdulaziz AlMangour, Saudi Arabia
Soumen Maiti, India
Jonathan David Parker, Canada
Jingyuan Yan, United States
Satyanarayana Sirasani, India
Xiaoan Hu, China
Derya Dispinar, Turkey
Samson jerold samuel Chelladurai, India
Akash Deep Sharma, India
Dan Dobrotă, Romania
Asit Kumar Gain, Australia
Dragica Milan Minic, Serbia
Zabiollah Mahdavifar, Iran
Chandan Pandey, India
Mahnaz Mahdavi Shahri, Iran
Janarthanan Gopalakrishnan, India
Deniz Uçar, Turkey
Weidong Song, China
Attoui Aissa, Algeria
Mohammad Farnush, Iran
Qiaoli Lin, China
Hajar Zarei Se Dehi Zadeh, Iran
Subravel Visvalingam, India
Asaminew Abiyu Cherinet, Ethiopia
Arif Gök, Turkey
Ning Li, China
Fufa Wu, China
Wenchun Jiang, China
Saeed Zeinali Heris, Iran
Himadri Bhusan Sahoo, India
Vladimir Victorovich Lukov, Russian Federation
Abhishek Ghosh, India
KangHua Chen, China
Pradeep L Menezes, United States
Shuhua Zhang, China
Naushad Ahmad, India
S Selvam, India
Guocheng Zhu, China
Mohamed Kamal ElFawkhry, India
Mohammad Hassan Shirani Bidabadi, China
Mohd Azli Salim, Malaysia
Vladimir Mikhailov Yegorovich, Russian Federation
Kaveh Sheikhi Moghaddam, Iran
Robin Gupta, India
Sergey Vasilevich Byvaltsev, Russian Federation
Nitin Saini, India
Ramesh Balakrishnan, India
Alexander Evgenievich Barmin, Ukraine
Khitam Abdulhussein Saeed, Malaysia
Sertan Ozan, Turkey
Anand Krishnan, South Africa
Farshad Darab-Golestan, Iran
Mohammadreza Elahifard, Iran
Paparao Mondi, India
Zbigniew Ranachowski, Poland
Sami ullah Rather, Saudi Arabia
Nickolaj Nikolayevich Rulyov, Ukraine
Oğuzhan Keleştemur, Turkey
Shengqiang Ma, China
Md Saiful Islam, Bangladesh
Ajay Kumar Choubey, India
Saeed Kakaei, Iran
Hojat Jafari, Iran
Yuhan Liang, United States
Ahmed Wagih, Egypt
Bhanodaya Kiran Babu Nadikudi, India
Rong Liu, Canada
Mahmoud Pakshir, Iran
Changhai Zhou, China
Vishal Ishvarbhai Lad, United States
Hossein Ghasemi Mobtaker, Iran
Francesco Caridi, Italy
Konstanti Viktorovich Ivanov, Russian Federation
Dipak Kumar, India
Americo Scotti, Brazil
Ziad Salem Abu-Hamatteh, Jordan
Mohsen Vafaeifard, Malaysia
Hülya - Demirören, Turkey
Tahir Mohiuddin Bhat, India
Hamit Özkan Gülsoy, Turkey
Sandhya Dwevedi, India
Sergey Nikolaevich Lezhnev, Kazakhstan
Faysal Fayez Eliyan, Canada
Shouxun Ji, United Kingdom
Patrice Berthod, France
Moslem Mansour Lakouraj, Iran
Akhyar - Akhyar, Indonesia
Chih-Chun Hsieh, Taiwan
Recep Sadeler, Turkey
Lutfiddin Omanivich Olimov, Uzbekistan
Mahmoud Ebrahimi, Iran
Lineker Max Goulart Coelho, Brazil
Aslıhan Katip, Turkey
Serkan ISlak, Turkey
Murat Sarıkaya, Turkey
Yaofeng Chang, United States
Mehmet Kaya, Turkey
Yahya Absalan, Russian Federation
Xiang Wang, China
Meilinda Nurbanasari, Indonesia
Rizk Mostafa Shalaby, Egypt
Anatolii Michailovich Lepikhin, Russian Federation

Volume 3 Issue 2 • October 2020 • ISSN 2630-5135 (Online)

Journal of Metallic Material Research

Editor-in-Chief

Dr. Oleg Valentinovich

BILINGUAL
PUBLISHING CO.
Pioneer of Global Academics Since 1984

BILINGUAL PUBLISHING CO.
Pioneer of Global Academics Since 1984

Volume 3 | Issue 2 | October 2020 | Page 1-53
Journal of Metallic Material Research

Contents

Article

Review

Copyright

Journal of Metallic Material Research
https://ojs.bilpublishing.com/index.php/jmmr

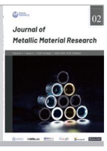

ARTICLE

The Study on the Corrosion Behaviour of Welded and Unwelded Medium Carbon Steel in Sodium Chloride (Nacl) Solutions

Cyril Ocheri[1*] **Hebert. A. Obiorah**[1] **Romanus Egwuonwu Njoku**[1] **Nnaemeka Anthony Urama**[1] **Joseph Babalola Agboola**[2] **Christopher Nwankwo Mbah**[3] **Johnson Nwaemezie Ezeanyanwu**[3] **Chikezie Walter Onyia**[3]

1. Department of Metallurgical and Materials Engineering, University of Nigeria, Nsukka
2. Department of Metallurgical and Materials Engineering, Federal University of Technology, Minna, Niger State
3. Department of Metallurgical and Materials Engineering, Enugu State University of Science and Technology, Enugu

ARTICLE INFO

Article history
Received: 18 September 2019
Accepted: 29 September 2019
Published Online: 31 October 2020

Keywords:
Corrosion behaviour
Welded
Un-welded
Medium carbon steel
Sodium chloride solution

ABSTRACT

The research work was based on the study of the corrosion behaviour of the welded and un-welded medium carbon steel in sodium chloride solutions. The Sodium chloride solutions used are 1ml, 2ml, 3ml and 4ml for both welded and un-welded medium carbon steel in NaCl. The experiments were conducted in two ways, the weight loss analyses of measurements and using the electrochemical analyzer workstation to determine the potential dynamic of the samples. The samples for the weight loss measurements were prepared from rolled products obtained at the foundry shop. Two medium carbon steel materials were sourced with different chemical compositions as sample A and B. The materials were prepared to accommodate the experiments for the determination of welded and un-welded medium carbon steel. A total of sixty-eight (68) samples were produced, prepared and used for the weight loss measurements /analyses the experiments. Thirty-four of the samples each were prepared for both the welded and un-welded experiments. All the samples were produced and prepared through the use of various machining processes with the use of a lathe machine for planning, milling. Thirty-four (34) of the sample preparation were further welded in readiness of the experiments. Sixty -eight breakers were sourced for and used. Ten (10) other samples were used for the determination with the use of the electrochemical analyzer. The chemical compositions of the medium carbon steel were determined with the use of SPECTRO Analytical Instruments. A metallurgical inverted optical microscope was used to determine the microstructures of the materials. The Scanning Electron Microscopy with EDS was used to determine the morphologies of the materials. The thirty-four of the samples were welded this process was performed to determine the effects of welding on the material surrounding the weldments. These materials were made into sizes with the use of power hacksaw (i.e. 2cm by 2cm). Other materials were prepared to 1cm x 1cm thickness from the same materials. The Tafel plot experiments and that of the open Circuit Potential Time (OCPT) were carried out with the use of Electrochemical Analyzer/ Workstation. The Medium carbon steel materials were exposed for fifty-four (54) days, with an interval of 3days. The corrosion rates analyses were determined and the graphs of the corrosion rates (mm/yr.) and other parameters were used plotted against No of days exposed.

**Corresponding Author:*
Cyril Ocheri,
Department of Metallurgical and Materials Engineering, University of Nigeria, Nsukka;
Email: cyril.ocheri@unn.edu.ng

DOI: https://doi.org/10.30564/jmmr.v3i2.2400

1. Introduction

The tendency of a metal to revert to its native state (or) Metallurgy in reverse, the chemical or electrochemical reaction between a material and its environments that produces a deterioration of the material and its deterioration properties. The destructive attack of a material by reaction with its environment, corrosion of metals is the commonest electrochemical phenomenon encountered in day phenomenon day to day life. Corrosion is the degradation of materials by electrochemical or chemical reaction with its environment. It is also an electrical circuit process where the exchange of electrons is conducted by a chemical reaction in part of the circuit. The chemical reactions occur at the surface of the metal exposed to the electrolyte. Oxidation reactions occur at the surface of the anode and reduction reaction occurs at the surface of the cathode [1]. Metals corrode because they are used in an environment where they are chemically unstable. Only copper and precious metals (gold, silver, platinum, etc.) are found in nature in their metallic state. All the other metals, to include iron, the metal are most commonly used and are processed from minerals or ores into metals which are inherently unstable in their environment [2].

Corrosion allows the pipes and other metallic and associated components to degrade and deteriorate steadily both internally and externally. It can reduce materials' life span by gradually chewing the thickness wall up. Under such circumstances, it could be as short as five years for the decline to cause certain metallic materials to fail [14]. Corrosion may also result in the pipe being encrusted, reducing the pipe's carrying capacity to a point that it needs to be replaced to provide the necessary flow [3,4]. However, like any engineering structure, the best-designed and maintained metallic materials will become defective as it progresses through it design life. One of the major causes of metallic defects around the world is corrosion [5]. The selection of materials for a particular situation is dependent on the materials that may pass through or been used for. In the case of metallic materials made to pipe, in such situation, liquid and gasses may be allowed to pass through the device. In such a scenario, the pressure is allowed to move through and the temperature of the contents. Metallic materials are made from various types of materials to meet precise and stringent requirements with regard to the desired service. Due to its strength, ductility, weldability, the most widely used material for the manufacture of petroleum pipelines is mild steel or medium carbon steel and is suitable for heat treatment with varying mechanical properties [6]. However, carbon steel quickly corrodes when exposed to pure air due to all the common structural metals from surface oxide films, but the oxide produced on carbon steel is ready to be broken down and is not fixed in the presence of moisture [7].

However, despite the current level of industry knowledge, most metallic materials continue to experience a modest but significant number of failure due to corrosion at its weld and entire point. The explanation for this is that the corrosion behaviour of materials such as pipes buried under the earth is much more complex than that of piece steel in a saltwater beaker [8].

Metallic materials built into pipelines play an incredibly important role worldwide as a means of transporting gases and liquids to the ultimate users over long distances from their sources. The general public is not aware of the number of pipelines which as a primary means of transportation are continually in services. A buried operating pipeline is very unobtrusive and seldom makes it present when transportation fluids are constructed with carbon steel materials. This is because metallic materials such as pipes have to be sturdy enough to withstand various conditions that are primarily due to temperature, pressure and fluid [6]. Medium steels can be categorized according to [9].

2. Medium-Carbon Steels

The medium-carbon steels have carbon concentrations between about 0.25 and 0.60 wt. %. These alloys may be heat treated by austenitizing, quenching, and then tempering to improve their mechanical properties. They are most often utilized in the tempered condition, having microstructures of tempered martensite. The plain medium-carbon steels have low hardenabilities and can be successfully heat-treated only in very thin sections and with very rapid quenching rates. Additions of chromium, nickel, and molybdenum improve the capacity of these alloys to be heat-treated, giving rise to a variety of strength-ductility combinations.

These heat-treated alloys are stronger than the low-carbon steels but at a sacrifice of ductility and toughness. Applications include railway wheels and tracks, gears, crankshafts, and other machine parts and high-strength structural components calling for a combination of high strength, wear resistance, and toughness [6].

3. Materials and Methods

3.1 Materials

The material used in this research work is a medium Carbon Steel produced at the Light Section Mill of the

DOI: https://doi.org/10.30564/jmmr.v3i2.2400

Ajaokuta Steel Company Limited, Ajaokuta, Kogi State, Nigeria. The chemical compositions of the materials were determined using SPECTRO Analytical Instruments at the Quality Control and Materials Analysis of the Foundry shop section of the Steel Plant. The chemical compositions of the two sourced materials are shown in table 1 and 2 tagged as samples A and B.

Figure 1. SPECTRO Analytical Instruments used for the determination of chemical compositions of Medium Carbon Steel

3.2 Equipment

The equipment used for this research work includes table lathe machine, table vice, bench grinder, electric arc welding machine, polishing machine, digital weighing balance, digital multi-meter, pH meter, and SPECTRO Analytical Instruments and Electrochemical Analyzer workstation.

3.3 Chemical Reagents

Chemical reagents used include sodium chloride, Distilled water.

3.4 Materials Preparation

3.4.1 Welding Operation

The 10mm thickness medium steel was cut by a hacksaw to 2cm by 2cm. Thirty-four (34) of such samples were prepared for the welded and un-welded samples. The types of joints were adopted, which include; Butt joint. Out of the (68) samples of 10mm thickness that was researched on, thirty-four (34) samples were welded, while the remaining thirty-four (34) for un-welded samples including some numbers that were used as the received control samples. All the thirty-four (34) samples of 10mm were abutted leaving a gap of 3 mm between them when the gap was fully filled with welded melt using the same 3.0 mm welding electrode and 2.5 mm welding gages at 12.5A welding current and at the same 70V welding voltage. This experiment was carried out in which the test materials were combined with gas welding, paying attention to the welding pool and the heat-affected gas welding zone.

3.4.2 Gas Welding

The welding operations were performed using oxy-acetylene gas that was held at a temperature of approximately 2200-2400ºC with a heat power of approximately 54-56mg / m^3. The electrode holder was connected to one terminal of the power source via a welding cable, and the work piece was connected to another terminal of the power source via a second cable. The heart of the coated electrode, the heart wire, conducts the electrical current to the arc and provides filler metals for the joint, the top 1.5 cm of the core wire was bare and retained by the electrode holder for electrical contact. The electrode holder was basically a metal clam with an outer shell that was electrically shielded to keep the welder secure.

3.4.3 Arc Welding

In Arc welding, the sample sizes of the test materials used in gas welding were also used. Using the same operation but the only difference being that the same electrode was used instead of an acetylene gas, and electric current. The version of your electrode is a 3.0 version of the electrode used for carbon steels. The welded samples were allowed to cool and hammer-tipped to remove the slag in order to reveal if the gap is totally filled

3.4.4 Preparation of Sample for Corrosion Test

The samples used for general corrosion studies were medium carbon steel with a thickness of 10 mm and were cut into various sizes of 2cm by 2 cm by power hacksaw. These samples were ground and polished by using emery papers to remove the rust particles on the test materials. A total of sixty-eight (68) specimens were used in all as shown in the table below.

Table 1. Shows Sample A: the chemical compositions of the sourced Medium Carbon Steel

Average	**%C**	**%Si**	**%Mn**	**%P**	**%S**	**%Cr**	**%Ni**	**%Mo**
$\bar{x}$	0.335	0.307	0.82	0.0061	0.0081	0.080	0.102	0.038
	%Al	%Cu	%Co	%Ti	%Nb	%V	%W	%Pb
$\bar{x}$	0.036	0.178	0.0085	0.0003	0.0054	0.0016	<0.0001	<0.0001
	%B	%Sn	%Zn	%As	%Bi	%Ca	%Ce	%Zr
$\bar{x}$	0.0007	0.0063	0.0042	0.0005	0.0010	0.0010	0.0023	0.0006
	%La	%Fe						
$\bar{x}$	<0.0001	98.3						

Table 2. Shows Sample B: the chemical compositions of the sourced Medium Carbon Steel

Average	%C	%Si	%Mn	%P	%S	%Cr	%Ni	%Mo
$\bar{x}$	0.347	0.276	1.3	0.027	0.0043	0.015	0.036	<0.0001
	%Al	%Cu	%Co	%Ti	%Nb	%V	%W	%Pb
$\bar{x}$	0.033	0.015	0.0013	0.001	0.042	0.0007	<0.0001	<0.0001
	%B	%Sn	%Zn	%As	%Bi	%Ca	%Ce	%Zr
$\bar{x}$	0.0006	0.0008	0.0021	<0.0001	0.001	0.0018	0.0019	0.0002
	%La	%Fe						
$\bar{x}$	<0.0001	98.1						

Table 3. Shows: The Identification and Description of Test Pieces in the solution of various Concentrations

S/No	Sample	Concentration Solution 1ml, 2ml, 3ml and 4ml of NaCl
1	Parent material	
2	Weld assembly for gas welding	
3	heat-affected zone for gas welding	
4	weld pool for gas welding	
5	weld assembly for arc welding	
6	weld pool for arc welding	
7	heat-affected zone arc welding	
8	Electrochemical Analyzer CHI600	Open Circuit Potential Time (OCPT), Tafel plots

3.4.5 Preparation of Solutions and Testing for the Corrosion

(a) The NaCl solutions were prepared using distilled water. The Electrochemical Analyzer was used for the determination of the corrosion tests. About 20ml of distilled water in volume was poured a big conical flask. These solutions were put into sixty -eight (68) small plastic beakers for the weight loss experiments. The processes were determined for 54 days at an interval of 3 days. The other experiments for the determination of the corrosion rate, log (iA) Currents and potentials etc., were performed with the aid of the Electrochemical Analyzer. The solutions were prepared as stated below in table 4.

Table 4. Sample preparation and methods of analyses

S/NO	Sample	Sample Size	Materials	Concentration	Remarks
1	A	10mm	Welded	Control sample 1-4 ml	Weight Loss
2	B	10mm	Un-welded	Control Sample 1-4 ml	Weight Loss
3	A	1cm x 1cm	Welded	The control sample, 1-4 ml	Electrochemical Analyzer
4	B	1cm x1cm	Un-welded	Control Sample 1-4 ml	Electrochemical Analyzer

The medium carbon steel rod of the thickness of 16mm by 12mm and length of 45mm by 6mm thickness was obtained from Light section Mill of the Ajaokuta Steel Company Limited, Ajaokuta, Kogi State, Nigeria. The materials were thoroughly clean and taken to the lathe machine for removing unwanted parts until the sample sizes were 10mm in thickness for both the welded and un-welded. The materials were cut into the required sizes with the use of a cutting disc to 10mm x 10mm for all the samples. A total of sixty-eight (68) samples were prepared in all for the experiments performed for weight loss measurement/analyses. Sixty-eight beakers were used for these experiments. Each of the beakers contained various quantities of Sodium Chloride (NaCl) solutions [12]. Each of the prepared samples was properly labelled for proper identification. During the cause of the experiments, both materials were kept side by side with reference to the welded and un-welded samples. The experiments were conducted for fifty-four (54) days. Before the experiments commenced all the weights of the samples were taken with the aid of a digital weighing balance. The immersed sample materials were removed from the sodium chloride at an interval of three (3) and the new weights were taken with the same weighing balance. The differential in the initial and final weights was used for the determination of corrosion rate measured in mm/yr.

3.4.6 Characterization of Medium Carbon Steel

Metallographic analyses took place with the use of Optical Microscopy at Material Science Laboratory, in the Department of Metallurgical and Materials Engineering, University of Nigeria Nsukka, the SEM and EDS analyses were carried out in South Africa. Below are the results of the analyses:

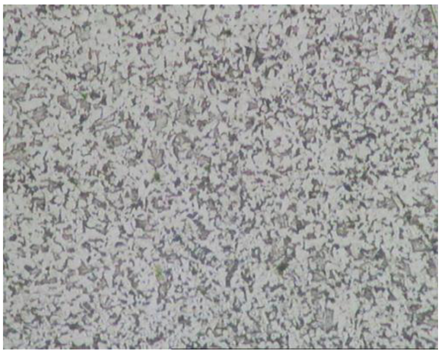

Figure 2. Optical micrograph of Medium Carbon Steel

From the micrograph of figure 2 above, it can be seen that the parent material contains ferrites and cementite. The ferrites are more compared to cementite which shows that cementite will corrode first before the ferrites.

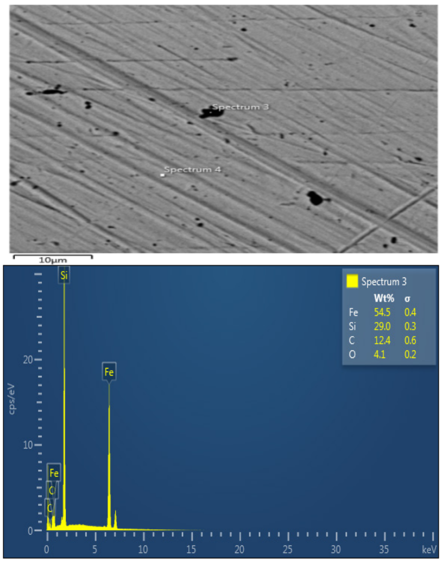

Figure 3. SEM/EDS for parent material

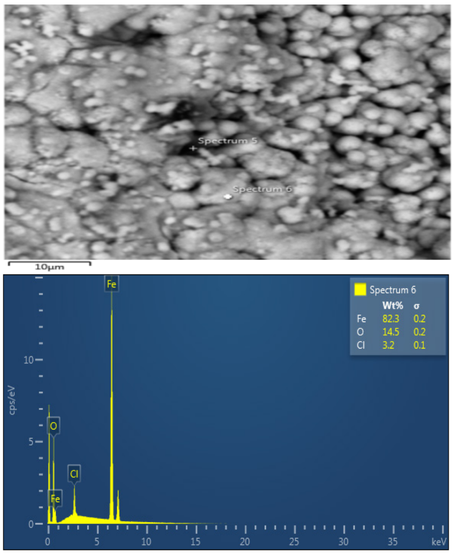

Figure 4. SEM/EDS for the control Sample A

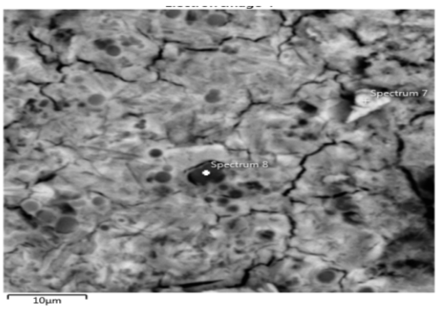

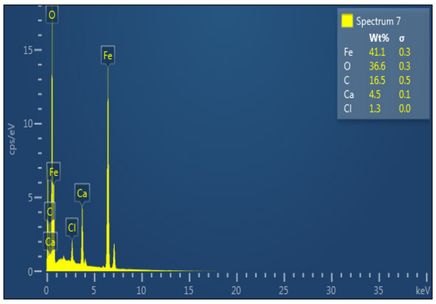

Figure 5. SEM/EDS for coupon Sample A of medium carbon steel immersed in NaCl on 4ml

From the above micrograph of Figure 1, it indicates that the parent material contains ferrites and cementite. The ferrites compared to cementite, which shows that cementite will corrode first before the ferrites.

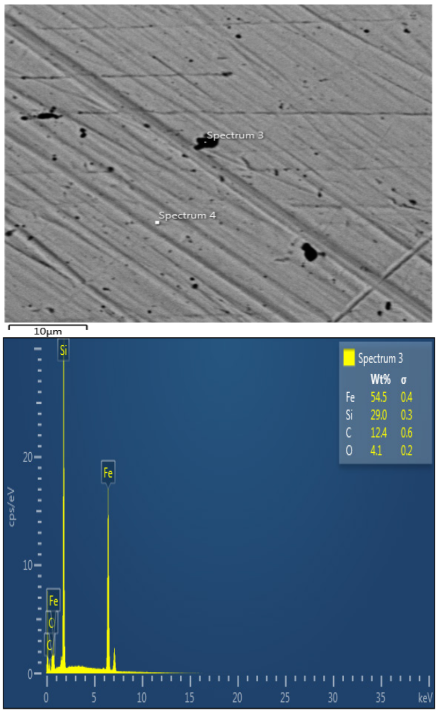

Figure 6. SEM/EDS for parent material

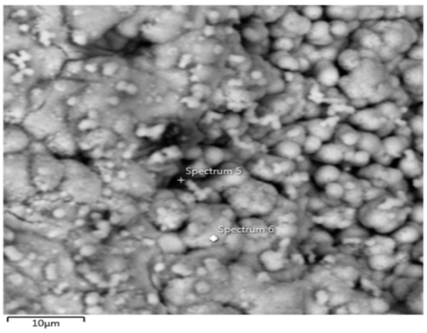

DOI: https://doi.org/10.30564/jmmr.v3i2.2400

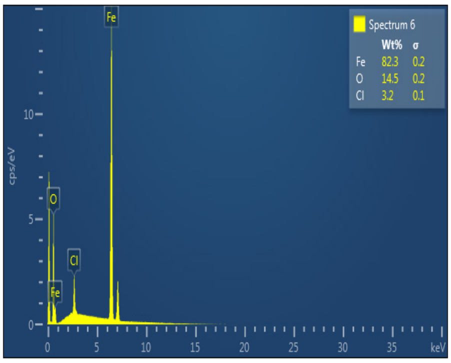

Figure 7. SEM/EDS for the control Sample B

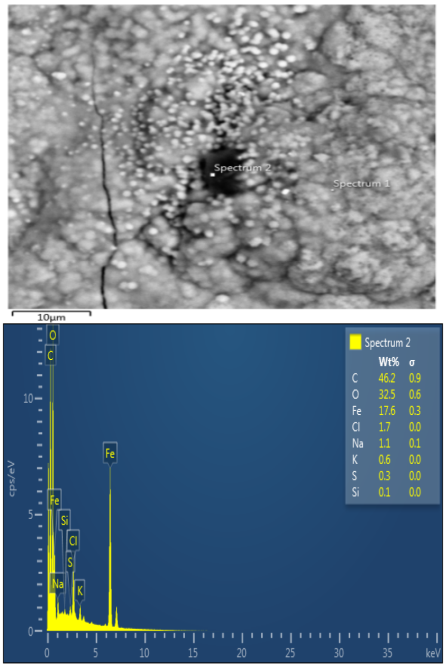

Figure 8. SEM/EDS for coupons for Sample B immersed in NaCl for 6 days on 4ml for un-welded Medium carbon steel

The optical microscopic examination, SEM/EDS for the parent material (coupon) viewed and discovered that iron was the major element present in the sample. These tests took 9 days before the morphological analyses. The sample with 4ml of welded materials shows that there was cathodic protection, which shows there was an increase in carbon content than that of the iron in the parent material. That is, the iron, which was 100wt%, reduced from 100 to 17.6wt% and carbon with 12.4wt% increased to 46.2wt%. These results show that the protection took place on the carbon whereas iron was degraded.

3.5 Corrosion Monitoring

Weight loss: The surface area mass of all specimens used for this was measured before immersion into a different solution. At every 3days interval, the immersion samples were collected, kept with the aid of a spatula within a bowl of water and with two white ankles to extract any corrosion products that may have come into contact with the test material. The specimens were then weighted digitally to achieve weight loss as part of the corrosion result in the setting under analysis. The calculation of corrosion rate was determined using the form below. Calculation of Corrosion Rate

The average corrosion rate may be obtained as follows:

$$Corrosion\ Rate = \frac{K\,x\,W}{A\,x\,T\,x\,D}[13]$$

Millimeters per year (mm/yr.) 8.76 x 10^4

Where K is a constant (varies with the unit)

T is the time of exposure in hours to the nearest 0.01 h, A is the area in cm to the nearest 0.01 cm^2t

W is the mass loss in grams to the nearest 1 mg g

D is the density in g/cm. D cm3

Several units are used to express corrosion rates s rates

Using the above-mentioned units for T, A, W, and D, the corrosion rate can be calculated in a variety of units, with an appropriate value of K

Millimeters per year (mm/yr) 8.76 x 10^4

$$Corrosion\ Rate = \frac{Weight\ Loss\,(CR)}{\frac{A\,x\,T}{365}} ----- Equation\ 3.2\ [10]$$

W = Weight loss (mg)

A = Total Surface area (mm^2)

$$\frac{T}{365} = Exposure\ time\ in\ days\ extrapolated\ to\ a\ year$$

A = $2\Pi^2 1$

Where

L is the length (mm)

R = radius (mm)

(b) Weight Loss Measurement

The experiments with 1ml-4 ml NaCl solutions took a period of 54 days. The Medium carbon steel on welded joints was used in the corrosion environment for the testing corrosion safety efficiency. The optical multi-meter (model 84280) was used to examine the weight loss of the samples in the sodium chloride atmosphere at an interval of three (3days). The obtained values were converted to a saturated calomel electrode (SCE) values using the following relation:

$E_m V$(SCE)=E_{zin} -1030… Equation (3.1), where 1030 is a constant value.

4. Results and Discussion

4.1 Results

The values and data generated from the weight loss measurement/ analyses tabulated from table 4.1 to 4.8. It could be seen that each data are specifically for welded and un-welded samples Nevertheless, tables 4.1 to 4.4 are located to welded samples, while tables 4.5 to 4.8 are located to un-welded samples. Also figures 9- 13 shows the description and distributions of the analyses various parameters with the no of days for A1-10mm samples of welded medium carbon steel immersed in 1 ml of sodium chloride solution. A similar trend was observed of figures 14 -18 shows the description and distributions of the analyses various parameters with the no of days for B1-10mm samples of welded medium carbon steel immersed in 2 ml of sodium chloride solution. Also figures 19-23 followed the pattern shown description and distributions of the analyses various parameters with the no of days for A1-10mm samples of welded medium carbon steel immersed in 3 ml of sodium chloride solution and figures 24- 28 shows the same trend for the description and distributions of the analyses various parameters with the no of days for A1-10mm samples of welded medium carbon steel immersed in 4 ml of sodium chloride solution. Also figures 29- 33 shows the description and distributions of the analyses various parameters with the no of days for A1-10mm samples of un-welded medium carbon steel immersed in 1ml of sodium chloride solution. A similar trend was observed of figures 34 -38 shows the description and distributions of the analyses various parameters with the no of days for B1-10mm samples of un-welded medium carbon steel immersed in 2 ml of sodium chloride solution. Also figures 39-43 followed the pattern shown description and distributions of the analyses various parameters with the no of days for A1-10mm samples of un-welded medium carbon steel immersed in 3 ml of sodium chloride solution and figures 44- 48 shows the same trend for the description and distributions of the analyses various parameters with the no of days for A1-10mm samples of un-welded medium carbon steel immersed in 4 ml of sodium chloride solution.

Table 4.1 A1- 10mm samples welded immersed in 1ml NaCl

No of days	Initial weights g	Final weights g	Weight loss g	Cumulative weight loss g	Corrosion rate g/cm^2/yr	Potential (mV)	pH
1	26.94	26.94	0	0	0	-488	7.35
4	26.94	26.93	0.006	0.006	0.359	-726	7.66
7	26.93	26.93	0.002	0.007	0.236	-755	7.89
10	26.93	26.92	0.011	0.018	0.208	-712	8.19
13	26.92	26.91	0.011	0.029	0.252	-686	7.45
16	26.91	26.9	0.008	0.037	0.215	-703	7.11
19	26.9	26.89	0.008	0.044	0.178	-621	7.31
21	26.89	26.89	0.006	0.05	0.085	-532	8.7
24	26.89	26.87	0.014	0.064	0.065	-710	7.8
27	26.87	26.86	0.015	0.079	0.079	-650	7.25
30	26.86	26.86	0.005	0.084	0.099	-735	7.1
33	26.86	26.85	0.59	0.09	0.058	-611	8.2
36	26.85	26.84	0.009	0.099	0.067	-680	8.1
39	26.84	26.84	0.007	0.105	0.088	-725	7.7
42	26.84	26.83	0.111	0.116	0.097	-740	8.1
45	26.83	26.82	0.007	0.124	0.065	-510	7.7
48	26.82	26.81	0.007	0.131	0.054	-620	8.15
51	26.81	26.8	0.009	0.139	0.035	-630	7.65
54	26.8	26.8	0.006	0.1454	0.026	-525	8.30

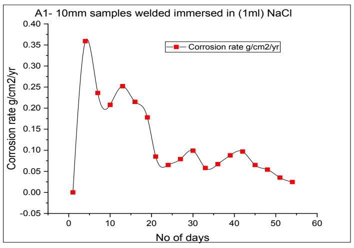

Figure 9. Weight loss g vs No of days

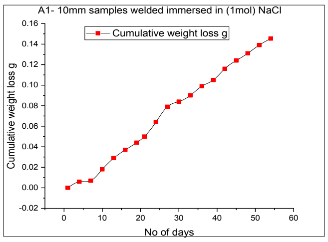

Figure 10. Cumulative weight loss g vs No of days

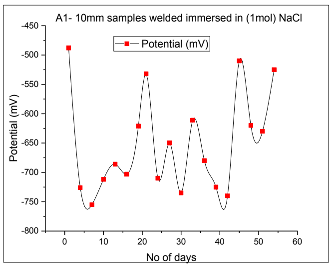

Figure 11. Corrosion rate g/cm^2/yr. vs No of days

DOI: https://doi.org/10.30564/jmmr.v3i2.2400

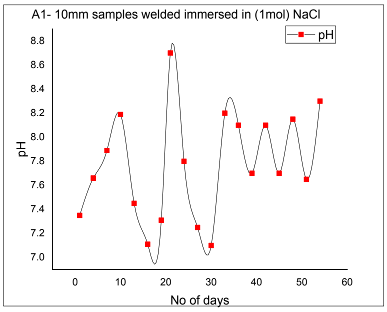

Figure 12. Potential (mV) vs No of days

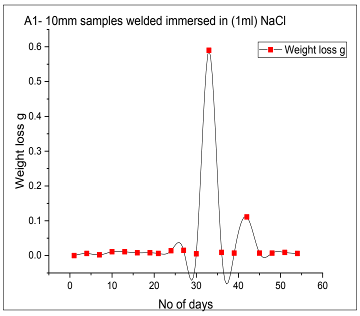

Figure 13. pH vs No of days

Table 4.2 B1- 10mm samples welded immersed in (2ml) NaCl

Nos. of days	Initial weights g	Final weights g	Weight loss g	cumulative weight loss g	Corrosion rate g/cm2/yr	Potential (mV)	pH
1	26.34	26.3361	0	0	0	-539	7.21
4	26.34	26.331	0.005	0.005	0.233	-805	8.06
7	26.33	26.3283	0.003	0.008	0.071	-395	7.64
10	26.33	26.3204	0.008	0.016	0.145	-577	8.3
13	26.32	26.3182	0.002	0.018	0.031	-790	7.35
16	26.32	263,102	0.008	0.026	0.091	-780	7.31
19	26.32	26.3085	0.002	0.028	0.016	-637	7.42
21	26.31	26.3002	0.008	0.036	0.072	-690	8.05
24	26.3	26.2965	0.004	0.04	0.028	-660	7.2
27	26.3	26.2911	0.005	0.045	0.037	-621	8.1
30	26.29	26.286	0.005	0.05	0.031	-635	8.19
33	26.29	26.28	0.006	0.056	0.033	-605	7.9
36	26.28	26.2742	0.006	0.062	0.029	-570	8
39	26.27	26.2702	0.004	0.066	0.019	-745	8.35
42	26.27	26.2662	0.004	0.07	0.017	-660	7.4
45	26.27	26.2601	0.006	0.076	0.025	-615	8.7
48	26.26	26.2554	0.005	0.081	0.018	-520	9.08
51	26.26	26.2494	0.006	0.087	0.022	-642	8.55
54	26.25	26.2419	0.008	0.094	0.025	-673	9.35

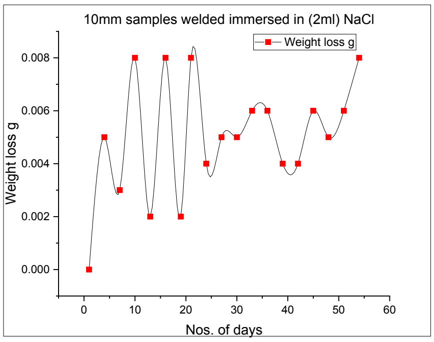

Figure 14. Weight loss g vs No of days

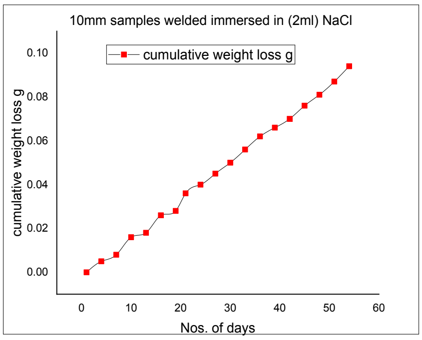

Figure 15. Cumulative weight loss g vs No of days

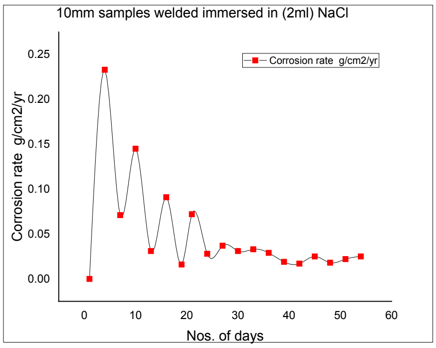

Figure 16. Corrosion rate g/cm^2/yr vs No of days

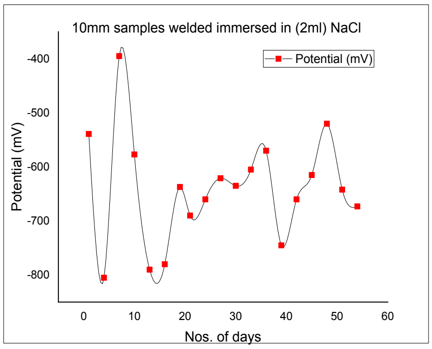

Figure 17. Potential (mV) vs No of days

DOI: https://doi.org/10.30564/jmmr.v3i2.2400

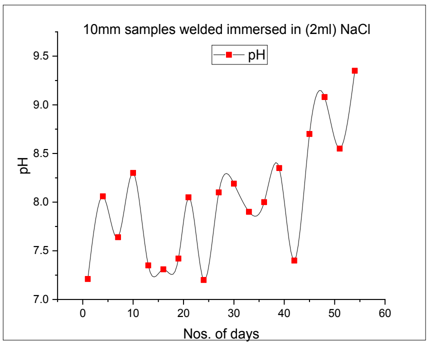

Figure 18. pH vs No of days

Table 4.3. A1- 10mm samples welded immersed in (3ml) NaCl

Nos. of days	Initial weights g	Final weights g	weight loss g	Cumulative weight loss g	Corrosion rate g/cm2/ yr	Potential (mV)	PH
1	15.32	15.32	0	0	0	-676	7.13
4	15.32	15.31	0.01	0.01	0.39	-456	7.11
7	15.31	15.31	0	0.01	0.29	-484	7.91
10	15.31	15.3	0.01	0.02	0.26	-776	7.21
13	15.3	15.3	0	0.02	0.17	-655	7.31
16	15.3	15.29	0.01	0.03	0.14	-674	7.44
19	15.29	15.29	0.01	0.03	0.05	-467	7.85
21	15.29	15.28	0.01	0.04	0.02	-678	7.36
24	15.28	15.27	0.01	0.05	0.04	-784	8.16
27	15.27	15.27	0	0.05	0.05	-657	7.64
30	15.27	15.27	0	0.05	0.03	-784	8.47
33	15.27	15.26	0.01	0.06	0.01	-467	8.09
36	15.26	15.25	0.01	0.07	0.03	-475	8.1
39	15.25	15.25	0.01	0.07	0.03	-657	7.5
42	15.25	15.23	0.01	0.09	0.03	-873	8.06
45	15.24	15.23	0.01	0.09	0.02	-674	8.24
48	15.23	15.22	0.01	0.1	0.02	-793	7.97
51	15.22	15.22	0.00	0.1	0.04	-674	7.46
54	15.22	15.21	0.01	0.10	0.02	-567	8.25

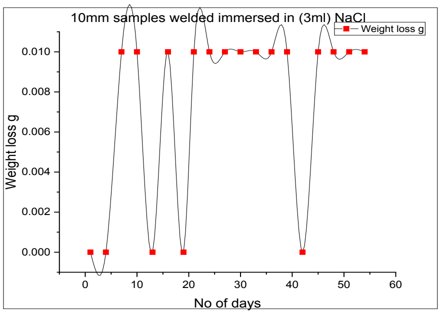

Figure 19. Weight loss g vs No of days

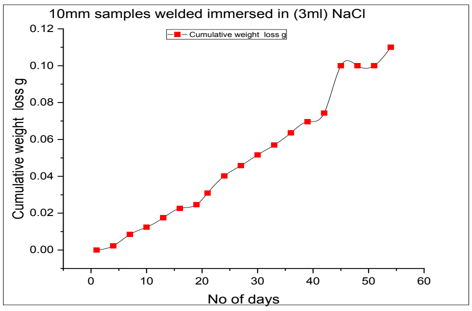

Figure 20. Cumulative weight loss g vs No of days

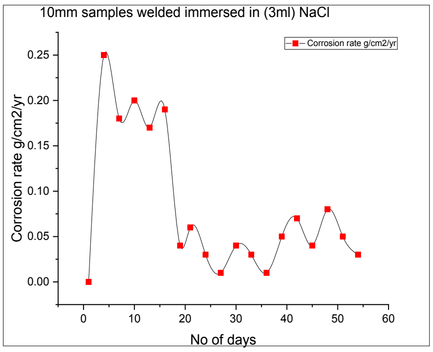

Figure 21. Corrosion rate g/cm^2/yr vs No of days

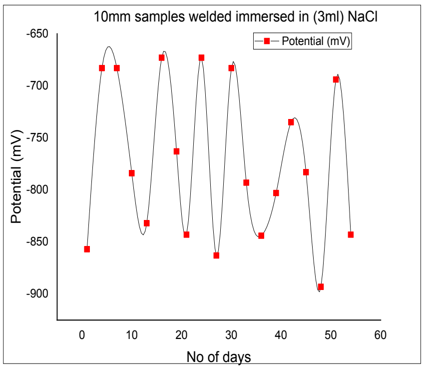

Figure 22. Potential (mV) vs No of days

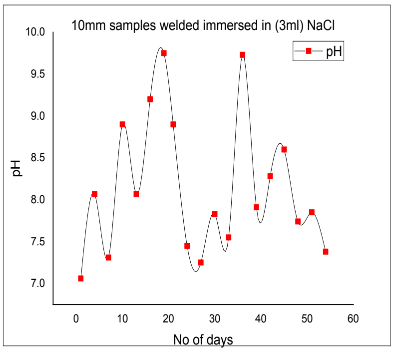

Figure 23. pH vs No of days

DOI: https://doi.org/10.30564/jmmr.v3i2.2400

Table 4.4. B1- 10mm samples welded immersed in (4ml) NaCl

No of Days	Initial weights g	Final weights g	weight loss g	Cumulative weight loss g	Corrosion rate g/cm2/yr	Potential (mV)	pH
1	21.65	21.65	0	0	0	-672	7.91
4	21.65	21.65	0	0.0018	0.37	-675	7.23
7	21.65	21.64	0.01	0.0102	0.24	-564	7.43
10	21.64	21.64	0	0.0145	0.16	-647	8.15
13	21.64	21.63	0.01	0.0205	0.19	-567	8.25
16	21.63	21.63	0	0.0235	0.04	-563	8.19
19	21.63	21.53	0	0.0266	0.03	-567	7.91
21	21.63	21.62	0	0.0302	0.03	-475	8.06
24	21.62	21.62	0	0.0335	0.03	-485	7.78
27	21.62	21.61	0.01	0.0416	0.06	-784	8.11
30	21.61	21.61	0	0.0436	0.01	-683	8.03
33	21.61	21.6	0.01	0.0496	0.04	-567	8.02
36	21.6	21.59	0.01	0.0636	0.08	-683	7.8
39	21.59	21.58	0.02	0.0807	0.09	-794	7.52
42	21.58	21.58	0	0.0827	0.01	-684	8.88
45	21.58	21.56	0.02	0.0997	0.07	-783	7.19
48	21.56	21.56	0	0.1006	0	-467	7.4
51	21.56	21.56	0	0.1037	0.01	-683	8.1
54	21.56	21.55	0.01	0.1118	0.01	-647	8.22

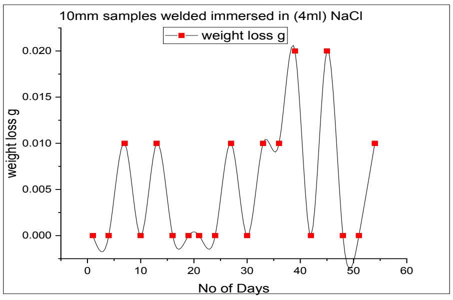

Figure 24. Weight loss g vs No of days

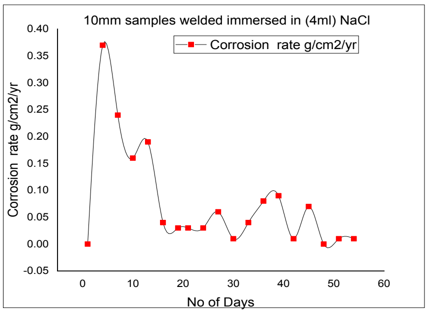

Figure 25. Cumulative weight loss g vs No of days

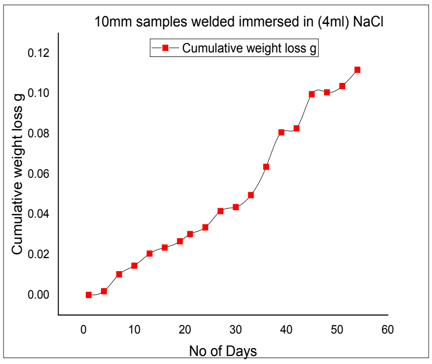

Figure 26. Corrosion rate g/cm^2/yr. vs No of days

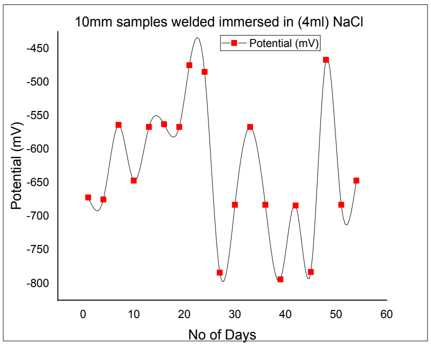

Figure 27. Potential (mV) vs No of days

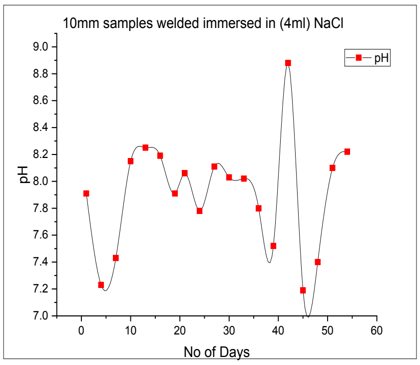

Figure 28. pH vs No of days

Table 4.5 A1- 10mm samples unwelded immersed in (1ml) NaCl

Nos. of days	Initial weights g	Final weights g	Weight loss g	Cumulative weight loss g	Corrosion rate g/cm2/yr	Potential (mV)	PH
1	15.06	15.06	0	0	0	-459	7.09
4	15.06	15.06	0.001	0.001	0.578	-465	7.13
7	15.06	15.05	0.002	0.003	0.355	-567	7.2
10	15.05	15.05	0.002	0.005	0.312	-647	7.32

DOI: https://doi.org/10.30564/jmmr.v3i2.2400

13	15.05	15.05	0.002	0.007	0.213	-563	7.25
16	15.05	15.05	0.002	0.008	0.029	-742	7.31
19	15.05	15.05	0.001	0.01	0.02	-645	7.37
21	15.05	15.05	0.003	0.012	0.024	-456	7.22
24	15.05	15.04	0.001	0.013	0.017	-598	8.1
27	15.04	15.04	0.001	0.014	0.088	-843	8.03
30	15.04	15.04	0.002	0.017	0.022	-658	7.99
33	15.04	15.04	0.002	0.018	0.038	-653	8.13
36	15.04	15.03	0.003	0.027	0.023	-793	8.08
39	15.03	15.02	0.002	0.035	0.036	-465	8.15
42	15.02	15.02	0.002	0.041	0.016	-753	7.35
45	15.02	15.01	0.005	0.046	0.033	-675	7.6
48	15.0116	15.01	0.0027	0.0484	0.034	-773	8.24
51	15.0089	15	0.0041	0.0525	0.034	-333	8.15
54	15.0048	15	0.0047	0.0572	0.029	-544	7.45

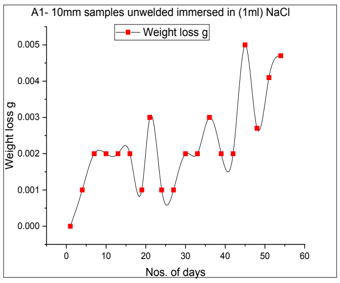

Figure 29. Weight loss g vs No of days

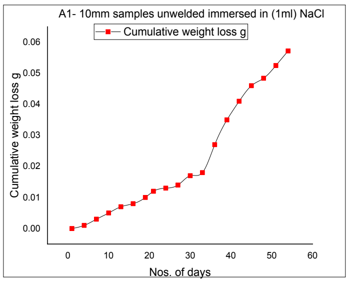

Figure 30. Cumulative weight loss g vs No of days

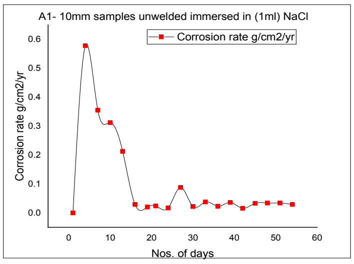

Figure 31. Corrosion rate g/cm^2/yr. vs No of days

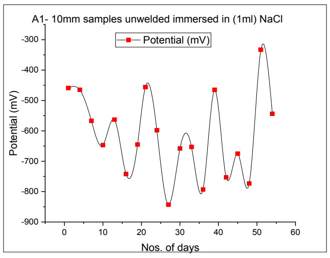

Figure 32. Potential (mV) vs No of days

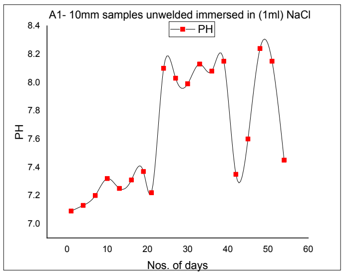

Figure 33. pH vs No of days

Table 4.6 B1- 10mm samples unwelded immersed in (2ml) NaCl

Nos. of days	**Initial weights g**	**Final weights g**	**weight loss g**	**Cumulative weight loss g**	**Corrosion rate g/cm2/ yr**	**Potential (mV)**	**PH**
1	15.32	15.32	0	0	0	-676	7.13
4	15.32	15.31	0.01	0.01	0.39	-456	7.11
7	15.31	15.31	0	0.01	0.29	-484	7.91
10	15.31	15.3	0.01	0.02	0.26	-776	7.21
13	15.3	15.3	0	0.02	0.17	-655	7.31
16	15.3	15.29	0.01	0.03	0.14	-674	7.44
19	15.29	15.29	0.01	0.03	0.05	-467	7.85
21	15.29	15.28	0.01	0.04	0.02	-678	7.36
24	15.28	15.27	0.01	0.05	0.04	-784	8.16
27	15.27	15.27	0	0.05	0.05	-657	7.64
30	15.27	15.27	0	0.05	0.03	-784	8.47
33	15.27	15.26	0.01	0.06	0.01	-467	8.09
36	15.26	15.25	0.01	0.07	0.03	-475	8.1
39	15.25	15.25	0.01	0.07	0.03	-657	7.5
42	15.25	15.23	0.01	0.09	0.03	-873	8.06
45	15.24	15.23	0.01	0.09	0.02	-674	8.24
48	15.23	15.22	0.01	0.1	0.02	-793	7.97
51	15.22	15.22	0.00	0.1	0.04	-674	7.46
54	15.22	15.21	0.01	0.10	0.02	-567	8.25

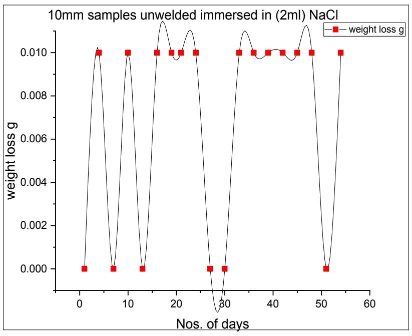

Figure 34. Weight loss g vs No of days

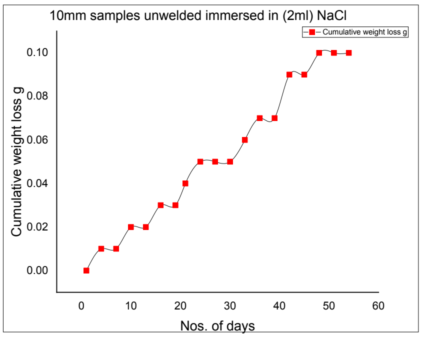

Figure 35. Cumulative weight loss g vs No of days

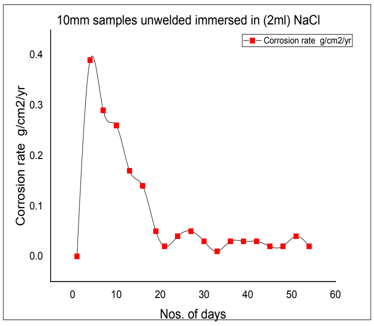

Figure 36. Corrosion rate g/cm^2/yr vs No of days

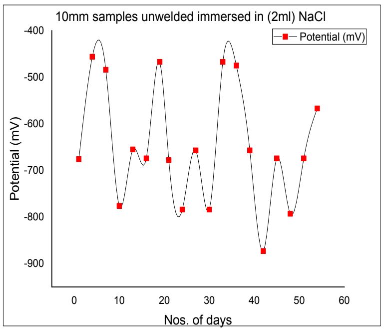

Figure 37. Potential (mV) vs No of days

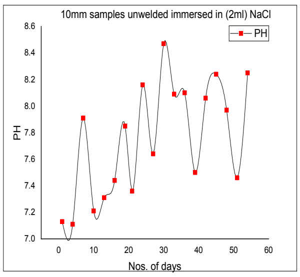

Figure 38. pH vs No of days

Table 4.7. A1- 10mm samples unwelded immersed in (3ml) NaCl

Nos. of days	Initial weights (g)	Final weights (g)	Weight loss (g)	Cumulative weight loss (g)	Corrosion rate g/ cm2/yr	Potential (mV)	PH
1	15.35	15.35	0	0	0	-528	7.2
4	15.35	15.34	0.01	0.0062	0.37	-678	7.3
7	15.34	15.34	0	0.0094	0.28	-765	7.42
10	15.34	15.34	0	0.0119	0.29	-567	7.16
13	15.34	15.33	0.01	0.0177	0.14	-763	7.3
16	15.33	15.33	0	0.0206	0.15	-647	7.21
19	15.33	15.32	0.01	0.0284	0.05	-503	7.11
21	15.32	15.32	0	0.0308	0.06	-674	7.78
24	15.33	15.31	0	0.0345	0.05	-783	7.14
27	15.31	15.31	0.01	0.0418	0.07	-573	7.38
30	15.31	15.3	0.01	0.0494	0.05	-564	7.36
33	15.3	15.29	0.01	0.0559	0.06	-673	7.23
36	15.29	15.29	0.01	0.0637	0.04	-764	7.5
39	15.29	15.28	0.01	0.0688	0.03	-863	7.18
42	15.28	15.27	0.01	0.0752	0.07	-673	7.52
45	15.27	15.27	0.01	0.0835	0.06	-753	7.12
48	15.27	15.26	0.01	0.0914	0.05	-573	7.86
51	15.26	15.25	0.01	0.0979	0.04	-792	7.84
54	15.25	15.25	0.00	0.1014	0.04	-783	7.86

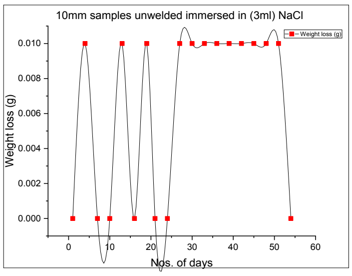

Figure 39. Weight loss g vs No of days

DOI: https://doi.org/10.30564/jmmr.v3i2.2400

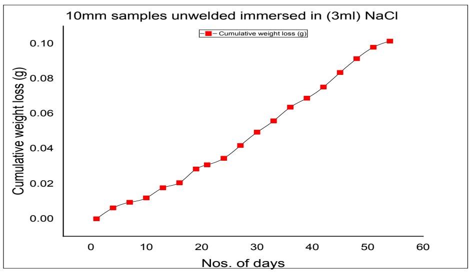

Figure 40. Cumulative weight loss g vs No of days

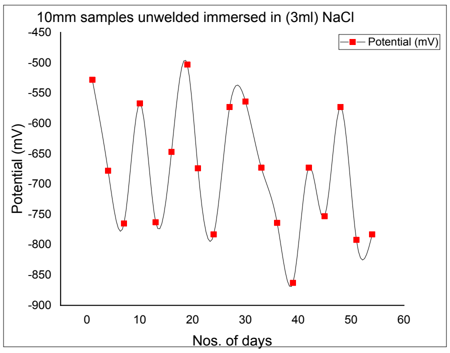

Figure 41. Corrosion rate g/cm^2/yr. vs No of days

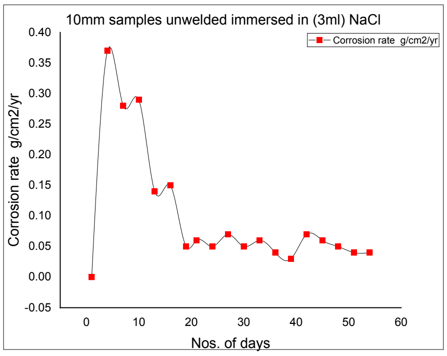

Figure 42. Potential (mV) vs No of days

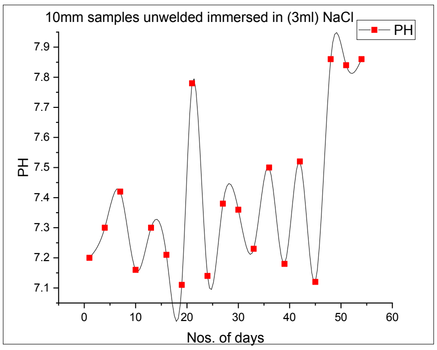

Figure 43. pH vs No of days

Table 4.8 B1: 10mm samples unwelded immersed in (4ml) NaCl

Nos. of days	Initial weights (g)	Final weights (g)	Weight loss (g)	Cumulative weight loss (g)	Corrosion rate g/cm2/ yr.	Po-tential (mV)	pH
1	14.61	14.61	0	0	0	-635	7.44
4	14.61	14.61	0	0.0004	0.48	-654	7.47
7	14.61	14.6	0.01	0.0068	0.27	-708	7.56
10	14.6	14.6	0	0.0113	0.13	-535	8.36
13	14.6	14.59	0.01	0.0174	0.14	-660	8.49
16	14.59	14.59	0.01	0.0225	0.09	-672	8.44
19	14.59	14.58	0	0.0269	0.07	-541	8.39
21	14.58	14.58	0.01	0.0033	0.08	-709	8.4
24	14.58	14.57	0.01	0.0386	0.07	-660	8.06
27	14.57	14.56	0.01	0.0458	0.08	-567	8.39
30	14.56	14.56	0.01	0.0517	0.06	-428	8.34
33	14.56	14.55	0.01	0.0571	0.05	-812	7.36
36	14.55	14.55	0	0.0613	0.03	-517	8.07
39	14.55	14.54	0.01	0.0664	0.04	-708	7.62
42	14.54	14.54	0	0.0702	0.03	-765	7.41
45	14.54	14.54	0.01	0.0776	0.05	-678	7.45
48	14.54	14.52	0.01	0.0822	0.04	-578	7.54
51	14.52	14.52	0.01	0.089	0.04	-688	8.3
54	14.52	14.51	0.01	0.0967	0.04	-656	7.61

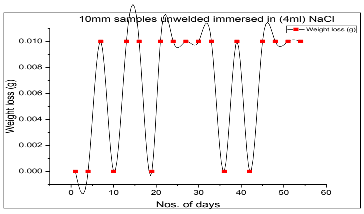

Figure 44. Weight loss g vs No of days

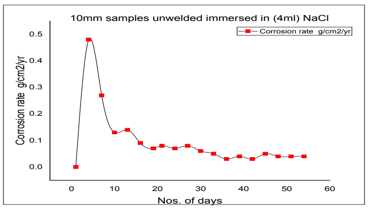

Figure 45. Cumulative weight loss g vs No of days

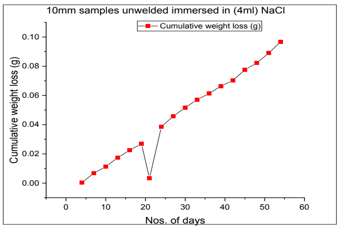

Figure 46. Corrosion rate g/cm^2/yr. vs No of days

DOI: https://doi.org/10.30564/jmmr.v3i2.2400

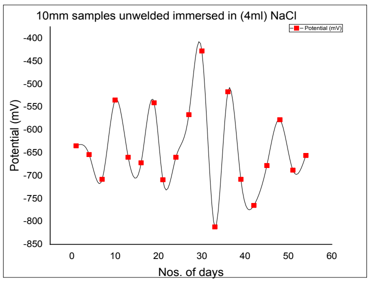

Figure 47. Potential (mV) vs No of days

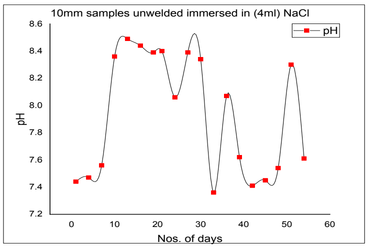

Figure 48. pH vs No of days

4.2 Electrochenical Test

(b) The corrosion test was conducted with the use of Electrochemical Tester Model: CHI604E. The tests were conducted in accordance with ASTM G199 - 09 (2014 Standard Guide for Electrochemical Measurement). An electrochemical cell containing the potential inhibitor solutions were used as the electrolyte, consisting of three electrodes, the working electrode (sample), counter electrode (graphite rod) and silver/silver chloride electrode was used as a reference electrode (Ag/AgCl). The tests were performed from -1.0V to +1.0V. The Open Circuit Tests were allowed to run for 3600 seconds while the Tafel tests were allowed to run for the same duration in seconds after which the graphs were plotted.

The samples used for the experiments were prepared in such a way that they were in the same sizes and dimensions of 1cm x 1cm. A total number of ten samples were prepared and five samples each for the samples A and B. Each of the sample have one control sample while the remaining four samples each were used to prepared samples 1-4ml solution of sodium chloride. Immediately the samples were mounted on the system. An Open Circuit Potential Time (OCPT) was carried out. The working and reference electrodes are connected in the Open Circuit Potential-Time technique (OCPT), and the potential difference across them was reported as a function of time. Since the counter electrode was not attached to the external cell, there was no current passing through the working electrode except for the bias current of the measuring amplifiers in the range of picoamperes. [11]. The values/data generated from the experiments were used to plot graphs. These graphs are shown in figures 49-58. Figures 49 -50 show the OCPT for welded and un-welded the medium carbon steel, while figures 51 -58 indicate the plot of Log(iA) against Current (A) for welded and un-welded medium carbon steel.

Interpretation of the Tafel plots for welded and un-welded samples for 1-4ml in sodium chloride.

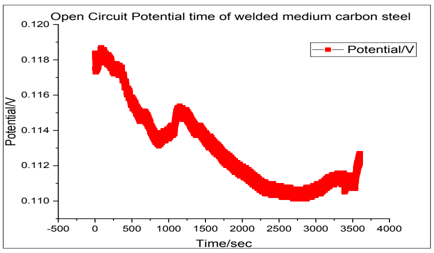

Figure 49. Potential vs time (OCPT) welded medium carbon Steel

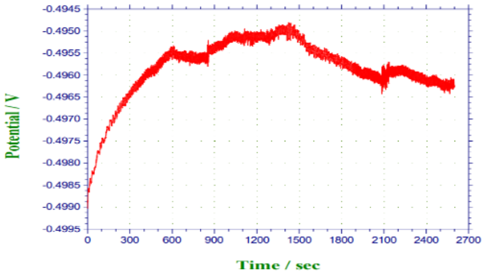

Figure 50. Potential vs time (OCPT) unwelded medium carbon Steel

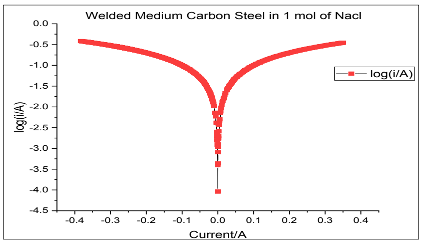

Figure 51. Log(i/A) for welded material in 1 ml NaCl solution

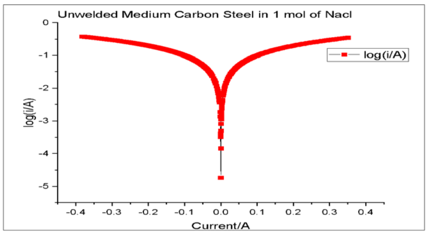

Figure 52. Log(i/A) for un-welded material in1 ml NaCl solution

DOI: https://doi.org/10.30564/jmmr.v3i2.2400

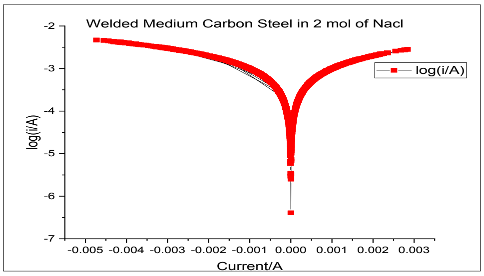

Figure 53. Log(i/A) for welded material in 2 ml NaCl solution

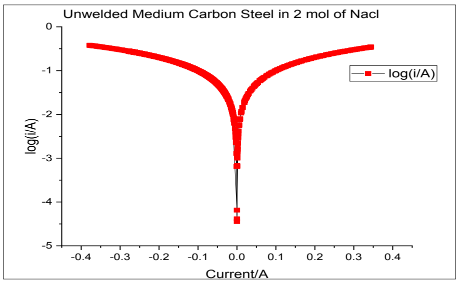

Figure 54. Log(i/A) for un-welded material in 2 ml NaCl solution

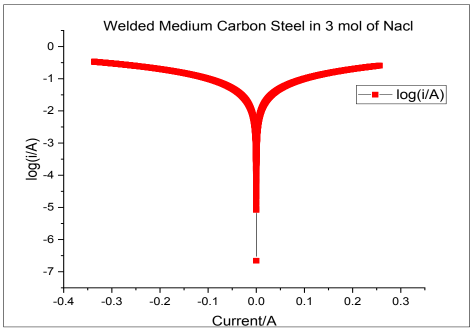

Figure 55. Log(i/A) for welded material in 3 ml NaCl solution

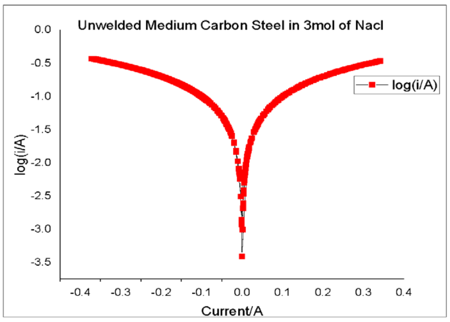

Figure 56. Log(i/A) for un-welded material in3 ml NaCl solution

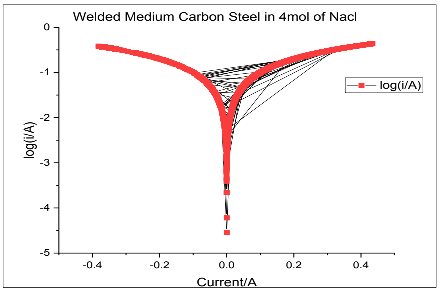

Figure 57. Log(i/A) for welded material in 4 ml NaCl solution

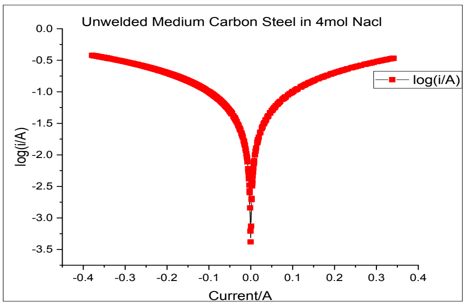

Figure 58. Log(i/A) for un-welded material in 4 ml NaCl solution

5. Conclusion

The Study on the Corrosion Behaviour of Welded and un-welded medium carbon steel in sodium chloride (NaCl) solutions were successfully performed. The experiments were in two parts, the first part took care of the weight loss measurement/analyses and the second part studied was based on the use of the electrochemical Analyzer/workstation. The materials used for the study was sourced from the Ajaokuta Steel Company Limited, Ajaokuta. Kogi State, Nigeria with references to the Light Section Mill. The obtained medium carbon steel materials were analyzed at the Quality Control and Materials Analyses unit of the Foundry Shop. These materials were identified and labelled as sample A and B. The experiments were performed under very strict environment as regards to corrosion science and engineering. 20ml of distilled water was used to prepare sodium chloride solutions. The obtained medium carbon steel materials were prepared for both experiments. The inverted Metallurgical Microscope was used to determine the microstructure of the samples, the samples were taken to South Africa for SEM and EDS analyses. The data generated were used to plot the graphs as shown in the various figures. It can be concluded that the welded medium carbon steel has better corrosion resisting tendency than the un-welded medium carbon steel.

References

[1] Revie, R.W., Uhlig, H.H. Corrosion and Corrosion Control. An Introduction to Corrosion Science and Engineering. 4th Edition, John Wiley & Sons, New Jersey, 2008

[2] Treseder, R. S. NACE Corrosion Engineer's Reference Book, 3rd edition. Houston: NACE. 2002

[3] Mattson, E. Basic Corrosion Technology for Scientists and Engineers. Second Edition, Bourne Press, Bournemouth, United Kingdom, 1996

[4] Ginzel E.A. Ginzel R.K. Study of acoustic velocity variations in line pipe steel. PBD, 1995, 53(5).

[5] Ginzel E.A., Ginzel R.K. Ultrasonic Properties of A New Low Attenuation Dry Couplant Elastomer. Materials Research Institute [20K Text / 15K in 3 Gif], 1995

[6] Callister, W.D. Jr. Materials Science and Engineering. 1997, 511-531.

[7] Smith, W.F., Hashemi, J. Foundations of Materials Science and Engineering. 4th Edition; Mcgraws - Hill Book. 2006: 28 - 36.

[8] Badmos, A. Y., Ajimotokan, H. A., Emmanuel E. O. Corrosion in Petroleum Pipelines. New York Science Journal, 2009, 2: 36-40.

[9] Leidheiser H, Granata R.D, R. Turoscy R. Technical Note: Alkali Metal Ions as Aggressive Agents to Polymeric Corrosion Protective Coatings. Corrosion. 1987, 43(5): 296-297.

[10] Osarolube, E., Owate, I. O., Oforka, N. C. Corrosion behaviour of mild and high carbon steels in various acidic media. Scientific Research and Essay, 2008, 3 (6): 224-228. Available online at: http://www.academicjournals.org/SRE ISSN 1992-2248 © 2008 Academic Journals (20) (PDF) Corrosion behaviour of mild and high carbon steels in various acidic media. Available from: https: //www.researchgate./publication/279711726_ Corrosion_behaviour_of_mild_and _ high _ carbon_ steels_in_various_acidic_media.

[11] Fontana M. G. Corrosion Engineering. McGraw-Hill, 1986 - Technology & Engineering 1986: 556.

[12] Electrochemical Analyzer /Workstation Model 600E Series User Manual 2014: 84.

[13] Tetretheway et at. Synergistic effect of cavitation erosion and corrosion of various engineering alloys in 3.5% NaCl solution Materials Science and Engineering. 2000, 290(1-2): 145-154.

[14] Narayanan Sankra T.S.N. Corrosion and Corrosion Preventive Methods. National Metallurgical Laboratory Madras Centre CSIR Complex Taramani, Chennai -600113.

[15] Mattson H. Richard. Introduction and Symposium Overview. First published: December 1996. ISBN: 9780471732792

DOI: https://doi.org/10.30564/jmmr.v3i2.2400

BILINGUAL PUBLISHING CO.
Pioneer of Global Academics Since 1984

Journal of Metallic Material Research
https://ojs.bilpublishing.com/index.php/jmmr

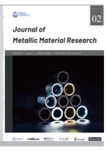

REVIEW

Original New Theory Abbreviation of Metals

Senchun Jiang[*]

Hangyu life saving Co., Ltd., Xiangyang, Hubei, 441002, China

ARTICLE INFO

Article history
Received: 9 September 2019
Accepted: 10 September 2019
Published Online: 31 October 2020

Keywords:
Gaussian curve
C-curve
Dispersion center
Supercooling dynamics
Carbon atom interaction

ABSTRACT

The electrons of metallic iron atoms all have wave-particle duality. The electrons of each iron atom are particles in the liquid state, the solid state is fluctuating. The wave-particle duality parameters of each iron atom electron are different, there is a small difference, the same is gathered into one, become a single grain.The parameters of wave-particle duality are different. The crystallization temperature of liquid state is different from that of solid state [1].

1. Properties of Metallic Iron Atoms

The spatial arrangement of iron atoms changes according to temperature, lt is a body-centered cubic lattice at high temperature. The middle temperature is a face-centered cubic lattice, lt is a body-centered cubic lattice at room temperature, The volume of ferrite cell is the largest at middle temperature, high temperature comes next, room temperature is the smallest. The high temperature BCC lattice structure is suitable for high temperature hot gas flow, medium-temperature face-centered cubic lattice structure fixed hot gas flow, good heat preservation performance, at room temperature, the BCC lattice structure is suitable for low temperature hot gas flow.

2. Atomic Arrangement

Regular arrangement of iron atoms does not allow other atoms to penetrate into the regular arrangement of the gap, other atoms can only penetrate into the defects in the arrangement of iron atoms, size and distribution of point, line and surface defects, determine the quality of the metal iron. The number of point, line and area defects is limited, a finite quantity determines the finite carbon content of iron. The size of grain boundary space is limited.

When there are few carbon atoms at the grain boundary, the iron atoms deprived of iron grains are combined into cementite at the grain boundary, over time carbon atoms aggregate at the grain boundaries to form graphite.

3. Iron Carbon Balance Diagram

The carbon atoms keep the iron crystal structure unchanged, that is to say, the stability of Iron structure is increased. The lines A, H, J and B of the iron-carbon equilibrium diagram are the lines of crystal-structure transition, G, P, S are also lattice structure transition lines, these

---

**Corresponding Author:*
Senchun Jiang,
Hangyu life saving Co., Ltd., Xiangyang, Hubei, 441002, China;
Email: 2126828166@qq.com

DOI: https://doi.org/10.30564/jmmr.v3i2.2374

two lines show that: the carbon atoms remain unchanged in the original structure. Carbon atoms are enriched into the crystal defect space to maintain the stability of the crystal structure.

The grain volume and defect space volume change with temperature, causing the separation and absorption of carbon atoms change of temperature transforms the structure. The precipitated carbon atoms are then enriched into the space with large defects in other grains, grain growth is a process of volume change and lattice defects constantly precipitating and absorbing carbon atoms, until the structural transformation.

C curve is the Gaussian curve in statistics,analyzing the C curve with statistical theory and everything will be clear. The undercooling power causes the transformation of the grain structure to a lower temperature, the martensite with transition structure from FCC structure to bcc structure was obtained by quenching, this is due to the combined action of carbon atoms and supercooling force, which reduces the temperature of structural transformation, the transformation process becomes longer, the result of slowing down. The reason for the high hardness of martensite is that there are three iron atoms in the cell structure. lt's the structure that causes the hardness. The volume of martensite unit cell is the largest, as result, the lattice defect space is large, the carbon-containing ability is much greater than that of the defects in the face-centered and body-centered lattices [2].

The primary and secondary temper embrittlement is the reason why the crystal structure is unstable before and after the transformation, which leads to increased brittleness. Tempering does not change the lattice from BCC structure to marten site structure.

Alloy steel, carbon steel, cast iron, whether in solid or liquid, there is an objective fact of lattice structure transformation at 1493℃ .

The principles of materials science are: structure determines performance.we should understand the metal iron from the structure. The face-centered cubic structure does not conduct magnetism, the magnetic conductivity of body-centered cubic junction is the reason for the size and size of the structural gap. lt is not the electrons of the iron atom that determine magnetic conductivity

References

[1] People's education press. Institute of curriculum and teaching materials. Edited by chemistry curriculum research center. Chemistry (compulsory 1). People's education press, 2004 preliminary examination and approval.

[2] Higher education press. Beijing Normal University. Central China Normal University. Nanjing Normal University. Inorganic chemistry. Volume 2. Fourth edition.

DOI: https://doi.org/10.30564/jmmr.v3i2.2374

BILINGUAL PUBLISHING CO.
Pioneer of Global Academics Since 1984

Journal of Metallic Material Research
https://ojs.bilpublishing.com/index.php/jmmr

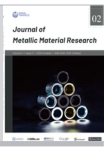

ARTICLE

Bulk Raw Materials Handling and Blending Techniques of Sinter Plant: A Case Study of Ajaokuta Steel Company Limited, Kogi State, Nigeria

Cyril Ocheri[1*] **Hebert. A. Obiorah**[1] **Romanus Egwuonwu Njoku**[1] **Nnaemeka Anthony Urama**[1] **Joseph Babalola Agboola**[2] **Christopher Nwankwo Mbah**[3] **Johnson Nwaemezie Ezeanyanwu**[3] **Chikezie Walter Onyia**[3]

1. Department. of Metallurgical and Materials Engineering, University of Nigeria, Nsukka
2. Department of Metallurgical and Materials Engineering, Federal University of Technology, Minna, Niger State
3. Department of Metallurgical and Materials Engineering, Enugu State University of Science and Technology, Enugu

ARTICLE INFO

Article history
Received: 21 September 2019
Accepted: 29 October 2019
Published Online: 30 November 2020

Keywords:
Blast furnace
Iron concentrate
Sinter Plant
Stockpile
Stockyard facilities

ABSTRACT

Bulk raw materials handling plant and sintering plant preparatory plants are established to receive, blend, stockpile, prepare and supply specified grades of raw materials for smooth operations of iron making plant (Blast furnace), steel making plant (Basic oxygen converter) and lime Plant(calcinations plant). The study discusses bulk raw materials handling and some general problem of scientific analysis and documentation of basic equipment details, stockyard facilities, bulk materials transport systems and sinter processes, for the general knowledge and operational procedures of these plant for effective and efficient operational processes for optical results. Iron ore concentrate supplied from the mines to some extent fluctuate in their chemical composition as a result of the nature of the deposit with various factors controlling beneficiation processes and addition of metal-bearing materials collected as a waste product from the Rolling Mills, Blast Furnace and Sinter Plant which must be recycled through Iron ore concentrate stockyard. The part of the sinter mixture is melted at a temperature about 1300-1480 ° C and a sequence of reactions shaping the sinter cake to be loaded into the blast furnace to produce iron from a pig.

1. Introduction

Bulk raw materials handling plant and sintering plant preparatory plants are established to receive, blend, stockpile, prepare and supply specified grades of raw materials for smooth operations of iron making plant (Blast furnace), steel making plant(Basic oxygen converter) and lime plant(calcinations plant). Moreover, the decision by the Federal Government to embark on this gigantic project in 1979 at the time the world oil market was facing uncertainties was informed not only by the to diversify the sources of foreign exchange but because of the catalytic effect of the steel industry in the development of the real sector of the economy. This

---

**Corresponding Author:*
Cyril Ocheri,
Department. of Metallurgical and Materials Engineering, University of Nigeria, Nsukka;
Email: cyril.ocheri@unn.edu.ng

DOI: https://doi.org/10.30564/jmmr.v3i2.2409

includes amongst others, the utilization of local raw materials (which a bound in large quantities in the country yet untapped) to a high degree in the production process, encourage and setting up of steel-related down-stream and auxiliary industries, inculcation of adaptive technology culture in Nigeria and provision of strong research and development base for the technological take-off of the country. In fact, Ajaokuta steel company is the first company of this magnitude in Nigeria to have a high input level of Nigerians in the project conception and management.

The Ajaokuta steel company is planned to produce 1.3millon tonnes of liquid steel per annum in the first phase to be finished in too long products as; 130,000 tons of wire rods, 400,000 tons of long products and light structures, 560,000 tons of rails and medium structures. This is to be upgraded to 2.6million metric tonnes in the second phase. The steel plant is designed to reach an ultimate capacity of 5.6million metric tonnes per year for long and flat sheet products including various sizes of heavy, medium and light structural sections, rails, plates, pipes and thin sheets. The integrated plant is one of the comprehensive steel plants in the world. It is unique in the completeness and spread of its integration. It comprises several full-fledged auxiliary, support and service industries all in one location. Some of these are; (1)A captive thermal power plant of 110 MW capacity, (2)A 7,000 tons capacity integrated foundry, (3) A massive Alumino-silicate plant, the largest in sub-Sahara (Africa), (4) A coke-oven and by-product chemical plant, (5)An oxygen separation plant, (6)A lime calcinations plant, (7)A rubberizing plant, (8)Four independent Rolling Mills, (9)A 795,000 tons capacity Billet mill - the only one in Nigeria and (10)An integrated mechanical repair shop complex.

In Ajaokuta, the technology adopted is the time tested conventional Blast furnace and Basic oxygen furnace (for Iron and steel making processes), suiTable for making high tonnage steel. The development strategy for the steel plant was based on a “backwards integration” approach.

This entailed the construction and completion of the final process stages first followed by the construction of the primary production plant. The backwards integration approach adopted was to allow the units already completed and which can stand alone as viable enterprises to generate revenue for the completion of the primary plants. The analysis of sourcing, handling, blending and preparation 0f the basic raw materials to be administered to these primary operations of Iron and steel making processes are the main aims and objective of this project.

The systematic addition and blending of these materials to achieve a homogenous stockpile of Iron ore concentrate with a variety of chemical compositions throughout the stockpile not exceeding 0.5% is yet another major reason why this research work was studied. Other problems often encountered by engineers in the field in maintaining relatively sTable sinter basicity (Lime / Silica ratio), this was also the reason for discussing the basic steps involved in Sinter charge calculations.

2. Raw Materials Requirements of Iron and Steelmaking

The raw materials requirement of Iron and steel making processes for Ajaokuta Steel Company Limited (ASCL) comprises of the following: (1) Iron ore concentrate, (2) Coking coal, (3) High-grade Iron ore lumps, (4) Fluxes(Limestone and Dolomite), (5) Bauxite, (6) Manganese ore and (7) Ferrous scrap. The annual consumption of the various raw materials and their possible sources are shown in Table 1 below:

Table 1. Raw material input of ASCL

S/No	TYPE OF RAW MATERIALS	SOURCES	ANNUAL REQUIREMENT (TONNES)
1.	Iron ore concentrate	Itakpe (Kogi State)	2,171,000
2.	High-grade Iron ore lumps	Imported	55,000
3.	Coking coal	Imported	1,300,000
4.	Limestone	Jakarta / Mfamosing	694,000
5.	Dolomite	Osara / Burum	265,000
6.	Manganese ore	Imported	84,000
7.	Bauxite	Imported	13,000
8.	Ferrous metal scrap	Local	120,000

2.1 Sourcing of Limestone

For the purpose of this project, only sourcing of limestone being the major fluxing agent in Iron and steel making process will be discussed in detail. Investigations on the suitability of Mfamosing limestone deposit for converter grade limestone was initiated in early October 1977 [1]. This was done because the available limestone deposit at Jakura, though chemically suiTable for converter lime, is mechanically unfit for conventional L.D converter steelmaking process. Furthermore, it was envisaged that a total of about 680,000 tonnes of limestone per annum would be required for the various processes in the steel complex out of which 240,000 tons per annum of the high-quality limestone would be needed for the steelmaking operations [1].

2.1.1 Geology of the Mfamosing Deposit

The Mfamosing deposit is located 30km northeast of Calabar city in the Cross-River State of Nigeria. The distance between this location and Ajaokuta is approximately 600km by road. The deposit is sedimentary in origin, occurring in marginal basin deposits of Cretaceous age (About 100 mil. Years old) overlying the Precambrian basement and consist in well-developed algae, or lithic and detritus facies which related to a reef and classic environment deposits [2]. The reef variety is white in colour while the classic variety is grey. Only the white variety of the deposit satisfies the requirement for converter lime manufacture. For a cross-section of the deposit see Figure 1 below:

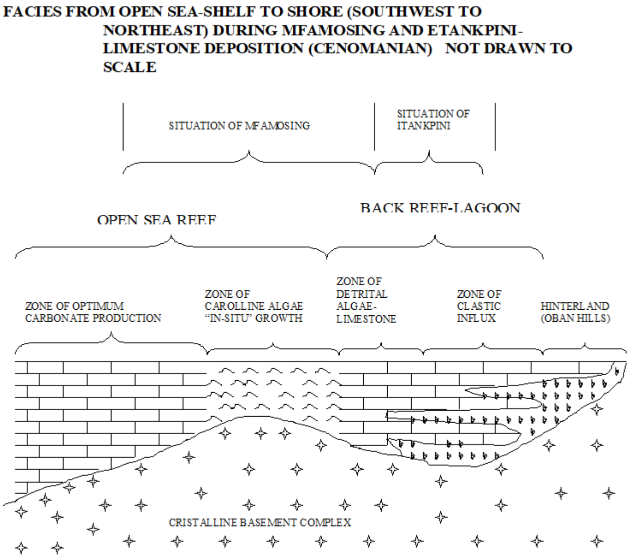

Figure 1. Idealised Stratigraphic Model Showing Variation In the exploitation of the Deposit

2.1.2 Exploitation of the Deposit

The total overburden to be stripped for quarrying operations is estimated to be 6.72 million tonnes and the estimated exploiTable reserve is 18 million tonnes. They are known on the surface of 0.7 km^2 and mined on 0.25km^2. Based on the geological information of the deposit, it is evident that selective mining will be absolutely necessary since not all the deposit is suiTable for the high-quality limestone required for the steel production.

2.1.3 Chemical and Physical Analysis of Mfamosing Limestone

Generally, lime is the basic slag forming component of the total charge in L.D. converters for steel making. For this purpose, very stringent high-quality lime is a basic pre-requisite for the converter lime. Table 2 below compares the properties of Mfamosing lime with Jakura and the standard established in the Detailed Project Report [1]. It clearly indicates that the Mfamosing is very suiTable for the converter lime. It has also been recorded that the limestone yields over 70% of fines below 10mm and just 10% of the accepTable lumps after calcinations.

Table 2. Chemical Analysis of Limestone from Jakura and Mfamosing [1]

S/No	Element	DPR (%)		Jakarta (%)		Mfamosing (%)	
	(%)	Sinter & B/ Furnace	Converter	Grey	White	Grey	White
1	Cao	53 min.	53.5 min.	52.28	54.7	54.5	55.04
2	MgO	0.64 max.	1.2 max.	1.14	0.41	0.58	0.24
3	SiO_2	1.81 max.	1.0 max.	2.6	0.23	5.07	0.69
4	S	0.052 max	0.05 max.	0.14	0.05	0.18	0.04
5	P	0.01 max.	0.06 max.	0.12	0.03	0.04	0.01
6	Al_2O_3	0.31 max.	1.5 max.	1.75	0.61	1.6	0.37
7	L.O.I.	43.76	43.76	40.2	43.76	40.2	43.74
8	Fe_2O_3	0.21 max.	1.5 max.	1.3	0.19	1.2	0.2
9	P_2O_2	0.21 max.	0.03 max.	0.07	0.05	0.02	0.02
10	SO_3	0.13 max.	0.13 max.	0.23	0.21	0.09	0.11
11	TiO_2	0.02 max	0.02 max	0.05	0.04	0.01	0.02
12	ALKALI	0.09 max.	0.09 max.	0.15	0.14	0.06	0.08

In terms of CaO and SiO_2 values, the above Table II indicates that whilst all the three limestones are suiTable for sinter making and Blast furnace additions, only the white varieties of Jakura and Mfamosing are suiTable for steel making.

2.2 Sourcing Dolomite

The major sources of dolomite to the integrated steel plant for control of Sinter basicity and production of dolomite refractory bricks are the Osara and Burum deposits. However, the Osara deposit is accorded top priority after a semi- Industrial test on the deposit was carried out at the all-union refractory Institute, Leningrad (USSR). The chemical and physical analysis conformed to the standard specification in the Detailed Project Report [1] as indicated in Table 3 below:

Table 3. Chemical Analysis of Osara Dolomite Deposit

S/No	Element	DPR (%)	Osara Deposit (%)
1.	L.O.I.	35.00	33.11
2.	SiO_2	6.38	13.10
3.	Al_2O_3	0.30	0.27
4.	Fe_2O_3	3.00 max.	2.52
5.	CaO	30.00 min.	35.89
6.	MgO	15.00 min.	14.82
7.	K_2O	0.02 min.	trace
8.	NaO	0.20 max.	0.16
9.	MnO	0.10 max.	0.06
Total		100 %	99.93 %

DOI: https://doi.org/10.30564/jmmr.v3i2.2409

3. Sourcing of Bulk Materials for the production of Sinter

3.1 Sourcing of Iron Ore Concentrates

The source of this raw material is the National Iron Ore Mining Company (NIOMCO) at Itakpe in Kogi State. The chemical analysis of this important raw material required by the DPR is as shown in Table 4 below:

Table 4. Chemical Analysis of Iron Ore Concentrate for NIOMP & DPR [3]

S/No.	Element	DPR %	NIOCOM(Itakpe) %
1.	Fe	63.00	65.60
2.	Al_2O_3	0.80	1.02
3.	SiO_2	0.80	5.14
4.	P_2O_5	0.07	-----
5.	P	0.03	0.055
6.	S	0.014	0.015
7.	Mn	0.08	0.06
8.	CaO	0.40	0.30
9.	MgO	0.20	0.18
10.	TiO_2	0.17	0.12
11.	$Na_2O + K_2O$	0.15	0.17
12.	Zn(ppm)	---	traces

3.2 Sourcing of Coking Coal

Good quality metallurgical coal is not available in Nigeria in economic quantity, therefore, the total quantity of metallurgical coal is to be imported. In order to minimize the import, coal carbonization tests have been conducted to determine the suiTable coal blends and the extent indigenous coal that can be used to blend the imported coals. EBE of Germany after conducting the necessary tests have concluded that Indigenous Enugu coal is to be crushed to 100 per cent below 0.1mm. Other blends have also been recommended to consist of 100 per cent of imported coals. The test report has been accepted by V/O Tiajpromexport (TPE) and it was decided to use 100 per cent imported coal blend during the commissioning of the plant and up to guarantee test period. To improve the economics of ASCL, it will be prudent to maximize the use of indigenous coal in the blend by adopting suiTable technologies such as partial briquetting of coal etc.

The ranges of variations of chemical analysis in metallurgical cokes are given in Table 5 below:

Table 5: Proximate Analysis of Metallurgical Cokes

S/No.	Elements	Range
1.	Fixed carbon	83-90 %
2.	Volatile matter	0.5-4 % (preferable < 2 %).
3.	Ash.	4-15 % (preferable < 10 %).
4.	Moisture.	< 5 % (preferable < 3 %)
5.	Sulfur.	0.5-3 % (preferable < 1 %).
6.	Phosphorous	< 0.04 %

4. Raw Materials Off-Loading Facilities

The whole plant layout covering materials handling and sintering plant which this project is project is based upon is shown in Figure 2 below:

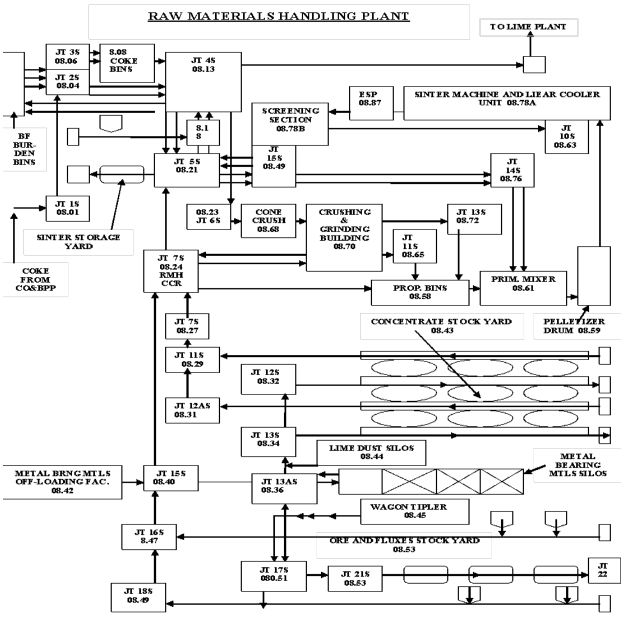

Figure 2. Layout of Sintering Plant

This unit was charged with the responsibility of receiving, blending, stockpiling and dispatching to the Sintering plant, Blast furnace, Lime plant and Steelmaking shop according to laid down procedure. To perform this responsibility efficiently and effectively, the unit comprises the following sections: (1) Off-loading facilities, (2) Fluxes stockyard. (3) Metal bearing materials stock bins. (4) Iron ore concentrate stockyard. (5) Aspiration plants (Dust cleaning plants) and (6) Network of inter-departmental conveyor belts.

4.1 Fluxes Off-Loading Facilities

Fluxes are delivered to the steel plant by two conventional methods of haulage viz; Railway and Road, therefore an elaborate arrangement has been put in place to receive the fluxes by both bottom discharge locomotive wagons and tipping trailers. In each case, the fluxes are discharged into underground bunkers 6Nos. in each arrangement with a combined volume $68m^3$. In any of the arrangement, the fluxes are off-loaded and fed into a common 1400mm width conveyor belt by means of Belt feeders for onward delivery to fluxes stockyard. The load-carrying capacity of the conveyor belt is 1500 tons per hour.

4.2 Coking Coal Off-Loading Facilities

Because of the high tonnage requirement of coking coal

DOI: https://doi.org/10.30564/jmmr.v3i2.2409

for production of coke in the coke-oven plant, it was envisaged that only rail transport system could cope with the annual requirement of 1,386,000 tonnes of coal per annum. As a result, the off-loading facility for coal was designed to receive the coking coal by means of only bottom discharge wagons into 6 numbers underground bunkers of the combined volume of 68m^3. By means of belt feeders, the discharged coals are fed into 1000 tonnes/hour conveyor belt, which is expected to deliver at the spacious coal stockyard via a rail-mounted stacker machine and later dispatch to coke-oven proportioning bins by means of a reclaimer machine on request by the user shop. A schematic diagram of the rail-mounted traversing stacker machine is shown in Figure 6 below. The area of one stockyard is 460m x 26m with an average bulk height (Stocking height) of 2.5m and a volume of 29,900m^3. The storage capacity of one stockyard is 30,000 tonnes of coking coal, there are four stockyards of similar dimension, which give a total storage capacity of 120,000 tonnes. This corresponds to 3 weeks of continuous operation stock to coke-oven. The stockyard is also equipped with 3numbers of Stackers with the capacity of 1,500 tonnes per hour each and 3numbers of Reclaimer with the capacity of 1,300 tonnes per hour each. The off-loading facility building has a height of +18.035m and - 19.3m deep (i.e. from level ground surface), this building housed all the receiving underground bunkers and conveyor belt delivery tunnels.

4.3 Metal Bearing Materials Off-Loading Facilities

Metal bearing materials are waste products of rolling mills, Blast furnace, Lime calcinations plant and Sintering plant processes which otherwise would have passed for waste but with this blending techniques developed they can now be recycled back into the process line. The arrangement provided in raw materials handling unit to receive, off-load and stockpile metal-bearing materials either by tipping trucks or by pneumatic tankers as the case may be. The type of metal-bearing waste and their estimated quantities are listed below:

(1) Scales from the Rolling Mills = 37,000 t/yr.
(2) Lime screening from the Lime Plant = 10,000 t/yr.
(3) Flue dust from the Blast furnace) = 18,000 t/yr.
(4) Sinter screenings from sintering plant = 170,000 t/yr.

Items (1), (2) and (4) above are received by tipping trucks while item (3) is received by pneumatically powered off-loading tanker trucks.

4.4 Iron Ore Concentrate Off-Loading Facility

The concentrate was received from National Iron Ore Mining Company (NIOMCO) by rail wagons of 60 to 70 tons carrying capacity into ASCL's marshalling yard where NIOMCO's locomotive engine de-coupled and coupled with trains of pre-arranged empty wagons back to NIOMCO's loading yard for another circle. The circle time was determined to be 3hrs 22mins. ASCL's shunting locomotive engine was coupled to the concentrate consignment from marshalling yard and move the loaded wagons through the intricate network of rail lines until it is carefully positioned on the wagon tippler's discharging track. The shunting locomotive engine was de-coupled and re-coupled to the previously discharged empty wagons back to marshalling yard for onward transfer back to NIOMCO. This is the main function of ASCL's internal shunting locomotive engines. The positioned, loaded wagons on wagon tippler's track are coupled with an electrically remotely controlled wagon-pusher (or car pusher) see Appendix V via a pushing flat form attached with the pusher. The car pusher has a tested pushing capacity of 160 KN, with this pushing force it can push 25 wagons loaded with 60-70 tonnes of concentrate, with a forward speed of 0.5m/sec and 1.0m/sec while empty.

The car pusher itself has a total weight of 70 tonnes. Its function is only to push fully loaded wagons serially and carefully position one wagon at a time on the centre of wagon tippler's plat-form (cradle). This was done by the operator from his operating cabin (pulpit) with the help of wagons attendant on the shop floor, and perform the function of supervising the centring operations, coupling and decoupling of wagons before and after each tipping circle. Massive rotating structure measuring 17470mm x 9639mm x 9038mm equipped with a well-balanced platform that accommodates loaded wagons ready for off-loading. The plat-form (cradle) was overlain with a railway track properly aligned with the surface railway track when in normal idle position but it rotates with the tippler when off-loading independently from the surface railway track. During tippling operation, the rotor rotates through an angle of 175^o. At this tilt angle, the materials are off-loaded into an underground bunker by means of gravity and a vibrator to ensure all content of the wagons are completely emptied, after which the tippler return back to its normal position by reversing the tippling action ready for another circle of operation.

This rotation is accomplished by employing the principle electro-dynamic braking system where alternating current and direct currents are charged to the system alternately at various pre-determined angular stages of the 175^o rotation. At the dead-end of 175^o, the whole power supply is cut-off, this action instantly set the electro-hydraulic braking system on. It was timed to remain in this

DOI: https://doi.org/10.30564/jmmr.v3i2.2409

position for a period of about 15 seconds during which vibrator must have stopped and all content of wagon emptied. The whole process of the rotation was then reversed to its initial take-off position and circle take s 63seconds to complete.

The underground bunker has a capacity of 180 tonnes of concentrate, it is equipped with apron-feeder below the bunker, which feeds concentrate continuously into the network of conveyor belts of 1000 tonnes capacity through chutes at each transfer points from underground to surface concentrate stockyard. The Wagon tippler building has a height of +18.035m and -19.30m from the ground surface.

5. Theoretical Analysis

5.1 Stockyards Ore and Fluxes Stockyard

Raw materials received by ore and fluxes off-loading facilities are discharged into ore and fluxes stockyard by means distributing car positioned on a gallery elevated at 22m above the stockyard ground level and it is mounted on a rail with electric drives that enable it traverses the whole length of the stockyard which is 566.2m. The distributing car ensures stockpiling of ore and fluxes at pre-determined spaces earmarked for each type of ore and fluxes. The overall area of the stockyard is 566.2m x 94m = 53222.8m^2, with this surface area, the stockyard can store up to 30 days stock of the following materials:

(1) Limestone =58,400 tonnes

(2) Dolomite = 24,460 tonnes and 90 days (3 months) stock of

(3) Bauxite = 3,250 tonnes

(4) High grade Iron ore lumps = 14,000 tonnes.

The stockyard is equipped with two giant pay-loaders of KOMATSU make; each has a 5m^3-bucket capacity charged with the responsibility of dispatching ore and fluxes to the user shops as directed by dispatcher stationed at the central control room. The stockyard is also equipped with 1,300 t/hr conveyor belt at both sides used for dispatching the fluxes to the user shops. A cross-section of various stockpiles of ore and fluxes and the dimensions of the area they occupy is shown in.

5.2 Iron Ore Concentrate Stockyard

Iron ore concentrate received by wagon tippler is stored in this stockyard by means of a Stacker machine shown in figure 6. The whole stockyard consists of 3 bays and in each bay, there are 4 stockpiles, each stockpile has the following dimensions:

Figure 6. Stacker and Reclaimer Machines with Stock Pile of Iron Ore Concentrate

Length = 92,000mm

Width = 30,000mm

Height = 13,500mm

Volume = 37,260m^3

Period of stock = 30 days.

Tonnage of stockpile = 93,150 tones.

The number of stockpiles in a bay = 4 stockpiles.

Total No. of stockpiles 3 x 4 = 12 piles.

Total tonnage capacity of the whole stockyard = 1,117,800 tons.

Effective volume of stockyard = 447,120m3.

Specific bulk weight (density) of Conc. = 2.5 t/m^3

Details of the stockyard arrangement are shown in the general layout diagram of Appendix IV above.

5.3 Stockpile Building - Process Techniques

There are three widely known methods of building stockpiles of Iron ore concentrate viz; Chevron layering, Wind brow layering (parallel pile), and Coil layering [4]. The decision to apply any of the three methods entirely depends on the chemical and physical characteristics of the raw material being stockpiled. During this project work, the chemical and physical properties of the beneficiated Iron ore concentrate from Itakpe was carefully studied and analyzed, chevron system of stockpiling is hereby recommended for use in ASCL's concentrate stockyard, this is because the concentrate received from the beneficiating plant of NIOMCO has a particle size range from 0 to 1mm and it has a relatively uniform chemical composition. Chevron method is suiTable for this class of material since there are no large lumps to give rise to size segregation at base of stockpile because of gravity differential during stockpiling operation. For this reason, the chevron method of stacking will be discussed in detail with a view

DOI: https://doi.org/10.30564/jmmr.v3i2.2409

to implementation when full operation commences. Other methods too will be discussed briefly.

Figure 7. Stacker Machine

5.3.1 Chevron Layering

This method consists of traversing the stacker arranged to feed the centre of the bed being formed. On the first pass, a triangular section of the material was deposited along the length of the stockyard. Let us consider the stacker having a stocking-out capacity of 1,500 t/hr and an average traversing speed of 25 meters per minute. The angle of repose of Iron ore concentrate is 35o. On the first pass, a triangular section pile was deposited along the length of the stockyard having a width of 1125mm and a vertical height of 375mm. On the second pass, a thickness of 150mm was added to the top of the first pass (pile). As bedding proceeds, the thickness of the layers is theoretically decreasing to only a few mm. The main disadvantage of this method is that segregation of materials occurs where lumpy materials constitute parts of the feed, resulting in the larger materials tending to be deposited in bands at the bottom and outside edges of the pile. In some instances, depending on the method of blending and reclaiming employed, this does not give the correct beneficiation required to the final burden. In the case of ASCL, at least for the nearest future, it is an only fine concentrate (0-1mm) was expected to be bedded. Chevron layering is, therefore, most suitable, providing a finished pile that is practically homogeneous in its size distribution and chemical composition.

5.3.2 Wind Brow (Parallel Pile) Layering

This method consists of laying a series of parallel piles by slewing the stacker at the end of each long travel circuit down the stockyard. When the first pile has been laid over the full base area of the bedding yard, the second tier of the piles is formed by filling in the furrows left between the piles. In this manner, a flat-topped pile can be formed if so desired depending on the base, width and height of the pile.

Figure 8. Reclaimer Machine with Iron Ore Concentrate Stockpile

The advantage of this system is that it avoids segregation, the disposition of the lumpy materials of each pass being restricted to the confines of its own smaller triangular pile as an integral part of the whole bed. An examination of a pile bedded in this manner clearly indicates a pre-determined cross-section blend with the lumpy materials deposited consistently throughout the completely homogeneous mass.

5.3.3 Coil Layering

This is a system similar to that described above, but with added refinement on the stacker control equipment. This would entail a form of Pantograph system or similar method so that the control gear would be coupled to a profile model of the refined file being laid. Bedding would begin at the side of the stockpile remote from the stacker, and the machine would traverse.

The full length of the stockpile. At the end of the yard, the stacker would be arranged to slew round to form the end of the pile before returning along the yard on the edge of the pile nearest the stacker. At the opposite end of the yard, the stacker would automatically slew to form the other end of the pile and on the second complete circuit. A coil layer would be formed within the periphery of the first. Layering would continue until the whole of the bedding area was covered with triangular piles, each representing one pass of the Stacker. Now, the Stacker would be elevated to form the second tier by filling the furrows left between the initial base piles. This process would con-

DOI: https://doi.org/10.30564/jmmr.v3i2.2409

tinue with the coils becoming progressively smaller until the desired height of stockpile had been formed. The additional advantage of this system over parallel pile layering is that it spreads the materials more evenly throughout the width and length of the bed. Although such an automatic system has not been installed to date, as far as we know, due to the high initial capital cost of control gears and the general lack of development in this direction, this method could well be the answer to the age-old enemy of bedding segregation.

5.3.4 Determination of Stacker Traverse Speeds

It will be readily appreciated that in order to attain efficient bedding it is necessary to achieve a constant rate of stocking of materials irrespective of the direction of travel of the equipment along the stockyard. Obviously, if the stacker travels at the same speed in the forward and reverses direction, due to the decreasing length of the material-carrying section of the main stocking-out belt.

Figure 9. Stacker and Reclaimer Machines with Stock Pile of Iron Ore Concentrate

Thus in order to attain a constant rate of stocking-out, we have two separate conditions. During forward motion of the Stacker, the amount of materials laid equals the relative velocity of the materials discharged multiplied by the weight of material per meter of the belt. During the reverse motion of the Stacker, the amount of material laid equals the relative velocity of the material discharge multiplied by the time to traverse the length of stock-yard in the reverse direction, multiplied by the weight of material per meter of the belt.

Let W = Rate of materials flow tons/min.

V = Velocity of stockyard belt, m/min.

V_f = Traversing velocity of Stacker in the forward direction, m/min.

V_r = Traversing velocity in the reverse direction, m/min.

L = Distance traversed by Stacker in each direction.

Therefore, the following can be deduced:

(1) During forwarding direction, the relative velocity of material discharge = $V\text{-}Vf$

(2) During the reverse direction, the relative velocity of material discharge =$V\text{-}Vr$

(3) Time to traverse the length of stockyard in forwarding direction = L/Vf

(4) Time to traverse the length of stockyard in reverse direction = L/Vr

Then,

The amount of material laid in forward direction =

$$\left(V-Vf\right).\frac{L}{Vf}.W/V$$

The amount of material laid in reverse direction =

$$\left(V+Vf\right).\frac{L}{Vf}.W/V$$

These rates are to be equal,

$$\left(V-Vf\right).\frac{L}{Vf}.\frac{W}{V}=\left(V+Vr\right).\frac{L}{Vr}.W/V$$

L, W and V are equal in both sides, then the equation reduces to

$$\frac{\left(V-Vf\right)}{Vf}=\frac{\left(V+Vr\right)}{Vr}$$

$$\left(\frac{V}{Vf}\right)-1=\left(\frac{V}{Vr}\right)+1----equation1$$

$$V/Vf-2=(V/Vr)$$

$$V/Vr=\left(V-2Vf\right)/Vf$$

$$\left(\frac{V}{Vr}\right)=\left(\frac{V-2Vf}{Vf}\right)$$

$$Vr\left(V-2Vf\right)=V.Vf$$

$$Vr=V.\frac{Vf}{V-2Vf}=Reverse\,Velocity----equation\ (ii)$$

From equation (i) above

DOI: https://doi.org/10.30564/jmmr.v3i2.2409

$$\frac{V}{Vf} = \left(\frac{V}{Vr}\right) + 2$$

$$\left(\frac{V}{Vf}\right) - 1 = \left(\frac{V + 2Vr}{Vr}\right)$$

$$Vf\left(V + 2Vr\right) = V.Vr$$

$$Vf = \left(\frac{V.Vr}{V + 2Vr}\right) = Forward\,Velocity - - - - equation\,iii$$

Although the traversing velocities of Stacker are not directly proportional to the speed of the main stocking out belt, V_f must be less than V, Otherwise, no material can be deposited over the Stacker's head in the forward direction. Examination of equation (ii) will show that V_f approaches $\frac{v}{2}$, V_r approaches infinity, and in practice, V_f is always considerably less than $\frac{v}{2}$ as previously pointed out, V_r will always be faster than V_f and generally practical considerations will fix the value of V_r at a maximum, thus allowing V_f to be determined from equation (iii).

6. Determination of Stacker Capacities

Since the time taken to travel along the stockyard in the forward direction is greater than that taken to travel in the reverse direction, and since the amount of material deposited in both direction must be the same, then obviously the rate of material flow over the boom conveyor under these conditions must be different. The following expressions will give the actual rates during forward and reverse traversing of the boom stacker. The rate of flow over the boom conveyor in the forward direction equals the rate of flow along the stockyard belt minus the weight of materials per meter of stockyard belt, multiplied by the traversing velocity of the Stacker. We have, therefore:

Rate of flow of material over boom conveyor in the forward direction

$$W - (W.Vf / V)$$

This expression can be re-written as

$$[(V - \frac{Vf}{V}]$$

$$((V - \frac{Vf}{V})].W\ tonnes\ /min$$

Rate of material flow over the boom conveyor in the reverse direction equals the rate of material flow along the stockyard belt plus weight of material per foot of stockyard belt multiplied by the traversing velocity of the stacker. We have therefore the rate of material flow over boom conveyor in the reverse direction: W+(W+Vr/V) . This expression can be re-written as $[(V + \frac{Vr}{V}]W\ tonnes\ /min$.

Number of passes: - The number of passes in producing a pile influences the efficiency of blending a great deal. It is given by $N = (W.V.60)/(C.L)$

Where N = Number of layers or passes.

W = Pile capacity, tons.

V = Average Stacker traversing velocity, m/min.

C = Main stocking belt capacity in tons/hour.

L = Length of the stockyard.

7. Sintering Plant

The purpose of sintering process is to prepare high-quality feedstock for the Blast furnace from Itakpe Iron ore concentrate, manganese ore, Blast furnace flue dust, mill scale and other Iron bearing materials by sintering them with the corresponding amount of limestone and dolomite with coke breeze used as solid fuel. The heart of a sintering plant work is the production of sinter cake. In accordance with the requirement of a Blast furnace process, good sinter should have: (1) Constant content of Iron manganese and Iron monoxide with minimum deviation from basic ones; (2) Constant (with minimum deviation from basic ones), basicity that is calcium dioxide-to-silicon dioxide ratio; (3) Minimum sulfur content; (4) High mechanical strength; (5) Minimum content of fines (fraction 0-5mm) when being charged into the blast furnace.

Getting uniformity with respect to maximum temperature. The distribution of heat ensures homogeneous sintering, refining, Efficiency and synthetic efficiency. Sintering of a double layer is Performed in some plants to achieve this goal (realization of Homogenous Tmax in its entire sinter bed thickness), and it consists of the preparation of the upper coke layer Contenu in the bottom to stop the ten [23]. When sintering is achieved at lower temperatures than 1300 ° C, decreases magnetite formation (less FeO) and improves the RI and the Degradability Index (RDI)-RDI. In addition, the optimal structure for reducibility of sinters Attainment of hematite nuclei (un-melted) in the blast furnace Surrounded by a network of acicular ferrites [33].

In modern plants, infrared thermography is used to Track the burn-through sintering point (when the flame occurs) The front approaches the base of the bed, but also for predicting Sinter characteristics and solid fuel rate change (adjusting the solid fuel rate) Amount of coke in a blend) [32]. Simulation models for sintering have been used to research the Method variables [30,31], so that the equations for heat distribution could be achieved [18]. The conduct of crude blends with a high content of goethite ore in the structure and permeability of sinter beds were examined. Japanese steel mills since the 1980s [24,26]. Sintering is a method of thermal agglomeration (1300-1480°C, [29] of a blend of mineral fines from iron ore (0.5 to 8 mm), iron and steel production by-products, Fluxes, elements forming slag, and fossil (coke) fuel. The target method by which the mixture of charged materials is mixed partly fused to create clustered clusters at a high temperature, the load (12-35 mm) for the blast furnace is received. The required physical-chemical and lowest mechanical characteristics [26]. On the opposite, incineration occurs as a horizontal layer. This passes across the bed vertically. The density of this A small fraction of the bed is a layer. Permeability is an output Load requirement, and for that reason the granulation Method is used beforehand (permeability enhanced during [22]. The sintering process is dependent on an increase in the temperature of Rough mix with a view to partial melting and Creation of a molten metal that crystallizes during refrigeration. In many mineral phases that agglomerate or solidify The system. The coke burning provides the energy for [27,28]. Sinter is stronger at softening and melting than pellets and ore, but worse at meltdown and high-temperature gas resistance, resulting in a 65 per cent mixed burden Sinter, 20 per cent lump ores, and 15 per cent pellet Best Outcome [34].

8. Raw Materials Requirement for Sinter Production

The raw material consumption data for the production of high-quality sinter are shown in Table V below; Sinter burden consists essentially of Iron ore concentrate, metal-containing waste, manganese sinter ore, lime screening, limestone, dolomite, sintering recycles and solid fuel fine (coke breeze).

Table 6. Raw Material Requirement for Sinter Production

S/No.	Type Of Raw Material	Consumption (tons/year)	Size Range(mm)	Moisture Content (%)
1.	Iron ore concentrate	2,135,000	0-1	6
2.	Mill scale	40,000	0-1	6
3.	Blast furnace flue dust	18,000	0-1	8
4.	Manganese	85,000	0-8	10
5.	Sludge	205,000	-	6
6.	Lime dust	58,000	-	-
7.	Limestone	300,000	0-80	2
8.	Dolomite	240,000	0-80	2
9.	Sinter return	1,543,000	0-5	-
10.	Coke	240,000	0-30	4

8.1 The Sinter Machine

The sintering machine installed at Ajaokuta consists of an endless pallets chain and is provided with gear-shaped sprockets for lifting and lowering the pallets at the load and discharge ends respectively in figure 9 above. The foot-shaped guide rails for the lifting and lowering stations are normally designed in such a way that the pallets are separated by both segments and pass from the upper strand to the lower strand without the pallets coming into contact with each other and without being subjected to too much wear. Cross-section of the sinter machine is shown in figure 10.

Major accessories of the sinter machine include;

(1) The ignition and heat treatment load, (2) the pallets and (3) the vacuum chambers

The sinter machine drive is located in the lifting station with the power of electric motor being transferred by the tooth segment of lifting sprockets to the pallet trust rollers. A torsion proof drum connects both lifting sprockets.

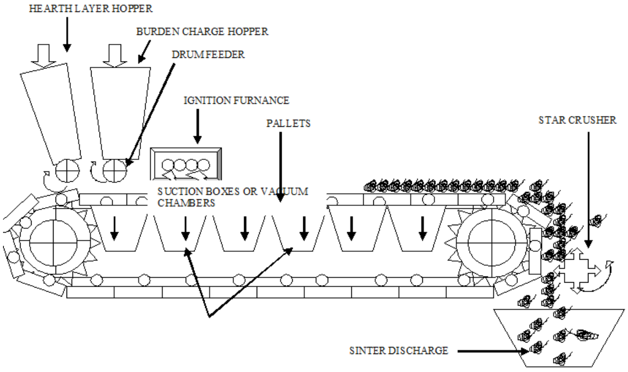

Figure 10. Travelling Grate Sinter Machine

The lifting and lowering sprocket shafts run in anti-friction bearings which are connected to a central lubrication system Shaft mounted gearboxes are used for applying the starting torque. To be able to effect changes on the pallet travel speed, the drive side is equipped with a floating type bearing with adjusTable equipment. Pallet travel speed can then be altered by varying the position of the lifting sprocket relative to the centre line of the sinter machine. A brief description of the major components mentioned above is attempted below:

(1) Pallets: - A typical pallet consists of three main parts namely; the central frame, the sidewalls and the rollers. Depending on the design of the pallet may come as one piece or in three separate parts with the sidewalls and roller bearings attached to the central frames on site. The bottom of the pallets consists of fire grates which are replaceable. The materials for the pallet construction may be cast iron or cast steel.

DOI: https://doi.org/10.30564/jmmr.v3i2.2409

(2) Vacuum Chamber: - Immediately below the sinter machine is the vacuum chamber inside which the rare-faction necessary to draw the process gas is created. To ensure efficient rarefaction, a tight seal must be achieved between movable pallets and stationary vacuum chambers in both longitudinal and traversal direction to the machine. For this purpose, sealing of strips is located on either of each pallet. Strings into the stationary vacuum chamber beams ensuring efficient sealing press the strips. Additionally, sealing plates are installed at the beginning and end of the suction area to effect the cross seal of the vacuum chambers.

(3) Sinter Machine Discharge End: - Sinter was discharged from the sinter machine through a crash deck to a single-roll tooth (star) crusher. Here the sinter was crushed to a maximum size of -250mm. An ideal sinter has the following features:

(a)The crush deck must be lined with special refractory bricks that will cool rapidly to ensure repairs around the roll crusher after only short stoppages.

(b)The parts must be quickly interchangeable to decrease short-down time.

(c)Wear-resistant material must be used in the crushing area.

(d)The geometry of the crushing system (point of impact, crushing angle, co-ordination of crushing facilities etc.) must be optimized.

8.2 Sinter Raw Material Stocking

All the raw materials delivered are crushed and ground to required particle sizes and are stocked in the appropriate stock bins (proportioning bins).

Table 7. Materials in Sinter Stock Bins

S/No.	Type Of Material	Delivery Capacity (t/hr)	Stock Period (hours)	No. of Bins.	Bins Capacity (tons)	No. Of Feeders
1.	Fe-materials	1,300	650	3	2,000	3
2.	Coke breeze	150	11	1	340	2
3.	Limestone/Dolomite	500	16	2	1,350	4
4.	Sinter returns	750	2.5	1	305	2

The operation of the feeders are;

(1) Fe-materials; 2 Feeders on, 1 stand-by.

(2) Limestone and Dolomite; 2 feeders on and 2 stand-by.

(3) Coke breeze; 1feeder on and 1 standby.

(4) Sinter returns; 1 feeder on and 1 stand-by

The purpose of the stocking is to;

(1) Ensure the continuous flow of materials.

(2) To serve as a buffer in case of break down.

(3) To assist in changes in consumption pattern. Good stocking practice makes sure that bunkers and buffers are run alternatively to eliminate caking or hanging of moist material in the bunkers due to long storage.

9. Proportioning Process at Materials Stock Bins

Proportioning means taking the exact amount of quantity of materials by weight required to make a given quantity of product. This proportioning was done at concentrate stockyard, sintering plant stock bins, sinter returns by calibration of feeders, and weigh scales to deliver the required quantity on tons per hour. The chemical analysis and stock level can change the consumption pattern or proportion to give the same quantity and quality of the product. To achieve this, charge calculation will predict the chemical analysis of sinter product. In addition, material balance will give the quantity expected. This calculation should be done as a priority before sampling. At ASCL, proportioning starts at Raw materials stockyard. At Raw materials handling, mill scales, BF Flue dust, manganese ore, sludge, lime dust, are added to the iron ore concentrate during delivery to the stock bins at sintering plant. Limestone and dolomite will be delivered in their consumption ratio to the hammer crushers. Charge calculation to predict the chemical analysis of the Fe-material is essential. This prediction and actual analysis are required for further charge calculation at the stock-bins-building to predict sinter analysis. At this stage, the proportioning processes should be well defined and predictions made. The formula for the supply of limestone and dolomite to the hammer crushers should be well defined as:

Annual consumption of limestone (L) = 300,000 tons

Annual consumption of Dolomite (D) = 240,000 tons

Therefore, consumption ratio = 3: 2.4 = 1: 0.8 = 5: 4

9.1 Primary & Secondary Mixing of Sinter Raw Mix (Pelletizing) Primary Mixing

The proportioned materials are mixed in a drum of dimension φ 4.2m x 12m slightly inclined at 2^{o} 30′ angle. The purpose is to homogenize the material such that each micro-volume of the sinter mix has an equal composition by weight of the materials proportioned.

The degree of homogeneity and the rate of discharge of materials depends on; (i)The speed of rotation of the mixing drum, (ii) Angle of inclination, (iii) Internal structures and (iv)Length of the drum.

The mixing drum has a variable speed control. On internal surfaces, ribs are welded to increase the resident time in the drum, thereby increasing the mixing efficiency. There is provision for water spraying in case of very dry material generating dust in the working area.

DOI: https://doi.org/10.30564/jmmr.v3i2.2409

9.2 Secondary Mixing (Pelletizing)

The homogenized sinter mix is charged into another drum of dimension φ 4.2m x 24m long has provision for water spraying. The purpose of pelletizing is to increase the permeability of the sinter mix. The principle of pelletizing is based on the theory that small wet particles gently rolling over each other stick together with the aid of surface tension of water(liquid) in the presence of binding material (lime or bentonite) forming balls and segregating(Rolling) to the ends For pelletizing the following facts are related;

(1) Speed of rotation of the drum, (2) Angle of rotation, (3) Moisture content (%), (4) Length of the drum.

The speed is inversely proportional to the pellet size. The higher the speed, the smaller the pellets. The higher the angle, the smaller the pellets. There is optimum moisture above or below which the pellet size becomes smaller.

9.3 Quality Control of Sinter

Despite the efforts made in proportioning and calibration there are still errors or malfunctions that are not easily determined until the result of the laboratory tests are obtained. The Detailed Project Report (DPR) specifies the sinter chemical analysis as follows:

Ferrous total = 52%
Manganese (Mn) = 1.06%
Phosphorous (p) = 0.036%
Sulphur (S) = 0.011%
Ferrous Oxide = 13.55%
Ferric Oxide = 60.29%
Manganese Oxide = 1.33%
Silica (SiO_2) = 9.43%
Alumina (Al_2O_3) = 1.00%
Calcium Oxide (CaO) = 12.09%
Phosphorus Pentaoxide = 0.082%
Sulphur Trioxide = 0.021%
Others = 014%

9.4 Charge Calculation to Produce Sinter of Rated Basicity

Initial data for charge calculation are:

$$Sinter\ Basicity = \left(\frac{CaO}{SiO2}\right) = 1.28$$

Table 8. Silica and Lime Content of Raw Materials at Stockyards

S/No	Materials From Stockyards	SiO2	CaO	L.O.I.
1.	Concentrate	9.3	0.66	1.5
2.	Dolomite	4.07	31.02	43.57
3.	Limestone	1.81	53.00	43.76
4.	Coke	7.0	1.00	85.00

Table 9. Material Consumption Rate

S/No.	Type Of Materials	Non-calcined (tons/hour)	Calcined (tons/hour)
1.	Concentrate	278.4	278.4x(100-LOI = 278.4x0.985 = 294.22
2.	Dolomite	29.7	29.7x0.564 = 16.75
3.	Coke	30.3	30.3x0.15 = 4.54
TOTAL			295.61

Calculation of limestone requirement in tons:

1st calculate the amount of silica introduced into the burden charge through other raw materials i.e.

$$\text{Silica } (SiO_2) \text{ in concentrate } = 278.4\,x\ \%\ of\ SiO_2\ in\ Table\ 7$$

$$= 278.4x0.093 = \frac{25.89t}{Hour}$$

$$= 278.4\ x\ 0.093\ =\ 25.89\ t/hr.$$

SiO_2 in Dolomite = 29.7 x % of SiO_2 in Table 7
= 29.7 x 0.041 = 1.22 t/hr.

$$SiO_2 \text{ in Coke } = 30.3\ x\ \% \text{ of } SiO_2 \text{ in Table 7}$$

$$= 30,3\ x0.07 = \frac{29.23t}{Hour}$$

Total SiO_2 introduced through burden charge = 25.89 + 1.22 + 2.12

$$\frac{29.23t}{Hour}$$

= 29.23 t/hr.

The lime requirement to neutralize this silica and maintain the required basicity of 1.28 is given by;

$$\frac{CaO}{SiO2} = 1.28$$

$$\frac{CaO}{29.23} = 1.28$$

$$CaO = \frac{29.23x1.28 = 37.41tonnes}{Hour}$$

Now, to calculate the amount of CaO introduced into the burden charge through other raw materials as indicated in Table 7

DOI: https://doi.org/10.30564/jmmr.v3i2.2409

CaO content in concentrate = 278.4 x % of CaO

$$= \frac{278.4\,x\,0.0066 = 1.84\,tonnes}{Hour}$$

CaO content in Dolomite = 29.7 x % of CaO

$$= \frac{29.7\,x\,0.31 = 9.20\,tonnes}{Hour}$$

CaO content in Coke 30.3 x % of CaO

$$= \frac{30.3\,x0.01 = 0.30\,tonnes}{Hour}$$

Total CaO introduced into the burden charge through other raw materials

$$= \frac{1.84 + 9.20 + 0.30 = 11.34\,tonnes}{Hour}$$

The amount of CaO required to be introduced through the addition of Limestone

$$\frac{37.41 - 11.34\ = 26.07\,tonnes}{Hour}$$

Dry Limestone consumption is given by

$$= \frac{26.07}{(0.5 - CaO\,required\,to\,neutralize\,SiO2\,in\,the\ \ Limestone)}$$

$$= \frac{26.07}{[0.53 - \left(0.0181x1.28\right)]}$$

$$= \frac{51.4\,tonnes}{Hour}$$

Limestone consumption at normal humidity of 2% is

$$\frac{51.4\,x1.02 = 52.43\,tonnes}{Hour}$$

To check for the basicity,

$$Wt\,of\ calcined\,burden = 295.61 + 52.43\,x\,0.56$$

$$Wt\,of\ calcined\,burden = \frac{324.97\,tonnes}{Hour}$$

$$Content\,of\ CaO\,in\,Sinter = \frac{(29.23\,x\,SiO2\,in\,dry\,Limestone)}{324.97}$$

$$Content\,of\ CaO\,in\,Sinter = \frac{(29.23\,x\,51.4\,x\,0.0181}{324.97}\,x\,\frac{100\%}{1} = 9.28\%$$

$$Content\,of\ CaO\,in\,Sinter = \frac{11.34\,x\,0.53\,x\,51.4}{324.97}\,x100\% = 11.87\%$$

$$Basicity\,of\ Sinter = \frac{CaO}{SiO2} = \frac{11.87}{9.2} = 1.28$$

Correction of the amount of Limestone with the charge of calcium oxide content e.g. CaO content decrease to 51%.

To produce Sinter with necessary basicity of 1.28,

$$it\,is\,necessary\,to\,increase\,the\,amount\,of\ \ Limestone\,by$$

$$= \frac{53tonnes}{51tonnes} = 1.039\,times$$

That is, the amount of Limestone after correction will be $51.4\,x1.039 = 53.4\,tonnes$

$$For\,wet\,Limestone = 53.4\ \ x1.02 = \frac{54.46}{tonnes}$$

10. Pollution Control of Working Environment

On a general note, the receiving and stockpiling of various raw materials such as Iron ore concentrate and fluxes generate a substantial quantity of dust during handling through chutes and along with conveyor belts, especially in underground handling facilities. Dust pollution is hazardous to workers respiratory system; it causes chronic occupational diseases such as Silicosis, Pneumoconiosis, etc. For that reason, all the dust-generating points within the materials handling facilities of ASCL are connected with a network of dust extraction pipes by means of induced draught Fans using either Electrostatic precipitator, Venturi scrubber or Fibre bag filter as the case may be, recovered dust is recycled back into the system. This singular advantage of cleaning the working environment and recycling the scarce and expensive raw materials back into the process line that could have been lost to the atmosphere justify the huge capital investment in their installation. The technical and process description of the three types of aspiration plants used will be briefly discussed below.

11. Electrostatic Precipitator Technical Description

Electrostatic precipitator consists of the following:

(1) A rectangular sections of the diffuser (for gas inlet) and confuser (for gas outlet) adjoined to section's faces; (2) Hoppers at the lower part of the housing to collect and remove the recovered dust; (3) Housing is covered by glass fiber in some units as a heat insulator to prevent cooling of process gases, which could lead to moisture condensation of noxious gases (SO_2 and H_2O) because of temperature drop; (4) Collecting electrodes, discharge electrodes, jolting mechanisms of the electrode, insulator units and gas-distributing grids are

DOI: https://doi.org/10.30564/jmmr.v3i2.2409

assembled inside the housing; (5) Discharge electrodes are connected at the top to a high-voltage feed source of rectified current 50-60 KV; (6) Collecting electrodes are earthed through the body of the housing; (7) Sidewalls of housing are solidly made from 6mm thick steel plates with horizontal ribs to provide structural stability; (8)Housing roof has an aperture used for assembly of equipment and installation of insulators; (9) Gas distributing grids were installed at diffuser (gas inlet) side to distribute gas evenly along all sections of the electric filter; (10) Collecting electrode of frameless construction is arranged in the vertical position in the same plane and all cells must be parallel to each other. Each cell is 640mm wide and hung to suspension beams by brackets; (11) Jolting beam consists of two strips 10 x 80mm connected between them by anvil from the impact end, and from the opposite by insert; (12) Discharge electrodes are flat bar frames with taut tape-needle members, turn of needles are directed parallel to gas flow; (13) All electrodes are installed on suspension frames by means of brackets. Suspension frames support top brackets freely; threaded joints of lower brackets are tightened and welded round; (14) Suspension frames of discharge electrodes together with the discharge electrodes form a common system, which was hung on suspension pipes, china base through high tensile strength insulators, and it is adjustable; (15) Jolting mechanism of discharge electrode has a reciprocating motion with provision for adjustments. Maximum the angle of lift of hammer is 60° and height of lift is 100 mm; (16) Jolting mechanism of collecting electrodes was assembled by blocks. Each block consist of a shaft with hammers, couplings and bearings mounted on the frame. The shaft of blocks are connected together by couplings, and frames are fixed to the housing; (17) Jolting mechanism of both electrodes is driven by means of gear motors mounted on speed reducers with maximum. The output torque of 150kgnm and 0.2rpm; (18) A combined units of disc gate and sluice feeders are installed bellow the hoppers for continuous discharge of collected dust to scrapper conveyor for recycling and (19) Hatches and doors are provided for accessibility into the ESP during inspection and repairs.

12. Process Description

Electrostatic precipitator operates based on the principle that; When two electrodes are connected to a high rectified voltage of 50-80KV, a coronary discharge of electrons from highly insulated negative (discharge) electrode to earthed positive (collecting) electrode occur.

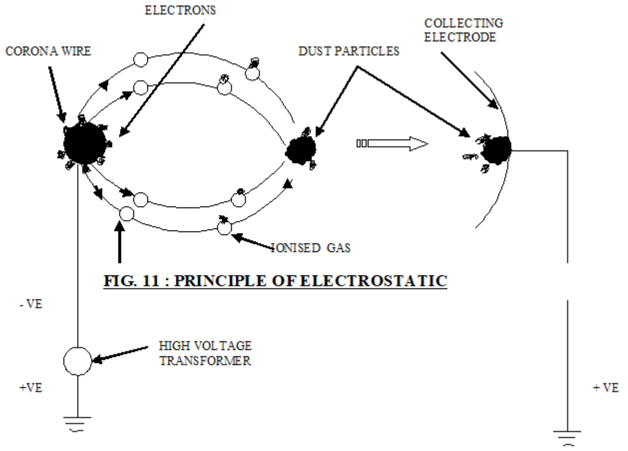

Figure 11. Principle of Electrostatic Precipitator

The corona discharge from highly insulated negative (discharge) electrode ionizes the gases and the ions become attached to the dust particles, then rapidly across to the earthed collecting electrode from which they are removed at regular intervals by means of jolting mechanism and the dust particles are collected at the bottom hopper. The transit time through the cells must be sufficient to allow each particle to travel across the width of the cells (electrodes) under electrostatic forces that is applied to it. The high-voltage rectified current is led to electrodes of ESP along high voltage cable. At the rectifier, positive terminals are earthed while negative terminals are properly insulated and connected to discharge electrode through high voltage cable. High-voltage, low current is supplied to discharge electrode, the electric field is generated in the ESP between discharge and collecting electrodes. Voltage quantity of the field is increased automatically by a thyristor-controlled circuit until the maximum voltage of 80 kV is reached. As the voltage increase approaches maximum, corona discharge arises in the space between the two electrodes. Induced Draught (ID) Fan suck process gases containing dust particles through the ESP, weighted particles contained in gases are admitted into ESP through the diffuser and gas-distributing grids for uniform gas distribution throughout the ESP chamber. They are ionized and carried by the moving ions. Ionized particles under the influence of electric field move to collect electrodes and settle them temporarily, cleaned gases continue to move through the electric field until it reaches confuter at the end of ESP and flows through the gas duct to ID Fan and stack. The temperature must be maintained above due points of both Sulphur dioxide and steam because of their deleterious effect of corroding the structural members and ID fan impeller blades. Once the maximum voltage is reached, the thyristor cut-off the voltage to zero and the

DOI: https://doi.org/10.30564/jmmr.v3i2.2409

jolting mechanism rap and shake the collecting electrodes thereby dropping the collected dust particles inside the hopper below. The circle is repeated throughout the operating time, collecting dust in the hopper is periodically and incessantly removed by means of sluice feeder and scrapper conveyors back to the process line.

12.1 Technical Description of the Venturi Scrubber

Venturi scrubber consists of the following: (1) The venturi scrubber of model KMP-8 consists of a venturi tube (tube-coagulator) with a hydraulic seal which creates a water curtain at the bottom discharge end; (2)The venturi tube consists of a casing, 30mm jet nozzle and water chamber for water film spraying along the inner surface of the venturi tube expander with a combined flow rate of 31.5m^3/hr.; (3) The venturi tube was of welded design and consists of an air inlet pipe from the top, which admits air at the rate of 105,000m^3 /hour, a throat and expander. Main water supply was provided through the 30mm jet installed at the central axis of venturi throat, the jet nozzles are easily detachable; (4) Additional water supply for the chamber flowing down in the shape of a uniform film along the entire inner surface of the venturi tube was also provided; (5) When filling the chamber with water, a hydraulic seal preventing air in-leakage from the environment is created; (6) When filling the chamber with water, a hydraulic seal preventing air in-leakage from the environment is created, Water was supplied to the chamber through the semi-circular 25mm pipe and two numbers. 25mm gate valves connected to the chamber's outer periphery The chamber was covered with Iron sheets at the top; (7) Openings for removal of sludge during repairs and cleaning are provided at the bottom discharge outlet; (8) The spray tower of type ЗИΛ-900 (drop catcher) consists of a casing and a branch pipe in the lower part meant for air supply from venturi (coagulator) and a scroll used for removal of cleaned air at the top of the spray tower. Cleaning efficiency that can be achieved is up to 97.5% and dust particles in the emissions not to exceed 1.43mg/m^3; (9) Sludge formed as a result of gas cleaning is removed from spray tower through the hydraulic seal in the lower the casing. For periodic flushing, the part of hydraulic compartment was supplied with water through 25mm gate valve; (10) For flushing of internal walls of spray tower, periodic spraying of the walls by means of nozzles installed at the upper part of the casting was done. Water is supplied to the nozzles through a circular pipe around the circumference of the spray tower; (11) For observation and visual inspection of the inner wall of the spray tower, an inspection man-hole is provided, 2 Nos. Instrumentation cabinets are provided at the ground floor with gauges for measuring suction pressure from 0-63kgf/m^2 and water flow rate from 0-50m^3/hour, a switch knob for starting and stopping the system was also provided by the side of the instrumentation cabinet; (12) Suction of dust-laden gas through the venturi scrubber is achieved by an exhauster fan of type D18X2Twith a capacity of 180,000m^3/hour, it was driven by a high tension electric motor with a power rating of 320KW and 6.6KV supply; (13) The exhauster motor was interlocked with maximum sludge level sensor in the spray tower and main water supply motorized gate valve.

12.2 Process Description

Venturi technically means narrows to a throat and then gradually increase to the original diameter, it was used in fluid mechanics to generate turbulence flow in fluids.

The basic principle of the venturi scrubber (wet coagulation dust catcher) is to provide intimate contact between the collecting fluid and the contaminant in the air to be cleaned. When the contaminant is particulate, the wetting of the particle increases its mass and it becomes relatively easy to remove from the air stream. The intimate mixture of air and liquid provides a large interface area between the two media so that solution or reaction of the contaminant was enhanced; the efficiency increases with pressure drops. In venturi scrubber type KMP-8, the contaminant air is passed through a venturi throat at a very high velocity of about 100m/sec and flow rate of 105,000m^3/hr. Water, which is simultaneously fed in at a rate of 31.5m^3/hour into the throat was atomized by the turbulent air into a fine fog. The intimate mixing of the contaminant and water in the turbulence created by the venturi results in rapid wetting and collection, pressure losses is as high as 330mm (13.2 inches) and the efficiency of separation is estimated at 97.5% in the sub-micron particle size range.

13. Fibre Cloth Bag Filter: Technical Description

Fibre cloth bag filter (Bag filter) consists of the following: (1) Each unit is made up of rectangular box measuring 6000mm x 2000mm x 2200mm divided into eight compartments each measuring 1500mm x 100mm x 2200mm; (2) Each compartment contain 24 Numbers of bag filters, a total of 96Nos. for each unit of eight compartments; (3) Dimension of each bag was □200mm x 2200mm height; (4) Each bag is hooked with a spring from the top end in addition to bag clamp to prevent the downward collapse of the bag in the event of upper clamp failure to grip; (5) Each compartment is provided with a baffle at the bottom end entrance into bags compartment for controlling alternate exhauster suction and counter flow of compressed air supplied by solenoid valves; (6)Each compartment is provided with an electrically activated programmed solenoid valve for controlling compressed air supply for the purpose of cleaning filter bags; (7) Bottom hoppers of all the eight compartments are connected with a common pipe for discharging the collected dust back to process line; (8) The exhauster fan model ци6-45N8 has a capacity of 15,500m^3/hour with 37KW electric motor or model ци6-45N8 which has a capacity of 8,100m^3/hour with 22KW motor depending on specific design requirement, the type installed in each unit depends on the dust emission rate in the unit. There are a total of 24 units in the whole section under study; (9) A start and stop push button switch is provided near each exhauster fan motor and (10) Electro-pneumatic programmed box is mounted on each control panel board (CPB) controlling each exhauster fan motor.

Process Description

By sucking action of exhauster fan through suction hoods, dust-laden air enters one section of the fabric and emerges through the other side as cleaned air and discharge to the atmosphere through the chimney. The cleaning process is not simple filtration since the pores of the medium are usually much larger than the particles to be collected. When the cloth bag filter is new, much dust will pass through the filter until a bed of deposited dust was built upon the fabric. The process was complicated, it involves impingement of the particles on the fibres, as well as deposition of the particles under the influence of settling, Brownian motion and static electricity created by flowing air. The dust mat will rapidly build upon the medium, and it was this mat, rather than the fabric, which acts as the filtering agent.

A permanent dust base will be created within the pores, which will not be dislodged by shaking so that cleaning efficiency remains high. The most commonly used fabric medium for normal application such as cleaning of concentrate, fluxes and coke dust is cotton or wool sateen/felt. The size of the filter, i.e. the area of filter medium through which a given stream of air passes, will affect the resistance to airflow and therefore the required exhauster fan motor with a power rating of 37KW and 22KW was installed at different units depending on projected (anticipated) dust emission. Normal resistance (i.e. pressure drops) of the filter to flow of air with a ratio of 3 to 1 used was 75mm of water.

An important feature of the design of bag filters is the inflation of the bags during suction and their sudden collapse during counter-current flow of compressed air, which serves as a shaking mechanism during a circle of bag cleansing. When the solenoid valve is activated, it releases a pressurized compressed air which was deflected upward into bags compartment by a baffle at the same time blocking suction from exhauster fan from below. Compressed air was blown through the fabric in a counter-current to the flow of clean air, which equally serves as a shaking mechanism to the bags. The shaking mechanism must vigorously rap, shake and flex the fabric to discharge the dust, which may adhere very firmly.

The shaking circle must as indicated be frequent enough to ensure continuous maintenance of the designed filtration rate, an automatic interlock between exhauster fan motor solenoid valves is provided such that the solenoid programmer was only activated when the exhauster fan motor is switched on. The material caked on the cloth was continuously dislodged from the surface and since it is agglomerated, is not restrained in the airstream but fall to the collecting hopper. The resistance after the initial build-up is essentially constant at the suction hoods, branch pipe velocity of 1,350-1,670 meters per minute for concentrate, fluxes and coke specks of dust were adopted.

14. Conclusion and Recommendation

There is no gainsaying the fact that an integrated steel plant like Ajaokuta Steel Company Limited can only be successfully operated with a sure guarantee of regular and timely supplies of bulk raw materials input. The bulk raw materials requirements like Iron ore concentrate, limestone, dolomite and coking coal are locally sourced and are available in the country except for coking coals which require high-grade foreign coals to be blended with low-grade local coal.

Therefore, adequate planning and logistics for their exploitation and transportation to site via road and railway systems, storage and handling will ensure not only the smooth operations but also the economic promotions for various operations of an integrated Iron and Steel Plants.

The various types of machinery and facilities made available on site for the bulk materials handling are so designed to ensure smooth expansions from the initial 3 million tonnes, to 2.6 million tonnes and 5.6milion tonnes signifying the first, second and third phases of liquid steel production per annum at ASCL.

The provision of highly rated and tested tipping, off-loading and stocking facilities at various stockyards was a significant assurance of uninterrupted operations. The advantages of the suggested techniques of stocking and blending are:

(1) Reduction of the overall price of raw material uti-

DOI: https://doi.org/10.30564/jmmr.v3i2.2409

lized, by carefully balancing the rich and poor materials to obtain the desired overall requirement in a burden; (2) During shortage conditions of the grade of material normally utilized, a blending system is sufficiently flexible to make possible the use of lower or higher grade of materials, which are readily available; (3) Almost invariably, variations of physical and chemical characteristics occur within different sections of a mine, and if a blending operation was incorporated, the extra expense of selective mining in order to obtain a measure of uniformity within the burden can be reduced; (4) The use of blended ores in the blast furnace prevents the local agglomeration of fine ores which fills the natural voids and obstruct the free flow of gas through the stack; excessive voids created by lump concentration causing hot sports are also eliminated; (5) Demurrage charge on railway wagons can be greatly reduced if carefully planned blending facilitates quick turn round; (6) Material bedded out before reclaiming provide buffering for breakdown emergencies of incoming materials; (7) The extension of raw material reserves is possible by making use of lower grade materials readily accepTable with blending and bedding; (8) Some of the coals used for coking ovens are prone to spontaneous combustion and cannot be safely stored for more than three weeks. When these are blended with coals of differing characteristics, the possibility of spontaneous combustion was reduced to a minimum; (9) There is an increase in the coke oven linings due to the charge being consistency at all times and (10) Due to the evening out of the chemical characteristics of ore fines for sintering, the consumption of coke (coke rate) during the process can be reduced, depending on the lime/silica ratio. This is obviously more economical. However, it must be pointed out here that a careful balance must be maintained between lime at the sinter plant and limestone at the Blast furnace.

Conflict of Interests

The authors declare that there is no conflict of interests regarding the publication of this paper.

References

[1] Detailed Project Report (DPR) of Ajaokuta Steel Company Ltd; By TiajPromeExport (TPE) of Russia 1980c

[2] Caen-Vachette, M., Umeji, A. C. Geology and Geochronology of the Mfamosing area. Evidence of crystalline Limestone formation in economic quantity. J. Afr. Earth Sci., , 1987, 7: 121-126.

[3] Mogbo, O., Okoro, A.U., Oluyede, P. O., Muotoh, E. O. G. The Itakpe Hills Iron Ore formations. First Symposium on the Precambrian Geology of Nigeria, Kaduna, 1981

[4] Kennedy, W. Q. Analysis of Bulk Materials Blending Techniques and Related Equipment. 8th Annual Report American Institute of Metallurgy, 1984, 61: 243-250.

[5] PACS-MECON (India). Annual Report on Ajaokuta Steel Company. 1986: 156-167.

[6] Linchersky, B. Iron and Steel making. 4th edition, 1990

[7] U.S.Steel Publication: The Making, Shaping and Treating of Steel, 19th Edition, 1975.

[8] Basic Oxygen Furnace Steelmaking: https://www.steel-technology.com/articles/oxygen/furnace

[9] E.T. Turkdogan "Fundamental of Steel Making" The Institute of Materials Book 656, First Published by the Institute of Materials 1 Carlton House Terrace London SW1Y 5DB, 1996.

[10] Carl-Erik Grip, Johan Isaksson, Simon Harvey, Leif Nilsson. Application of Pinch Analysis in an Integrated Steel Plant in Northern Sweden. ISIJ International, 2013, 53(7): 1202-1210.

[11] C. Mapelli and S. Baragiola: Ironmaking Steelmaking, 200633: 379.

[12] C. Ryman: Iron Steel Technol., 2011, 8: 61.

[13] C. E. Grip, M. Larsson and J. Dahl: Proc. 84th Steelmaking Conf., ISS, Warrendale, PA, 2001: 543.

[14] Dawson, P. R., Ironmaking Steelmaking, 1993, 20: 137-143.

[15] Hsieh, L. H., Proc. On Iron and Steel Tech. Conf. Indianapolis, IN, USA. Association for Iron and Steel Tech., Warrendale, PA, USA. 2007, 1: 207-214.

[16] Cumming, M. A. and Thurlby, J. A., Ironmaking Steelmaking, 1990, 17: 245-254.

[17] Cappel, F., ISS Ironmaking Conf. Proc., 1991, 50: 200.

[18] Yamaoka, Y., Nagaoka, S., Yamada, Y., Ando, R., Trans. Iron Steel Inst. Jpn., 1974, 14: 185-194.

[19] D. Fernández-Gonzáleza, I. Ruiz-Bustinzab, J. Mochónb, C. González-Gascac, L. F. Verdeja. Iron Ore Sintering: Process" Mineral Processing And Extractive Metallurgy Review 2017, 38(4): 215-227. http://DX.DOI.Org/10.1080/08827508.2017.1288115

[20] Fernández-González, D., Martín-Duarte, R., Ruiz-Bustinza, I., Mochón, J., González-Gasca, C., Verdeja, L. F. Optimization of sinter plant operating conditions using advanced multivariate statistics: Intelligent data processing. JOM, 2016, 68: 2089-2095.

[21] Fernández- González, D., R., Ruiz-Bustinza, I., Mochón, J., González-Gasca, C., Verdeja, L. F. Iron ore sintering: Raw materials and granulation. Mineral

Processing and Extractive Metallurgy Review, 2017, 38: 36-46.
[22] Ishikawa, Y., Kase, M., Sasaki, M., Satoh, K., Sasaki, S. Recent progress in the sintering technology- High reducibility and improvement of fuel consumption. Ironmaking Conference Proceedings, 1982, 41: 80-89.
[23] Ishikawa, Y., Shimomura, Y., Sasaki, M., Hida, Y., Toda, H. Improvement of sinter quality based on the mineralogical properties of ores. Proceedings of the 42th Ironmaking Conference, AIME, Atlanta, 1983: 17-29.
[24] Yang, W., Choi, S., Choi, E. S., Ri, D. W., Sungman, K. Combustion characteristics in an iron ore sintering bed: evaluation of fuel substitution. Combustion and Flame, 2006, 145: 447-463.
[25] Yasumoto, S., Tanaka, S. Continuous measuring of heat pattern in sintering bed and its application to sintering operation. Kawasaki Steel Technical Report, 1982, 5: 1-8.
[26] Otomo, T., Taguchi, N., Kasai, E. Suppression of the formation of large pores in the assimilated parts of sinter produced using pisolitic ores. ISIJ International, 1996, 36: 1338-1343.
[27] Dawson, P. Determination of the high temperature properties of blast furnace burden materials. SEAISI (South East Asia Iron and Steel Institute) Quarterly Journal, 1987, 16: 23-42.
[28] Loo, C. E., Matthews, L. T., O'Dea, D. P. Lump ore and sinter behavior during softening and melting. ISIJ International, 2011, 51: 930-938.
[29] Eisele, T. C., Kawatra, S. K. A review of binders in iron ore pelletization. Mineral Processing and Extractive Metallurgy Review, 2003, 24: 1-90.
[30] Patisson, F., Bellot, J. P., Ablitzer, D., Marlière, E., Dulcy, C., Steiler, J. M. Mathematical-modeling of iron-ore sintering process. Ironmaking and Steelmaking, 1991, 18: 89-95.
[31] Dawson, P. R., Ostwald, J., Hayes, K. M. The influence of sintering temperature profile on the mineralogy and properties of iron ore sinters. Proceedings of the Australian Institute of Mining and Metallurgy, 1984, 829: 163-169.
[32] Usamentiaga, R., Molleda, J., García, D. F., Bulnes, F. G. Monitoring sintering burn-through point using infrared thermography. Sensors, 2013, 13: 10287-10305.
[33] Toda, H., Senzaki, T., Isozaki, S., Kato, K. Relationship between heat pattern in sintering bed and sinter properties. Transactions of the Iron and Steel Institute of Japan, 1984, 24: 187-196.
[34] Hsieh, L., Liu, K. Influence of material composition on the softening and melting properties of blast furnace burden materials. Ironmaking Conference Proceedings, 1988, 57: 1623-1632.

DOI: https://doi.org/10.30564/jmmr.v3i2.2409

BILINGUAL PUBLISHING CO.
Pioneer of Global Academics Since 1984

Journal of Metallic Material Research
https://ojs.bilpublishing.com/index.php/jmmr

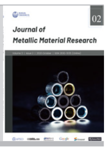

ARTICLE

Study of the Formation Conditions of Aluminum Oxide Nanoparticles in an Overstressed Nanosecond Discharge Between Aluminum Electrodes in a Mixture of Nitrogen and Oxygen

A.K. Shuaibov* **A.Y. Minya** **A.A. Malinina** **A.N. Malinin** **Z.T. Gomoki** **V.V. Danylo** **Yu.Yu. Bilak**

Uzhgorod National University, st. Voloshin, 54, 88000, Uzhgorod

ARTICLE INFO

Article history
Received: 9 October 2019
Accepted: 29 October 2019
Published Online: 30 November 2020

Keywords:
Electrical and optical characteristics of plasma
Luminescence of nanostructures
Aluminum oxide
Overstressed nanosecond discharge
Nitrogen
Oxygen

ABSTRACT

The results of the study of oscillograms of voltage, current, pulsed electric power and energy input into the plasma of an overstressed nanosecond discharge between aluminum electrodes in argon and mixtures of nitrogen with oxygen (100-1) at pressures in the range of 13.3-103.3 kPa are presented, the emission plasma spectra are studied. It is shown that in mixtures of nitrogen with oxygen at atmospheric pressure, nanoparticles of aluminum oxide (Al2O3) are formed, the luminescence of which manifests itself in the spectral range of 200-600 nm and which is associated with the formation of F-, F + - centers and more complex aggregate formations based on oxygen vacancies. Calculations of the electron-kinetic coefficients of plasma, transport characteristics, such as mean electron energies in the range 5.116-13.41 eV, are given. The electron concentration was $1.6 \cdot 10^{20}$ m^{-3} - $1.1 \cdot 10^{20}$ m^{-3} at a current density of $5.1 \cdot 10^6$ A / m^2 and $1.02 \cdot 10^7$ A / m^2 on the surface of the electrode of the radiation source ($0.196 \cdot 10^{-4}$ m^2). Also drift velocities, temperatures and concentrations of electrons, specific losses of the discharge power for elastic and inelastic processes of collisions of electrons per unit of the total concentration of the mixture from the reduced electric field strength (E / N) for a mixture of aluminum, nitrogen, oxygen, rate constants of collisions of electrons with aluminum atoms on the E / N parameter in plasma on a mixture of aluminum vapor, oxygen and nitrogen = 30: 1000: 100000 Pa at a total mixture pressure of P = 101030 Pa are given.

1. Introduction

In works [1,2], the results of studying the kinetics of processes in a heterogeneous plasma based on mixed flows of a buffer gas - argon, an oxidizer (water molecules), and aluminum dust are presented. Plasma of various types of discharge (glow, pulsed and combined) in gas-vapor mixtures of argon, water, and aluminum dust was studied. In the plasma under study, aluminum dioxide is formed at the high-voltage electrode in the form of a developed flaky surface, and thermal energy is released [1]. The cost of producing a hydrogen molecule in such a reactor does not exceed 1.5 eV / molecule, which is much more economical than the hydrolysis method for produc-

---

**Corresponding Author:*
A.K. Shuaibov,
Uzhgorod National University, st. Voloshin, 54, 88000, Uzhgorod;
Email: alexsander.shuaibov@uzhnu.edu.ua

DOI: https://doi.org/10.30564/jmmr.v3i2.2441

ing hydrogen. In order to simplify the design of the reactor, it is important to replace the generator of aluminum dust by producing microdroplets of aluminum by exploding microtips on the surface of aluminum electrodes in a strong electric field of a nanosecond discharge (formation of ectons [3]). Moreover, it is also important to establish the type of nanostructures of aluminum oxide and obtain it in the form of a thin nanostructured film.

In [4,5], the electrical and optical characteristics of a spark discharge are given, the current and voltage of which had an oscillatory form in the microsecond range. The discharge was ignited between aluminum and graphite electrodes in air and was investigated by time-resolved emission spectroscopy. The studies were carried out in the discharge ignition mode far from the overstress of the discharge gap. Vapor of electrode materials entered the plasma as a result of sputtering under the action of a spark discharge (the duration of the current oscillation train was about 25 μs, and one full oscillation was 5-6 μs).

Aluminum oxide nanopowders were synthesized by the gas-phase method in [6]. With this method of nanopowder formation, a drop of molten aluminum was held in vacuum by a high-frequency field and flowed around with an argon and oxygen flow. Aluminum vapors were carried away to a colder zone, where they condensed and oxidized. The obtained aluminum oxide powder with particle sizes of 60 and 15 nm was pressed, annealed in air, and its photo and cathodoluminescence were studied.

In a subnanosecond high-voltage discharge between aluminum electrodes in air, the characteristics of an aluminum plasma at atmospheric pressure were investigated for the ectonic mechanism of aluminum vapor injection into the discharge gap [7]. The production of vapor of electrode materials was most effective in the absence of matching between the output resistance of the high-voltage modulator and the resistance of the discharge gap. Under these conditions, the deposition of structures based on sputtered copper electrodes 1- 10 in length and 1 μm in diameter was observed on the walls of the discharge chamber.

We are not aware of any works on the synthesis of nanostructures of aluminum oxide using an overstressed nanosecond discharge of atmospheric pressure with an ectonic mechanism [3] of injection of aluminum vapor into the plasma of an oxygen-containing gas. The results of such studies of the synthesis conditions and some characteristics of the nanostructures of copper, zinc, and iron oxides are given in our article [8].

In addition, the plasma parameters of such discharges remain practically unexplored, which does not allow targeted work to optimize this technology for the synthesis of alumina nanostructures using an overstressed nanosecond discharge in nitrogen with a small addition (at the level of 1%) of oxygen.

This work presents the results of studying the conditions for the formation and characteristics of luminescence of nanoparticles of aluminum oxide in the plasma of an overstressed nanosecond discharge of atmospheric pressure in mixtures of nitrogen with oxygen and nitrogen at atmospheric pressure between aluminum electrodes, and also modeling the electron-kinetic coefficients of the plasma and transport characteristics for the mixture under study.

2. Experimental Technique and Conditions

A nanosecond discharge in mixtures of nitrogen and oxygen (mixture composition 100-1) and argon was ignited in a 3-liter dielectric chamber between aluminum electrodes. The diagram of the discharge device is shown in Figure 1. At a distance of 30 mm from the center of the discharge gap, a glass substrate was installed, which served for the deposition of thin films from the products of the sputtering of the electrode material and the products of the destruction of the gaseous medium. The diameter of the aluminum cylindrical electrodes was 5 mm. The radius of curvature of the working end part of the aluminum electrodes was 3 mm. The pressure of the gas mixture and argon was varied in the range of 50 - 202 kPa. The distance between the electrodes was 2 mm. Aluminum vapors were introduced into the discharge gap due to microexplosions of surface irregularities of aluminum electrodes in a strong electric discharge field and the formation of ectons [3].

To ignite the discharge, high-voltage bipolar pulses with a total duration of 50-100 ns and an amplitude of ± (20-40) kV were applied to the electrodes.

The discharge was photographed using a digital camera. The distance between the electrodes was used as a scale for determining the plasma volume. At an interelectrode distance of 2 mm, the discharge gap was strongly overstressed. The nanosecond discharge at a pressure of p = 50-202 kPa was rather uniform.

The voltage pulses across the discharge gap and the discharge current were measured using a broadband capacitive divider, a Rogowski coil, and a 6-LOR 04 broadband oscilloscope. The time resolution of this recording system was 2-3 ns. The pulse repetition rate was varied in the range f = 35-1000 Hz. To record the emission spectra of the discharge, an MDR-2 monochromator, a FEU-106 photomultiplier, a dc amplifier, and an electronic potentiometer were used. Plasma radiation was analyzed in the spectral region 200-650 nm. The plasma radiation registration system was calibrated against the radiation of a deuterium lamp in the spectral range of 200-400 nm and a band lamp

DOI: https://doi.org/10.30564/jmmr.v3i2.2441

in the range of 400-650 nm. The pulse electrical power of the overstressed nanosecond discharge was determined by graphically multiplying the oscillograms of voltage and current pulses. Time integration of the pulsed power made it possible to obtain energy in one electric pulse, which was introduced into the plasma. The experimental technique and conditions are described in more detail in [8].

Thin films based on the destruction products of aluminum electrodes and oxygen molecules were deposited on glass substrates during 2-3 hours of reactor operation. The resulting films were tested for light transmission in the visible wavelength range. The experimental technique and technique for recording the transmission spectra of the synthesized films are described in [9].

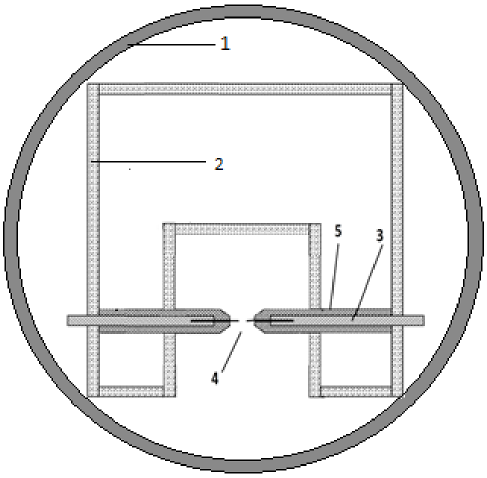

Figure 1. The design of the gas-discharge module: 1 - housing, 2 - fixing the system of electrodes made of plexiglass, 3 - control system for the distance between the electrodes, 4 - electrodes made of aluminum, 5 - insulators made of fluoroplastic

3. Spatial, Electrical and Optical Characteristics

The plasma volume depended on the repetition rate of voltage and current pulses and in the frequency range of 10- 150 Hz it increased from 3 to 30 mm^3. The discharge had a diffuse shape in the form of a sphere. The reason for obtaining a diffuse discharge in gases at atmospheric pressure may be the preionization of the discharge gap by a runaway electron beam with a duration of about 130-150 ps, which is formed at high values of the parameter E/N (where: E is the electric field strength, N is the density of particles in the discharge) [10]. It was experimentally established in [11] that even when using high voltage pulses with a leading edge duration of about 200 ns, a runaway electron beam with an intensity of only an order of magnitude less is formed in the discharge plasma in atmospheric pressure air, even in the same discharge at an air pressure of 13 kPa.

The most typical oscillograms of voltage and current pulses for an overstressed nanosecond discharge between aluminum electrodes in Argon and a mixture of nitrogen with oxygen are shown in Figure 2 and 3. Due to the mismatch between the output resistance of the pulsed high-voltage modulator and the plasma resistance, the voltage pulse had the form of individual spikes with a duration of 7 -10 ns. This mode of ignition of a subnanosecond high-voltage discharge between metal electrodes in the form of a needle and a flat metal plate (or grid), when the total duration of a train of 10 nanosecond voltage pulses was 1-1.5 μs, was used in [7] to obtain plasma jets from a material electrodes. It is promising for the deposition of thin metal films on solid substrates of highly dispersed powders based on electrode materials and products of destruction of molecules of a gas medium.

The maximum value of the positive and negative components of current pulses reached 300 A, voltage amplitudes of 30-40 kV. An increase in the argon pressure in the discharge gap to 101 kPa led to an increase in the plasma resistance and an increase in the matching between the output of the high-voltage modulator and the discharge. Therefore, with an increase in the argon pressure from 50 to 101 kPa, the energy input to the plasma in one discharge pulse increased from 226 to 441 mJ.

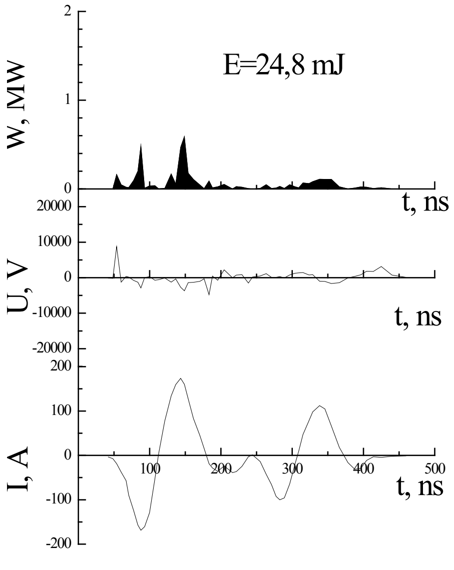

Figure 2. Oscillograms of current, voltage, pulsed power of the discharge, and energy input to the plasma in one discharge pulse at an argon argon pressure of 13.3 kPa

DOI: https://doi.org/10.30564/jmmr.v3i2.2441

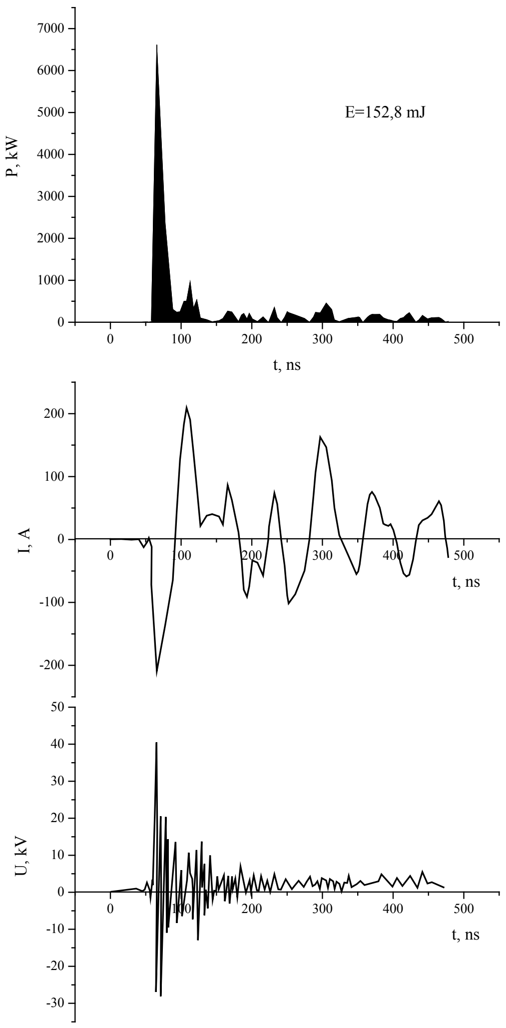

Figure 3. Oscillograms of voltage and current pulses at a pressure of a nitrogen and oxygen mixture of 100 kPa-1 kPa

With an increase in the pressure of the mixture of nitrogen and oxygen (1001) from 50 to 101 kPa, the maximum value of the pulsed electric power of the discharge increased from 3 to 6.3 MW, and the maximum energy input per pulse increased from 110 to 153 mJ.

Figure 4 and 5 present plasma emission spectra of an overstressed nanosecond discharge between aluminum electrodes in a mixture of nitrogen and oxygen and argon. Experiments with argon, which were carried out in the same pressure range as with air, were carried out in order to demonstrate the absence of emission bands of nanostructures of aluminum oxides in the plasma of inert gases (where, in principle, there are no oxidizer molecules).

It can be seen from Figure 4 and 5 that the emission intensity of the discharge plasma in air at all pressures studied by us exceeds the emission intensity of the spectral lines and discharge bands in argon. In the spectra of plasma radiation based on mixtures of nitrogen and oxygen, a small admixture of aluminum vapor recorded radiation on the transitions of the atom and singly charged aluminum ion, nitrogen oxide radicals and nitrogen molecules, as in the emission spectra of a subnanosecond discharge plasma [7]. In the discharge based on argon, radiation was mainly recorded at the transitions of the atom and ion of aluminum (Table 1).

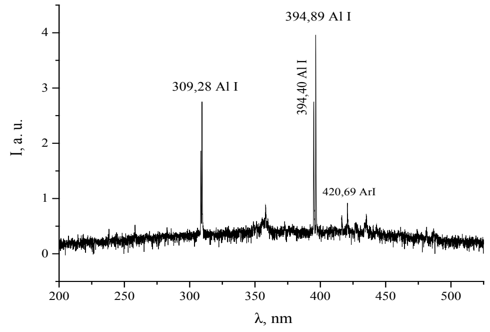

(1)

Table 1. The results of decoding the emission spectra of the discharge between the electrodes from aluminum in argon (Figure 4)

Wavelength, nm	Particle	Transition	Terms	Lower energy level, eV	Upper energy level, eV
308.21	Al I	$3s_2(^1S)3p-3s_2(^1S)3d$	2P*-2D	0.000000	4.021485
309.27	Al I	$3s_2(^1S)3p-3s_2(^1S)3d$	2P*-2D	0.013893	4.021651
309.28	Al I	$3s_2(^1S)3p-3s_2(^1S)3d$	2P*-2D	0.013893	4.021485
394.40	Al I	$3s_2(^1S)3p-3s_2(^1S)4s$	2P*-2S	0.000000	3.142722
394.89	Ar I	$3s^23p^5$(2P*<3/2>)4s- $3s^23p^5$(2P*<3/2>)5p	2[3/2]*-2[1/2]	11.548350	14.687120
396.15	Al I	$3s_2(^1S)3p-3s_2(^1S)4s$	2P*-2S	0.013893	3.142722
415.85	Ar I	$3s^23p^5$(2P*<3/2>)4s- $3s^23p^5$(2P*<3/2>)5p	2[3/2]*-2[3/2]	11.548350	14.528910
419.83	Ar I	$3s^23p^5$(2P*<3/2>)4s- $3s^23p^5$(2P*<3/2>)5p	2[3/2]*-2[1/2]	11.623590	14.575950
420.06	Ar I	$3s^23p^5$(2P*<3/2>)4s- $3s^23p^5$(2P*<3/2>)5p	2[3/2]*-2[5/2]	11.548350	14.499050

DOI: https://doi.org/10.30564/jmmr.v3i2.2441

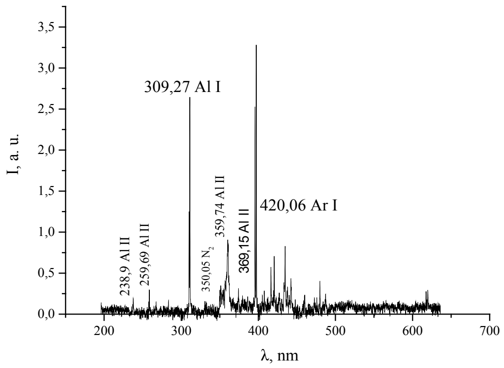

(2)

Figure 4. Radiation spectra of overstressed nanosecond discharge at argon pressures 1 - 13.3 kPa, 2 - 101.3 kPa

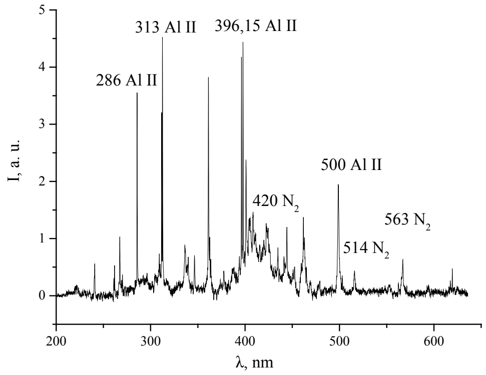

(1)

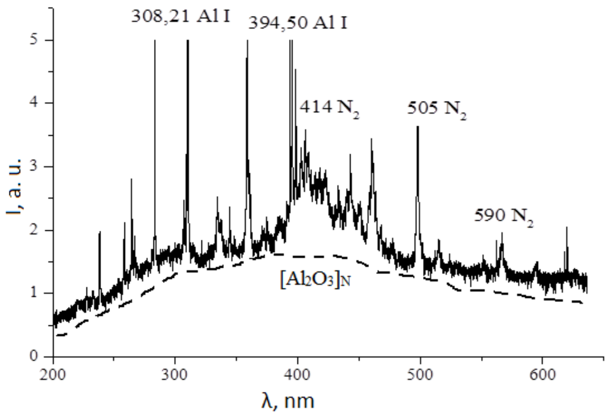

(2)

Figure 5. Radiation spectra of overstressed nanosecond discharge between aluminum electrodes in a mixture of nitrogen and oxygen: 13.3 (1) and 101.3 (2) kPa; p (nitrogen) - p (oxygen) = 100-1), dashed line - [Al_2O_3] N - designation of a large cluster or nanoparticle of aluminum oxide

The most intense spectral lines of the atom and singly charged ion of aluminum, which appeared in the spectra of plasma radiation based on mixtures of nitrogen and oxygen, were as follows: (256.8 + 257.5 + 257.5); 265.3; 394.4; 396.2 nm Al I; 236.5; (247.5 + 247.6); 286.9; 622.6; (623.1 + 624.3) nm Al II (Table 2). In addition to the spectral lines of aluminum, intense lines of the atom and singly charged nitrogen ion, as well as molecular

Table 2. Identification of the main spectral lines and emission bands of the plasma of an overstressed nanosecond discharge between aluminum electrodes on a mixture p (nitrogen) - p (oxygen) = 100 - 1 at a pressure of 101.3 kPa

nm	Particle	The configuration of the transition	Term	Lower energy level, eV	Upper energy level, eV
286.84940	Al II	3s3d-3s9p	1D-1P*	13.649400	17.970410
373.39030	Al II	3s4p-3s6s	3P*-3S	13.073080	16.392640
308.21	Al I	$3s_2(^1S)3p-3s_2(^1S)3d$	2P*-2D	0.000000	4.021485
390.06750	Al II	3s3p-3p2	1P*-1D	7.420707	10.598340
313.58500	Al II	3s4p-3s7s	1P*-1S	13.256460	17.209080
324.16000	Al I	3s2(1S)4d-3s3p(3P*)3d	2D-2F*	5.236819	9.060500
337.13	N_2	10-0			
344.36400	Al I	3s2(1S)3p-3s3p2	2P*-4P	0.013893	3.613246
348.26300	Al I	3s2(1S)nd-3s3p(3P*)3d	2D-2D*	4.826633	8.385690
364.92040	Al II	3s4p-3s5d	3P*-3D	13.071350	16.467950
365.10870	Al II	3s4p-3s5d	3P*-3D	13.073080	16.467930
387.00490	Al II	3s4f-3s13g	3F*-3G&1G	15.302550	18.505330
394.40060	Al I	3s2(1S)3p-3s2(1S)4s	2P*-2S	0.000000	3.142722
396.15201	Al I	3s2(1S)3p-3s2(1S)4s	2P*-2S	0.013893	3.142722
399.4997	N II				
402.63180	Al II	3s3d-3s6p	1D-1P*	13.649400	16.727880
402.63180	Al II	3s3d-3s6p	1D-1P*	13.649400	16.727880
405.67950	Al II	3s4d-3s15p	1D-1P*	15.472500	18.527850
405.94	N_2	8-0			

bands of the second positive system of nitrogen, were observed in such a plasma.

In the emission spectra of the plasma of an overstressed nanosecond discharge in mixtures of nitrogen with oxygen and a small admixture of aluminum vapor (Figure 5), broad emission bands were recorded with maxima in the spectral ranges of 390- 440 nm and 290- 300 nm. The highest emission intensity of these bands was observed at a pressure of a mixture of nitrogen and oxygen of 101 kPa. In mixtures based on argon, these bands were absent in the emission spectra of the discharge. Since a significant portion of nitrogen is present in the mixture under study, it is possible to expect the formation of nanostructures of aluminum nitrides in the studied plasma. But a comparison of the broadband emission spectra of the investigated discharge with the characteristic emission spectra of aluminum nitride nanostructures [12] showed that they are fundamentally different. In [13], characteristic electroluminescence spectra of anodic aluminum oxide are presented. The spectra in contact with solutions of different electrolytes were recorded at an oxidation current density of 5-15 mA / cm^2. These spectra were in the form of broad luminescence bands in the spectral range with maxima for different electrolytes in the spectral range of 480-550 nm. Proceeding from this, the most probable source of broadband radiation from the plasma of the discharge under investigation can be nanostructures of aluminum oxide.

In [6], it was noted that in the photoluminescence spectrum of anion-defect single crystals and nanostructured ceramics based on aluminum oxide, upon excitation of the corresponding samples by radiation with a wavelength of 205 nm, a broad emission band was observed with a maximum at a wavelength of 415 nm. This band coincides with that obtained in the present experiment. It is interpreted as a luminescence band of F centers (transition - 1S - 3P with a maximum emission spectrum at an energy of 3.0 eV and a decay time constant of 36 - 40 ms) [6,14]. In [6], the results of studying the cathodoluminescence spectra of nanostructured ceramics of aluminum oxide are also presented. Cathodoluminescence was excited by a pulsed electron beam with a density of 1 A cm^{-2}, an energy of 180 keV, and a duration of 3 ns. The spectrum of this cathodoluminescence was similar to the spectrum recorded in our experiment at a pressure of 101 kPa for a nitrogen-oxygen mixture. The main one was the emission band with a maximum at wavelengths of 410-420 nm (photon energy 3.0 eV), which was adjacent to a wider short-wavelength band with maxima of the photon energy at 3.4, 3.8, 4.3 eV [6]. The ultraviolet photo and cathodoluminescence bands of nanostructured aluminum oxide ceramics are associated with the radiation of F + - centers, which are created by oxygen vacancies and have a relatively short decay time (0.6 - 1.0 μs) [6,14].

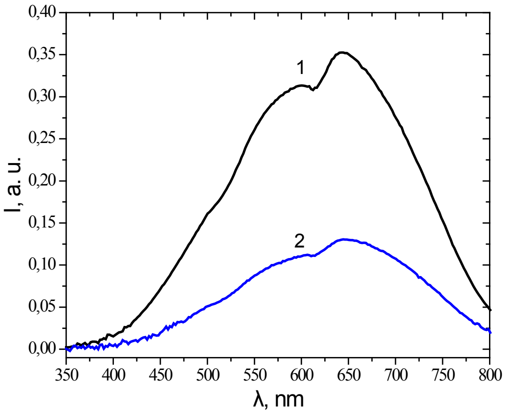

Figure 6. Transmission spectra of films based on copper and aluminum in the spectral region 350-800 nm (band lamp): 1 - clean glass substrate, 2 - film obtained by sputtering aluminum electrodes in a mixture of nitrogen and oxygen 100 - 1 kPa; the repetition rate of voltage and current pulses is 40 Hz, and the sputtering time is 3 h

As can be seen from Figure 6, the resulting film is characterized by weak transmission of radiation in the visible region of wavelengths. According to [15], films based on nanostructured ceramics made of aluminum oxide are practically opaque in the visible region of the spectrum, their transmission begins to increase in the spectral range of 0.8- 2.0 μm from 1-3 to 25%.

4. Plasma Parameters

The discharge plasma parameters for a mixture of aluminum vapor, oxygen, and nitrogen (component ratio 30: 1000: 100000 Pa) were determined numerically and calculated as total integrals of the electron energy distribution function (EEDF) in the discharge. EEDFs were found numerically by solving the kinetic Boltzmann equation in a two-term approximation. EEDF calculations were carried out using the program [16]. On the basis of the obtained EEDF, the mean energy of electrons, the mobility of electrons, the specific power losses of the electric discharge, and the rate constants of elastic and inelastic scattering of electrons by aluminum atoms, oxygen molecules and nitrogen molecules were determined, the ratio of which was (30: 1000: 100000) Pa depending on the value of the reduced electric field (the ratio of the electric field strength (E) to the total concentration of atoms of aluminum, molecules of nitrogen and oxygen (N)). The range of changes in the parameter E / N = 1-1000 Td ($1 \cdot 10^{-17}$ - $1 \cdot 10^{-14}$ V $\cdot$ cm^2) included the values of the parameter E/N, which were realized in the experiment. The following processes are taken into account in the integral of collisions of electrons with atoms and molecules: elastic scattering of electrons by aluminum atoms, excitation of energy levels of aluminum atoms (threshold energies 3.1707 eV, 2.9032 eV, 4.1463 eV, 4.2339 eV, 4.1296 eV, 5.1220 eV), ionization of aluminum atoms (threshold energy 6.0000 eV); elastic scattering and excitation of energy levels of oxygen molecules: vibrational (threshold energies: 0.190 eV, 0.380 eV, 0.570 eV, 0.750 eV), electronic (threshold energies: 0.977 eV, 1.627 eV, 4.500 eV, 6.000 eV, 8.400 eV, 9.970 eV, dissociative electron attachment (threshold energy - 4.40 eV) ionization (threshold energy - 12.06 eV); elastic scattering and excitation of energy levels of nitrogen molecules: rotational - threshold energy 0.020 eV, vibrational (threshold energy: 0.290 eV, 0.291 eV, 0.590 eV, 0.880 1.170, 1.470, 1.760, 2.060, 2.350; electronic: 6.170 eV, 7.000, 7.350, 7.360, 7.800, 8.160, 8.400, 8.550, 8.890, 11.03, 11.87, 12.25, 13.00, ionization (threshold energy - 15.60 eV). Data on the absolute values of the effective cross sections of these processes, as well as their dependences on the energies of electrons were taken from the databases [17,18] and works [19].

The electron concentration (N_e) was calculated using the well-known formula [16]:

$$N_e=j/e\cdot V_{dr.,}$$

where j is the current density in the discharge, e is the electron charge, V_{dr} is the electron drift velocity.

The drift velocity of electrons was determined from the expression [16]:

$$V_{dr}=\mu_e\cdot E,$$

where μe is the electron mobility, E is the field strength on the plasma.

The field strength on the plasma E was calculated by the formula:

$$E=U_{pl.}/d,$$

$U_{pl.}$ - plasma voltage, d-discharge gap.

The results of a numerical calculation of mean energies of electrons make it possible to determine their temperature in the gas-discharge plasma of the emitter from the well-known formula [16]:

$$\varepsilon=3/2\cdot kT,$$

where ε is the electron energy, k is the Boltzmann constant, T is the temperature in degrees Kelvin.

The mean energy of the discharge electrons increases almost linearly from 0.2271 eV to 15.93 eV with an increase in the E / N parameter from 1 Td to 1000 Td. For the range of reduced electric field strength 205 Td -820Td, at which experimental studies of the electrical and optical characteristics of the discharge were carried out, the mean electron energies varied within 5.116-13.41 eV. And their highest energies corresponded to values of 60.57- 241.3 eV.

The results of a numerical calculation of the mean energies of electrons make it possible to determine their temperature in the gas-discharge plasma of the emitter from the well-known formula [16]:

$$\varepsilon=3/2\cdot kT,$$

where ε is the electron energy, k is the Boltzmann constant, T is the temperature in degrees Kelvin.

It increases from 59345.6 K to 155.556 K when the E / N parameter changes from 205 Td to 820 Td, respectively.

The product of the electron mobility and the total concentration of atoms and molecules of the mixture, as follows from the data of numerical calculations, varies in the range 0.9466E + 24N - 0.6931E + 24N (1/m/V/s) with a change in the parameter E / N in the range 205 Td -820 Td, which gives the electron drift velocity values of $1.9\cdot 10^4$ m / s and $5.7\ 10^4$ m / s, respectively, for the field strength on the plasma of $5\cdot 10^6$ V / m and $2\cdot 10^7$ V / m, the value of the electron concentration $1.6\cdot 10^{20}\ m^{-3}$ - $1.1\cdot 10^{20}\ m^{-3}$ at a current density of $5.1\cdot 10^6 A/m^2$ ta l. 02 $\cdot 10^7 A/m^2$ on the surface of the electrode of the radiation source ($0.196\cdot 10^{-4}\ m^2$).

In Figure 5 and Table 2 show the lines of atoms and ions of aluminum, nitrogen bands that are present in the spectrum of an overstressed nanosecond discharge between aluminum electrodes in a mixture p (nitrogen) - p (oxygen) = 100 - 1 at a pressure of 101.3 kPa.

Figure 7 shows the dependences of the mean energy of electrons in the plasma of a vapor-gas mixture Al: O_2: N_2 = 30: 1000: 100000 Pa at a total pressure p = 101.030 kPa on the reduced electric field strength.

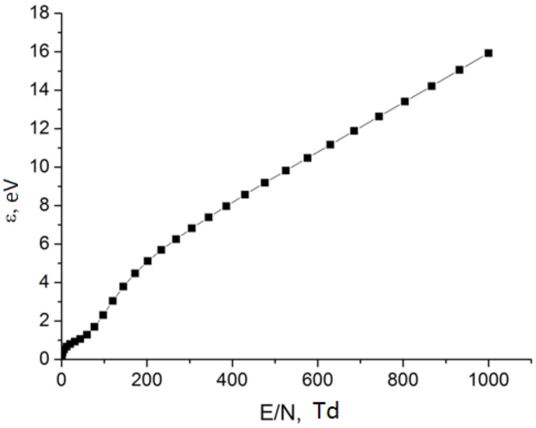

Figure 7. The dependences of the mean energy of electrons in the plasma of a vapor-gas mixture: 1-Al-O_2-N_2 = 30: 1000: 100000 Pa at a total pressure p = 101.030 kPa on the reduced electric field strength

DOI: https://doi.org/10.30564/jmmr.v3i2.2441

The mean energy of discharge electrons for a vapor-gas mixture aluminum-oxygen-nitrogen = 30: 1000: 100000 Pa increases almost linearly from 0.2271 eV to 15.93 eV (Figure 8), with an increase in the reduced electric field strength from 1 Td to 1000 Td. For the range of reduced electric field strength 205 Td - 820 Td, in which experimental studies of the electrical and optical characteristics of the discharge were carried out, the mean electron energies varied within 5.116-13.41 eV for this mixture. Their highest energies corresponded to values of 60.57- 241.3 eV.

Table 3 presents the results of calculating the transport characteristics of electrons: mean energies in ε, temperature T K, drift velocity $V_{dr.}$ and the concentration of electrons for a mixture of aluminum vapor with oxygen and nitrogen.

Table 3. Transport characteristics of plasma of an overstressed nanosecond discharge between aluminum electrodes in a mixture of nitrogen and oxygen: p = 101.325 kPa; p (nitrogen): p (oxygen) = 100-1)

E/N, Td	**Mixture: - Al -O_2-N_2 = 30: 1000:100000 Pa**			
	ε, eV	**T^0, K**	**$V_{dr.}$, m/s**	**N_e, m^{-3}**
205	5.116	59345	$1{,}9{\cdot}10^4$	$1{,}6{\cdot}10^{20}$
820	13.41	155556	$5{,}7\ 10^4$	$1{,}1\ {\cdot}10^{20}$

The temperature and drift velocities of electrons decrease from 155556 K to 59345 K and from 5.7 10^4 m / s to 1.9 · 10^4 m / s when the parameter E / N changes from 820 Td to 205 Td, respectively. The electron concentration values increase from 1.1 · 10^{20} m^{-3} to 1.6 · 10^{20} m^{-3} at a current density of 5.1 · 10^6 A / m^2 ta 1. 02 · 10^7A / m^2 on the surface of the radiation source electrode (0.196 · 10^{-4} m^2) for a given mixture.

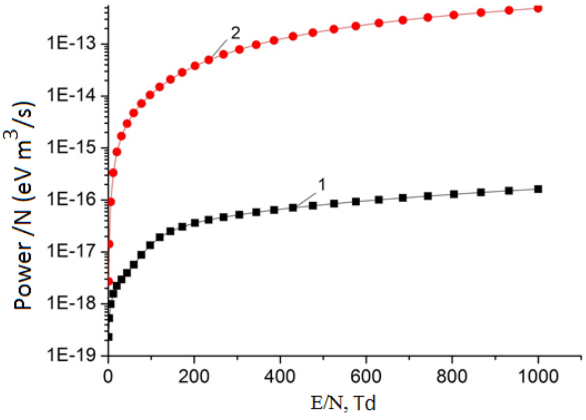

Figure 8. Specific discharge power for elastic (1) and inelastic (2) processes per unit of the total concentration of the mixture on the reduced electric field strength for a mixture of aluminum, nitrogen, oxygen

Table 4. A summary table of the values of the specific power of the discharge for elastic and inelastic processes per unit of the total concentration of the mixture at the experimental values of the reduced electric field strength for the mixture of aluminum, nitrogen, oxygen

E/N, Td	**Elastic, Power /N (eV m^3/s)**	**Inelastic, Power /N (eV m^3/s)**
205	3,612E-17	3,814E-14
820	1,294E-16	3,622E-13

Figure 8 presents the dependence of the specific powers of discharge losses for inelastic (2) and elastic (1) processes of collisions of electrons with the components of the mixture in a gas-discharge plasma on the reduced electric field strength. An increase in power is observed with increasing values of the reduced electric field, both for inelastic processes and for elastic ones. The specific powers for the reduced electric field strengths at which our experiments were carried out, have the following values: 3.612E-17 (eV m^3 / s) and 3.814E-14 (eV m^3 / s) for a reduced electric field equal to 205 Td, as well as 1.294E-16 (eV m^3 / s) and 3.622E-13 (eV m^3 / s) for a reduced electric field of 820 Td.

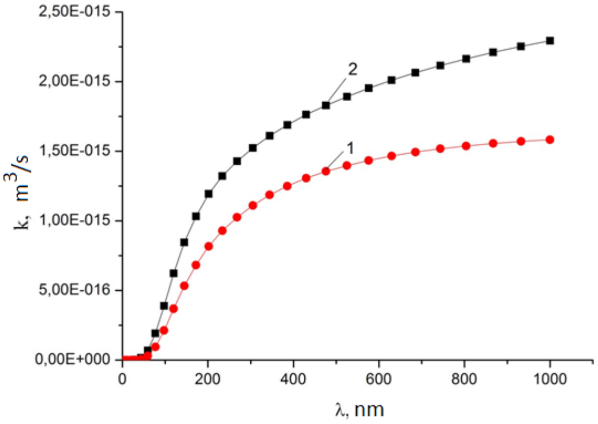

Figure 9. The dependences of the rate constants of collisions of electrons with aluminum atoms on the E / N parameter in plasma on a mixture of aluminum vapor, oxygen and nitrogen = 30: 1000: 100000 Pa at a total pressure of the mixture P = 101030 Pa: 1- excitation of the state of aluminum with a threshold energy 4.13 eV, 2- excitation of the state of aluminum with a threshold energy of 2.9 eV

Figure 9 presents the results of a numerical calculation of the dependence of the rate constants of collisions of electrons with aluminum atoms on the parameter E / N in a mixture of aluminum vapor, oxygen, and nitrogen for a ratio of partial pressures in a mixture of 30: 1000: 100000 Pa at a total mixture pressure P = 101030 Pa for two excitation processes states of aluminum with threshold energies of 4.13 and 2.9 eV, which correspond to the

DOI: https://doi.org/10.30564/jmmr.v3i2.2441

emission lines that are present in this mixture at 308.21 nm and 394.4 nm. In the range of reduced electric field strength 205 Td - 820 Td, at which experimental studies of the electrical and optical characteristics of the discharge were carried out, the rate constants of these processes are 0.8176E-15- 0.1556E-14 and 0.1194E-14- 0.2210E-14 m^3 / s.

Table 5. A summary table of the values of the rate constants of collisions of electrons with aluminum atoms at experimental values of the E / N parameter in plasma on a mixture of aluminum, oxygen and nitrogen vapors = 30: 1000: 100000 Pa at a total mixture pressure P = 101030 Pa

E/N, Td	394.4 nm	308.21 nm
205	0.1194E-14	0.8176E-15
820	0.2210E-14	0.1553E-14

5. Conclusions

Thus, it has been established that the plasma of an overstressed nanosecond discharge between aluminum electrodes at pressures of a mixture of nitrogen and oxygen (100-1) 50-101 kPa, a pulsed discharge power of 3-6.3 MW and an energy input of 110-153 mJ in one pulse is a source of luminescence nanoparticles of aluminum oxide in the form of a wide band, which is in the spectral range of 200-600 nm; during the deposition of the destruction products of electrodes and air molecules in plasma on a glass substrate, films based on aluminum oxides were obtained, which are characterized by low transparency in the visible region of the spectrum.

Numerical modeling of plasma parameters has established that for the range of reduced electric field strength 205 Td - 820 Td, at which experimental studies of the electrical and optical characteristics of the discharge were carried out, the mean electron energies varied within 5.116-13.41 eV, and their highest energies corresponded to values of 60.57- 241.3 eV. The value of the electron concentration was $1.6 \cdot 10^{20}$ m^{-3} - $1.1 \cdot 10^{20}$ m^{-3} at a current density of $5.1 \cdot 10^6$ A / m^2 and l. 02 $\cdot$ 10^7A / m^2 on the surface of the electrode of the radiation source ($0.196 \cdot 10^{-4}$ m^2). The excitation rate constants for two processes of excitation of the states of aluminum with threshold energies of 4.13 and 2.9 eV, which correspond to the emission lines that are present in this mixture at 308.21 nm and 394.4 nm in the range of reduced electric field strength 205 Td - 820 Td, at which experimental studies of electric and optical characteristics of the discharge were carried out are as follows 0.8176E-15- 0.1556E-14 and 0.1194E-14- 0.2210E-14 m^3 / s.

The specific powers for the reduced electric field strengths at which our experiments were carried out had the following values: 3.612E-17 (eV m^3 / s) and 3.814E-14 (eV m^3 / s) for a reduced electric field equal to 205 Td, as well as 1.294 E-16 (eV m^3 / s) and 3.622E-13 (eV m^3 / s) for the value of the reduced electric field equal to 820 Td.

References

[1] Bityurin V.A., Efimov A.V., Grigorenko A.V., Goryachev S.V., Klimov A.I., Chinnov V.F. Plasma stimulation of aluminum combustion in water vapour. Modern science, 2011, 2(7): 47-51. Available online at: http://modern.science.triacon.org/en/issues/2011/files/2011_2(7)_8.html

[2] Bityurin V.A., Grigorenko A.V., Efimov A.V., Klimov A.I., Korshunov O.V., Kutuzov D.T., Chinnov V.F. Spectral and kinetic analysis of a gas-discharge heterogeneous plasma in the flow of an Al, H2O, Ar mixture. High Temperature, 2014, 52(1): 3-13. Available online at: https://elibrary.ru/item.asp?id=21866675

[3] Mesyats G. A. Ecton- Electron Avalanche from metal. Usp. Fizich. Nauk, 1995, 165(6): 601-626.

[4] Walters J. P., Malmstadt H.V. Emission Characteristics and Sensitivity in a High-Voltage Spark Discharge. Analytical Chemistry, 1965, 37(12): 1484-1503. Available online at: https://pubs.acs.org/doi/abs/10.1021/ac60231a010

[5] Walters J. P. Source Parameters and Excitation in a Spark Discharge. Applied Spectroscopy, 1972, 26(1): 1484-1503. Available online at: https://www.osapublishing.org/as/abstract.cfm?uri=as-26-1-17

[6] Kortov V.S., Ermakov A.E., Zatsepin A.F., White M.A., Nikiforov S.V. et al. Features of luminescent properties of nanostructured aluminum oxide, Solid State Physics, 2008, 50(5): 916-920. Available online at: https://link.springer.com/article/10.1134/S1063783408050259

[7] Beloplotov D.V., Tarasenko V.F., Lomaev M.I. Luminescence of aluminum atoms and ions in a repetitively pulsed discharge initiated by runaway electrons in nitrogen. Optics of the atmosphere and ocean, 2016, 29, 2: 96-101. Available online at: https://www.sibran.ru/upload/iblock/f31/f310891d-5d0661a5c8090d5dbeddf328.pdf

[8] Shuaibov A.K., Minya A.I., Gomoki Z.T., Danilo V.V., Pinzenik P.V. Charachterristics of a High-Current Pulse Discharge in Air wich Ectonic Mechanism

of Copper Vapor Injection into a Disharge Gapr. Surface Engineering and Applied Electrochemistry, 2019, 55(1): 65-90. Available online at:
https://www.springerprofessional.de/en/characteristics-of-high-current-pulse-discharge-in-air-with-ecto/16681528

[9] Holovey V.M., Popovych K.P., Prymak M. V., Birov M.M., KrasilinetsV.M., Sidey V.I. X-ray induced optical absorption in $Li_2B_4O_7$ and $Li_2B_4O_7$:Cu single crystals and glasses. Physica B, 2014, 450: 34-38. Available online at:
https://www.sciencedirect.com/science/article/abs/pii/S0921452614004578

[10] Runaway electrons preionized diffuse discharge / Ed. by V.F. Tarasenko. New York: Nova Science Publishers Inc., 2014: 578.

[11] Beloplotov D. V., Tarasenko V. F. On the influence of a cathode shape on the parameters of current pulses of runaway electron beams in a gas discharge when applying voltage pulses with a rise time of 200 ns, Journal of Physics: 2019, 1393(012004): 7. Available online at:
https://iopscience.iop.org/article/10.1088 /1742-6596/1393/1/012004

[12] Silvera E., Freitas I.A., Glembocki O.J., Slack G.A., Schowalter L.J. Excitonic structure of bulk AlN from optical reflectivity and cathodoluminescense measurements. Phys. Rev., 2005, 71, (10): 041201-041204. Available online at:
https://journals.aps.org/prb/abstract/10.1103/PhysRevB.71.041201

[13] Egorov A.E., Chernyshev V.V. Electroluminescence spectra of anodic alumina in various electrolytes. Bulletin of Voronezh State University. Series. Physics mathematics, 2005(2): 8-10.

[14] Gasenkova I.V., Mukhurov N.I., Vakhioh Ya.M. Optical properties of anodized aluminum substrates as a basis for threshold detectors. Reports of BSUIR, 2016, 2(96): 114-118.

[15] Seredin P.V., Goloshchapov D.L., Lukin A.N., Bondarev A.D., Lenshin A.S. et al. Structure and optical properties of Al2O3 thin films obtained by reactive plasma sputtering on GaAs substrates (100). Physics and technology of semiconductors, 2014, 48(11): 1564-1569. Available online at:
https://link.springer.com/article/10.1134%2FS1063782614110256

[16] BOLSIG+ Electron Boltzmann equation solver. Available online at:
http:/www.bolsig.laplace.univ-tlse.fr.

[17] Content and usage of the archive Available online at:
http://www.ioffe.ru/ES/Elastic/data2.html

[18] Electron-Impact Cross Sections for Ionization and Excitation Database . Available online at:
https://physics.nist.gov/cgi-bin/Ionization/ion_data.php?id=AlI&ision=I&initial=&total=Y

[19] Shimon L.L. Influence of autoionization states on the population of energy levels of atoms of the aluminum subgroup. Scientific Bulletin of UzhNU. Physics Series, 2007, 20: 56-61.

DOI: https://doi.org/10.30564/jmmr.v3i2.2441

BILINGUAL PUBLISHING CO.
Pioneer of Global Academics Since 1984

Journal of Metallic Material Research
https://ojs.bilpublishing.com/index.php/jmmr

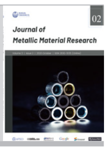

ARTICLE

Tetrahydro-dibenzo[a,d] Annulene-5, 11-Dihydrazone and Magnesium Oxide Used to Control the Corrosion of Aluminium in Chloride Ions Environment

Rajesh Kumar Singh* **Jay Prakash Singh** **Dharmendar Kumar**

Department of Chemistry, Jagdam College, J P University, Chapra, 841301, India

ARTICLE INFO

Article history
Received: 21 September 2019
Accepted: 27 October 2019
Published Online: 30 November 2020

Keywords:
Chloride ions
Aluminium
Corrosion
Electrospray
Thermal parameters
Marine environment

ABSTRACT

Chloride ions interact with aluminium in marine atmosphere to form corrosion cell. Due to this corrosion reaction occurs on their surface, aluminium is oxidized into Al^{3+}. The corrosion reaction accelerates deterioration in metal and it produces galvanic, pitting, stress, crevice, intergranular corrosion. Chloride ions decrease internal and external strength of aluminium metal. It is a very important metal so used in different appliances for e.g. road, water, air transports, housing, railways and other fields. Nanocoating and electrospray techniques used to check the corrosion of aluminium metal. For nanocoating and electrospray materials applied tetrahydro-dibenzo[a,d] [7] annulene-5, 11-dihydrazone and MgO. Both materials formed composite barrier and developed a passive surface for Cl^- ions. This barrier reduced the corrosion rate of aluminium. Nozzle spray and chemical vapour deposition technique used for coating process. The corrosion rate of metal was determined by gravimetric method. Corrosion potential and current density were calculated by potentiostat. The composite barrier formation was confirmed by activation energy, heat of adsorption, free energy, enthalpy and entropy. These thermal parameters were obtained by Arrhenius equation, Langmuir isotherm and Transition state equation. The adsorption of tetrahydro-dibenzo[a,d] [7] annulene-5,11-dihydrazone and MgO electrospray on aluminium surface was depicted by Langmuir, Frundlich and Temkin isotherm. The results of surface coverage area and coating efficiency were noticed that both materials were mitigated the corrosion rate of aluminium in chloride ions environment.

1. Introduction

Metals produce their corroding process in presence of acids [1], bases [2], salts [3], humidity [4], heat [5], temperature [6], pollutants [7], effluents [8] and particulates [9]. They also corrode when their internal morphology [10] can be change. Metals are surrounded by these hostile environments to form corrosion cell [11] and create dissolution on their surface. Corrosion chemists used several types of techniques to control the corrosion of materials like metallic [12] and nonmetallic coating [13] such coatings have done in acidic or basic medium. Cathodic protection [14] methods applied to protect metals corrosion in remote areas. Anodic protection [15] methods used in to control the corrosion of underground buried pipe. Various types of in-

---

**Corresponding Author:*
Rajesh Kumar Singh,
Department of Chemistry, Jagdam College, J P University, Chapra, 841301, India;
Email: rks_jpujc@yahoo.co.in

DOI: https://doi.org/10.30564/jmmr.v3i2.2403

hibitors [16] like organic and inorganic compounds provided ambient environment for corrosive substances. Organic compounds used as anodic, cathodic and mixed inhibitors [17] as per nature of corrosive of medium. The affect of corrosion mitigated by change the shape and size of metals as surrounding environment. Polymeric lamination [18] checked corrosion of materials in some corrosive environment. The attack of pollutants on materials protected by the application of paint coating. Conversion coating [19] can be alter outer face of metal and produced passive layer against effluents or pollutants. Thermal coating [20] can be done for metal which worked at high temperature. Top layer coating [21] stopped corrosion reaction in acidic medium. The metals shaved by the utility of hot dip coating [22] , flame spraying [23], cladding and chemical vapour deposition. Biological corrosion [24] controlled by sparing of nitrogen and sulphur containing functional organic compounds. The aluminium corrosion suppressed by nanocoating of tetrahydro-dibenzo[a,d] [7] annulene-5,11-dihydrazone such coating can be developed lot of porosities on the surface of base metal. Pollutants entered inside metal through diffusion or osmosis process and accelerate corrosion reaction. These porosities blocked by MgO by electrospraying method thus nanocoating and electrospray materials formed composite barrier that is worked as passive barrier for chloride ion environment. The coating and electrospray compounds concentration used 40 mM and 20 mM.

2. Experimental

Gravimetric method used to determination of corrosion rate: The sample of aluminium cut into (3X5X0.1) cm^2 and its outer layer rubbed with emery paper. It washed with acetone and dried with hot air gun. The corrosion rate of aluminium calculated at 283, 293, 303, 313 and 323 K temperature and these temperatures dipping duration of sample 10, 20, 30, 40 and 50 days in chloride ions solution. The sample kept into 10 M sodium chloride solution and the corrosion rates were determined above mentioned temperatures and days without coating and with coating nanocoating of tetrahydro-dibenzo[a,d] [7] annulene-5,11-dihydrazone and MgO electrospray.

Potentiostat Techniques: Potentiostat 173 model EG & PG Princeton model used to obtain the results of corrosion electrode potential and corrosion current density. Aluminium metal kept between calomel electrode and Pt reference and these electrodes connected with wire thus external current is flowing. The corrosion electrode potential and current density recorded without coating and with coating tetrahydro-dibenzo[a,d] [7] annulene-5,11-dihydrazone and MgO electrospray in chloride ions medium.

Coating compound tetrahydro-dibenzo[a,d] [7] annulene-5,11-dihydrazone synthesized by following methods: Indanone was added in cold solution of phosphorus pentachloride in presence of benzene solvent and the reaction mixture was stirred for 1hour. After work up the received yield was 87% of 3-chloro-1H-indene.

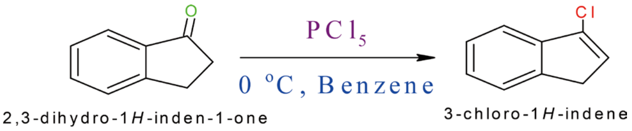

3-Chloro-1H-indene treated with potassium t-butaoxide solution and during completion of reaction mixture temperature was maintained 0^0C. The reaction mixture was stirred for two hours then cyclohexene was added which trapped 2, 3-didehydro-1H-indene and produced 2,3-cyclohexane-indene of 86% yield.

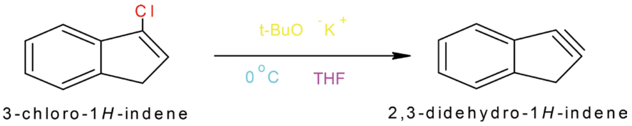

When 2,3-didehydro-1H-indene treated with cyclohexene, it is trapped with cyclohexene to give , 2,3-cyclohexane-indene.

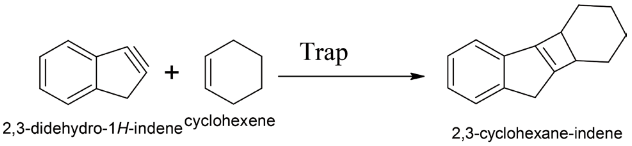

2,3-cyclohexane-indene was oxidized with NaIO$_4$ and RuO$_2$ in the presence of methylnitrile, carbon tetrachloride and water to give tetrahydro-dibenzo[a,d] [7] annulene-5,11-dione.

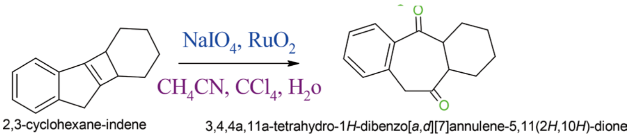

When tetrahydrodibenzo[a,d] [7] annulene-5,11-dione was refluxed with hydrazine in presence of ethyl alcohol to give tetrahydrodibenzo[a,d] [7] annulene-5,11-dihydrazone.

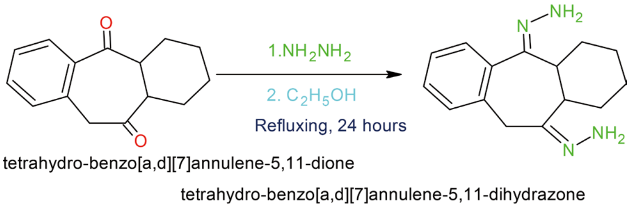

3. Results and Discussion

Aluminium comes in contact of chloride ions to produce galvanic, pitting, stress, crevice and intergranular

DOI: https://doi.org/10.30564/jmmr.v3i2.2403

corrosion. Such types of corrosion were controlled by the nanocoating of tetrahydro-dibenzo[a,d] [7] annulene-5,11-dihydrazone and electrospray of MgO.

Tetrahydro-dibenzo[a,d] [7] annulene-5,11-dihydrazone and MgO corrosion protection with time: The corrosion rate of aluminium was obtained without coaing and coating with tetrahydro-dibenzo[a,d] [7] annulene-5,11-dihydrazone and MgO by formula K_1 (mmpy) = (13.56) W_M / D_M A_M t (where W = weight loss of metal in kg, A = Area of metal in square meter, D = Density of metal in kg/ m^3, t=exposure time in hours) in chloride ions environment. The values of corrosion of aluminium were mentioned in Table 1. Figure 1 graph was plotted between K_M (corrosion rate) versus t (days) found to be straight line. The results of Table 1 and the plot of Figure 1 were shown that corrosion rate of aluminium increased without coating but their values decreased with nanocoating and electrospray of tetrahydro-dibenzo[a,d] [7] annulene-5,11-dihydrazone and MgO compounds. Polymeric-coated Al was nanocoated with tetrahydro-dibenzo[a,d][7]annulene-5,11-dihydrazone thus it developed protection barrier on its surface and on that barrier MgO electrospray used in this methods composite surface film generated. It stopped osmosis of diffusion process of chloride ions.

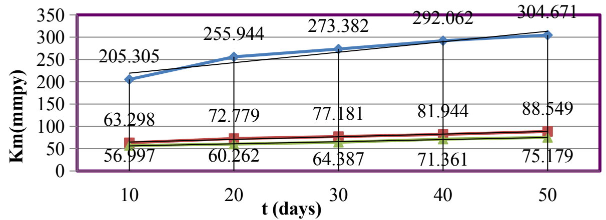

Figure 1 K Vs t of polymeric-coated Al with nanocoating of N_2 & MgO

Aluminium corrosion rate without and with coating of tetrahydro-dibenzo[a,d] [7] annulene-5,11-dihydrazone and MgO at different temperatures: The corrosion rate of aluminium was calculated at 283, 293, 303, 313 and 323^0K temperatures in absence and presence of tetrahydro-dibenzo[a,d] [7] annulene-5,11-dihydrazone and MgO electrospray. The recorded corrosion rate was written in Table1 which indicated that corrosion rate increased at lower to higher temperature but their values were reduced after coating of nanocoating and electrospray materials. Such trends were clearly observed in Figture 2 which was plotted between logK versus 1/T.

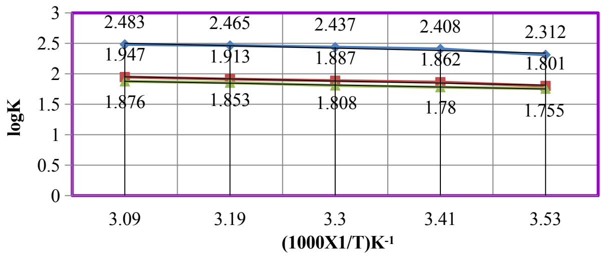

Figure 2 logK Vs 1/T for polymeric-coated Al with nanocoating of NC(2) & MgO

The values of log (**ɵ**/1-**ɵ**) for aluminium in tetrahydro-dibenzo[a,d] [7] annulene-5,11-dihydrazone and MgO: The values of log(ɵ/1-ɵ) for nanocoating of tetrahydro-dibenzo[a,d] [7] annulene-5,11-dihydrazone and MgO were given in table4.13.1 at 283, 293, 303, 313 and 323^0K temperature. It observed that their values were decreased as temperatures rising. In case with electrospray material got same types of results. Such types of trends clearly noticed in Figure 3 which was plotted between log(ɵ/1-ɵ) verse 1/T. MgO dispersed into marix of tetrahydro-dibenzo[a,d] [7] annulene-5,11-dihy-

Table 1. Corrosion rate of aluminium without and with coating of tetrahydro-dibenzo[a,d] [7] annulene-5,11-dihydrazone and MgO electrospraying of MgO in chloride ions environment

N & E	Temp(K)	283K	293K	303K	313K	323K	C(mM)
	Time(days)	10	20	30	40	50	
No	K_{m0}	205.305	255.974	273.798	292.062	304.671	00
	$\log K_{m0}$	2.312	2.408	2.437	2.465	2.483	
N_2	K_m	63.298	72.779	77.181	81.944	88.549	40
	$\log K_m$	1.801	1.862	1.887	1.913	1.947	
	$\log(K_m/T)$	1.253	1.329	1.368	1.409	1.457	
	$ɵ_m$	0.6916	0.7156	0.7181	0.7194	0.7079	
	$(1-ɵ_m)$	0.3084	0.2844	0.2819	0.2806	0.2921	
	$\log(ɵ_m/1-ɵ_m)$	0.351	0.401	0.406	0.408	0.384	
	% CE(m)	69.16	71.56	71.81	71.94	70.79	
E_{MgO}	K_m	56.997	60.262	64.387	71.361	75.179	20
	$\log K_m$	1.755	1.780	1.808	1.853	1.876	
	$\log(K_m/T)$	1.208	1.247	1.290	1.349	1.386	
	$ɵ_m$	0.7223	0.7645	0.7648	0.7556	0.7532	
	$(1-ɵ_m)$	0.2777	0.2355	0.2352	0.2449	0.2468	
	$\log(ɵ_m/1-ɵ_M)$	0.415	0.511	0.512	0.490	0.484	
	%CE (m)	72.23	76.45	76.48	75.56	75.32	

DOI: https://doi.org/10.30564/jmmr.v3i2.2403

drazone and increased the values of $\log(\theta/1-\theta)$.

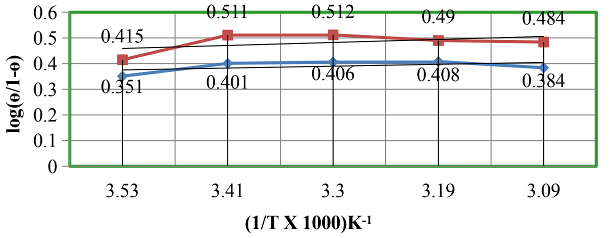

Figure 3 $\log(\theta/1-\theta)$ Vs 1/T for aluminium with nanocoating of N_2& MgO

Surface coverage area on aluminium by tetrahydro-dibenzo[a,d] [7] annulene-5,11-dihydrazone and MgO: Surface coverage area accommodated by tetrahydro-dibenzo[a,d] [7] annulene-5,11-dihydrazone and MgO electrospray were calculated by equation, $\theta_m = (K_{mo}-K_m/K_{mo})$ and its values were recorded in Table1. Figure 4 plotted between θ_m(surface coverage area) versus T(temperature) indicated that electrospray of MgO enhanced the capability of surface as temperature increased. Nanocoating and electrospray compounds formed a stable barrier which blocked the osmosis or diffusion process of corrosive pollutants.

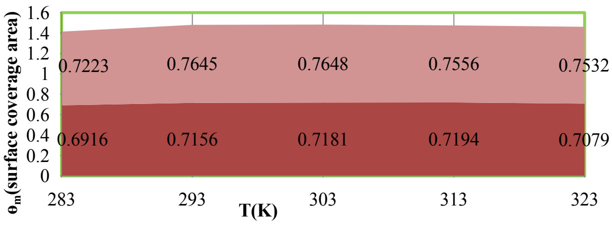

Figure 4 θ_m Vs T aluminium with N_2& MgO electrospray

Percentage of coating efficiency of tetrahydro-dibenzo[a,d] [7] annulene-5,11-dihydrazone and MgO: The percentage coating efficiencies tetrahydro-dibenzo[a,d] [7] annulene-5,11-dihydrazone and electrospray of MgO were determined by formula $\%CE = (K_{mo}-K_m/K_{mo}) \times 100$ and their values were given in Table1. It observed that percentage coating efficiency enhanced coating with tetrahydro-dibenzo[a,d] [7] annulene-5,11-dihydrazone but it coated with MgO percentage coating efficiency developed more as shown in Figure5 which plotted between % CE(m) versus T (temperature). It noticed that at higher temperatures these compounds produced stable barrier.

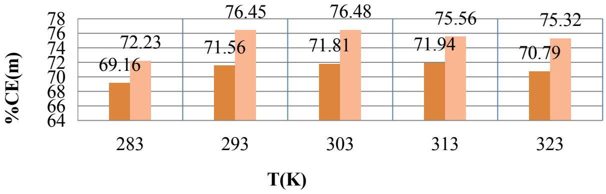

Figure 5 %CE(m) Vs T for aluminium with N_2& MgO electrospray

Activation energies of tetrahydro-dibenzo[a,d] [7] annulene-5,11-dihydrazone and MgO: Activation energies of these compounds were calculated at different temperatures by the use of Arrhenius equation $\log K_m = \log A - E_{ma}/2.303RT$ and Figure 2 plotted between $\log K_m$ versus 1/T and values were recorded in Table 2. Figure 6 graph plotted between E_{ma} (activation energy) versus T (temperature) noticed that activation energies of aluminium increased without coating after coating of tetrahydro-dibenzo [a,d] [7] annulene-5,11-dihydrazone and electrospraying of MgO its values were decreased. These results were noticed that both compounds formed chemical bonding with base metal. The results of Table 2 were shown that activation energies decreased as temperature enhanced but surface coverage area increased.

Table 2. Thermal parameters of aluminium without and with coating of tetrahydro-dibenzo[a,d] [7] annulene-5,11-dihydrazone and MgO in chloride ions environment

Thermal Parameters	283K	293K	303K	313K	323K
Ema	156.126	157.081	153.845	150.425	146.774
E_{2a}	121.619	121.464	119.124	116.740	115.091
q_2	-23.702	-26.158	-25.631	-24.898	-22.698
ΔG_2	-224.454	-220.778	-215.267	-209.678	-211.733
ΔH_2	-84.655	-86.711	-86.423	-86.028	-86.139
ΔS_2	-87.566	-90.173	-91.421	-92.696	-96.398
θ_{2m}	0.6916	0.7156	0.7181	0.7194	0.7079
Ea, MgO	118.513	116.115	114.137	116.740	110.893
q, MgO	-28.024	-33.334	-32.322	-29.902	-28.610
ΔG, MgO	-221.379	-215.432	-210.298	-206.013	-200.893
ΔH, MgO	-81.580	-81.364	-81.454	-82.363	-81.936
ΔS, MgO	-85.824	-87.036	-88.409	-90.400	-91.530
θ, MgO	0.7223	0.7645	0.7648	0.7556	0.7532

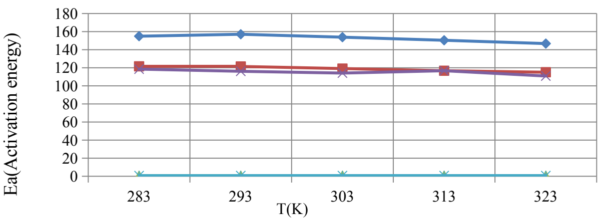

Figure 6 Ea Vs T for aluminium with nanocoating of N_2 & MgO electrospray

Heat of adsorption of tetrahydro-dibenzo[a,d] [7] annulene-5,11-dihydrazone and MgO electrospray: The heat of adsorption of both compounds were obtained by Langmuir equation $\log(\theta_m/1-\theta_m) = \log(A.C) - (q_m/2.303RT)$ (where T is temperature in Kelvin and q_m heat of adsorption) and Figure3. The negative sign of heat of adsorption depicted that nanocoating and electrospray compounds adsorbed by chemical bonding. The plot of Figure7 between q_m(heat of adsorption) verse T(temperature) with θ_m(surface coverage area) in-

DOI: https://doi.org/10.30564/jmmr.v3i2.2403

dicated as temperatures increased surface coverage area also enhanced.

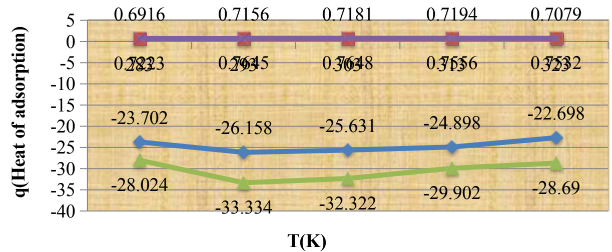

Figure 7 q_m Vs T, θ_m for aluminium with nanocoating of N_2& MgO electrospray

Free energy of nanocoating tetrahydro-dibenzo[a,d] [7] annulene-5,11-dihydrazone and MgO electrospray: The values of free energies of nanocoating and electrospray were calculated at various temperatures by formula $\Delta G_m = -2.303RT \log (33.3K_m)$ and their values were written in Table 2. It was observed that free energies of nanocoating and electrospray materials decreased when temperature rose from lower to higher. Free energies of both compounds indicated that they were attached with aluminium by chemical bonding. Figure 8 plotted between ΔG_m(free energy) versus T(temperature) , θ_m(surface coverage area) that graph was shown that free energies reduced and surface coverage area was enhanced.

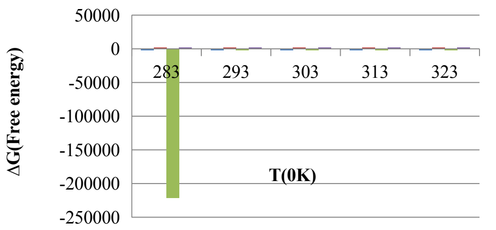

Figure 8 ΔG_m Vs T,θ_m for aluminium with nanocoating of N_2 & MgO electrospray

Enthalpy of nanocoating tetrahydro-dibenzo[a,d] [7] annulene-5,11-dihydrazone and MgO electrospray: Enthalpy of both compounds were determined by equation $K_m = R\ T / N\ h \log (\Delta S_m^{\#} / R) X \log (-\Delta H_m^{\#} / R\ T)$ and Figure 9. Their values were recorded in Table2. The results of Table2 indicated that both compounds coating process were exothermic. Figure9 the graph plotted between ΔH_m (enthalpy) versus T, θ_m for nanocoating and electrospray indicated that enthalpy decreased at lower to higher temperature then surface coverage increased. It confirmed that both compounds were attached with aluminium by chemical bonding. Enthalpy of values nanocoating and electrospray compounds were decreased so both compounds were formed a composite thin layer barrier. Enthalpy values found to be smaller with nanocoating and electrospray and increased surface coverage area as shown in Figure 10.

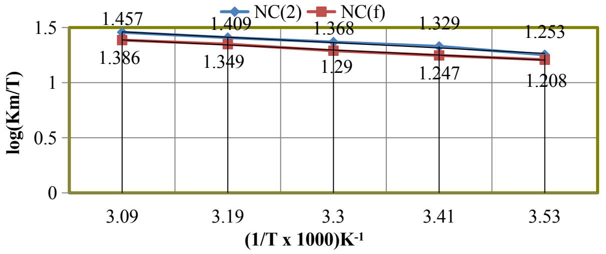

Figure 9 log(Km/T) Vs 1/T for aluminium with nanocoating of N_2 & MgO electrospray

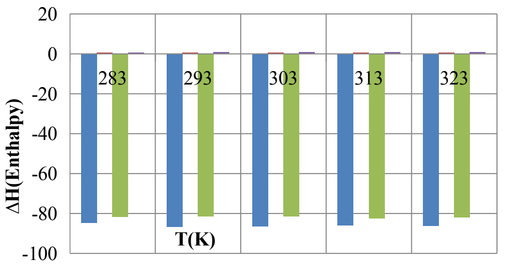

Figure 10 ΔH Vs T,θ for aluminium with nanocoating N_2 & MgO electrospray

Entropy of nanocoating tetrahydro-dibenzo[a,d] [7] annulene-5,11-dihydrazone and MgO electrospray: Entropy of nanocoating and electrospray compounds were calculated by $K_m = R\ T / N\ h \log (\Delta S_m^{\#} / R) X \log (-\Delta H_m^{\#} / R\ T)$ and their values were mentioned in Table2. Both compounds produced negative entropy which depicted a chemical bonding occurred between nanocoating and electrospray on aluminium metal. Figure 11 plotted between ΔS_m versus T, θ_m, it indicated entropy decreased then surface coverage area increased.

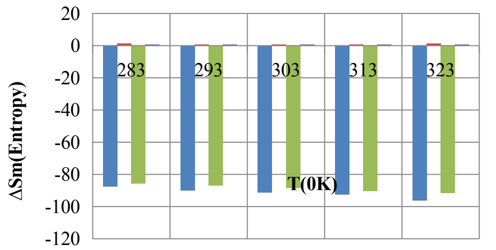

Figure11 ΔS_m Vs T,θ_m for aluminim with nanocoating N_2 & MgO electrospray

Potentiostat of nanocoating tetrahydro-dibenzo[a,d] [7] annulene-5,11-dihydrazone and MgO electrospray: Electrode potential and corrosion current of aluminium, tetrahydro-dibenzo[a,d] [7] annulene-5,11-dihydrazone and MgO electrospray were calculated by equation $\Delta E_m/\Delta I_m = \beta_a\ \beta c / 2.303\ I (\beta_a + \beta_c)$ and Tafel plot of Figure 12 plotted between ΔE_m(electrode potential) verse I(current density) and their values were expressed in Table3. These results were shown that electrode potential, corrosion current density and anodic polarization were enhanced without

DOI: https://doi.org/10.30564/jmmr.v3i2.2403

coating and decreased cathodic polarization. Nanocoating and electrospray compounds reduced electrode potential, corrosion current density and anodic polarization and increased cathodic polarization. The corrosion current of aluminium reduced by nanocoating of tetrahydro-dibenzo[a,d] [7] annulene-5,11-dihydrazone and MgO electrospray. MgO electrospray increased more current density with respect of nanocoating of tetrahydro-dibenzo[a,d] [7] annulene-5,11-dihydrazone. Both nanocoating and electrospray materials developed composite passive barrier on the surface of aluminium in chloride ions environment.

The corrosion current density of aluminium, nanocoating and electrospray were obtained by above mentioned equation and the values put in equation, K_{cr} (mmpy) = 0.1288 I (mA /cm^2) × Eq .Wt (g) / ρ (g/cm^3) to produce their corrosion rate. Their values were written in Table3 which clarified that corrosion increased without coating of aluminium but it reduced with nanocoating and electrospray. Nanocoating tetrahydro-dibenzo[a,d] [7] annulene-5,11-dihydrazone incrased coating efficiency and surface coverage area where as these values were more enhance by MgO electrospray. The corrosion rates of materials were obtained by weight loss experiment which satisfied the corrosion rate of potentiostat measurement technique.

Table 3. Potentiostat of aluminium nanocoating of tetrahydro-dibenzo[a,d] [7] annulene-5,11-dihydrazone and MgO electrospray

N & C	**ΔE_m (mV)**	**ΔI_m**	**β_a**	**β_c**	**I (mA/cm^2)**	**K_{cr} (mmpy)**	**$^{\theta}m$**	**% CE**	**C (mM)**
N(0)	-630	239	286	126	14.43	620.533	00	00	00
N_2	-255	72	45	157	4.29	184.471	0.7027	70.27	30
EMgO)	-221	62	40	167	3.94	169.420	0.7269	72.69	10

Mechanism of composite barrier formation: The organic compound tetrahydro-dibenzo[a,d] [7] annulene-5,11-dihydrazone possessed electron rich functional group hydrazone and aromatic ring and they chelated with aluminum to form complex compound. This compound developed lots of porosities on their surface that is blocked by MgO electrospraying. MgO entered into matrix of tetrahydro-dibenzo[a,d] [7] annulene-5,11-dihydrazone and formed a composite barrier. The composite barrier formation confirmed by the results of activation energy, heat of adsorption, free energy, enthalpy and entropy. The composite barrier of aluminium- tetrahydro-dibenzo[a,d] [7] annulene-5,11-dihydrazone-MgO worked as noble barrier against chloride ions environment.

4. Conclusion

The results of corrosion rate of aluminium were obtained by gravimetric and potentiostat techniques which indicated that corrosion rate and electrode potential increased without coating but their values were reduced by coating of tetrahydro-dibenzo[a,d] [7] annulene-5,11-dihydrazone and electrospraying of MgO. The surface coverage areas and percentage coating efficiencies produced by both compounds were shown that they had capability to adhere with aluminium. The coating of tetrahydro-dibenzo[a,d] [7] annulene-5,11-dihydrazone and electrospraying of MgO were an exothermic process. It confirmed by the values of free energy, enthalpy and entropy. Both compounds adsorbed on aluminium surface by chemical bonding to satisfy by the results of activation energy, heat of adsorption, free energy, enthalpy and entropy. The values of entropy indicated that both compounds were high stable on aluminium surface. The results of corrosion rate, surface coverage area, coating efficiency, corrosion potential, current density and thermal parameters values were depicted that tetrahydro-dibenzo[a,d] [7] annulene-5,11-dihydrazone and MgO were mitigated corroding effect of aluminium in chloride ions environment.

Acknowledgement

The UGC-New Delhi provided financial grant for research work. Author thanks financial supporting agency. I give my warm regards Professor Sanjoy Misra, Department of chemistry, R U Ranchi, Professor G Udaybhanu, Department of Applied chemistry, IIT (ISM), Dhanbad and Professor INN Namboothari, Department of Chemistry, IIT, Mumbai for their valuable suggestion and guidance. I am very thankful my departmental colleagues Dr. Sanjay Kumar and Dr. Raman Kumar Singh to help me data analysis graph plotting.

References

[1] R K Singh, Noor Alam. Study the corrosion & corrosion protection of brass sculpture by atmospheric pollutants in winter season. Modern Approach on Material Science, 2019, 1(3): 54-62.

[2] Szabo T, Molnar-Nagy L, Telegdi J. Self-healing microcapsules and slow release microspheres in paints. Progress in Organic Coatings, 2011, 72: 52-57.

[3] Videla H., L K Herrera. Understanding microbial inhibition of corrosion. Electrochem Acta, 2009, 39: 229-234.

[4] R K Singh. Corrosion protection of transport vehicles by nanocoating of Dechydrobenzo annulene-5,10-dihydrazone in corrosive environments and weather change. Journal of Powder Metallurgy and Mining, 2017, 6(1) 1-8.

[5] Wen N T, Lin C S, Bai C Y, Ger M D. Structures and characteristics of Cr (III) based conversion coatings

on electrogalvanized steels. Surf. Coat Technol, 2008, 203: 317.

[6] Boerio F J, Shah P. Adhesion of injection molded PVC to steel substrates, J of Adhesion, 2005, 81(6): 645-675.

[7] R K Singh, Manjay K Thakur, Sabana Latif. Mild Steel corrosion control by nanocoating and filler compounds in hostile environments. J of J Material Science, 2018, 4(3): 1-12.

[8] Deveci H, Ahmetti G, Ersoz M. Modified styrenes: Corrosion physico-mechanical and thermal properties evaluation. Prog. Org. Coat. 2012, 73: 1-7.

[9] Genzer J. Templating Surfaces with Gradient Assemblies. J of Adhesion, 2005, 81: 417-435.

[10] Leon-Silva U, Nicho M E. Poly(3-octylthiophhene) and polystyrene blends thermally treated as coating for corrosion protection of stainless steel 304. J. Solid State Electrochem, 2010, 14: 1487-1497.

[11] Baier R E. Surface behaviour of biomaterials: Surface for biocompatibility. J. Mater. Sci. Mater. Med., 2006, 17: 1057-1062.

[12] R K Singh. Corrosion protection of transport vehicles by nanocoating of decahydrobenzo annulene-5,10-dihydrazone and SiC filler in H2O, O2 (moist), CO2, SO2 environments and weather change. Journal of Metallurgy and Materials Science, 2016, 58:, 167-179.

[13] Rao BVA, Iqbal M Y, Sreehar B. Electrochemical and surface analytical studies of the self assembled monolayer of 5-methoxy-2-(octadeclthiol) benzimidazole in corrosion protection of copper. Electrochim, Acta, 2016, 55 620-631.

[14] Liu X Y, Ma H Y, Hou M Z. Self-assembled monolayers of stearic imidazoline on copper electrodes detected using electro chemical measurement, XPS, molecular simulation and FTIR. Chinese Sci. Bull., 2009, 54: 374-381.

[15] Liao Q Q, Yue Z W, Zhou Q. Corrosion inhibition effect of self-assembled monolayers of ammonium pyrrolidine dithiocarbamate on copper. Acta Phys. Chin. Sin., 2009, 25: 1655-1661.

[16] Zhang D Q, He X M, Kim G S. Arginine self-assembled monolayers against copper corrosion and synergitic effect of iodide ion. J. Appl. Electrochem, 2009, 39: 1193-1198.

[17] Ghareba G S, Omanovic S. Interaction of 12-aminododecanoic acid with a carbon steel surface: Towards the development of “green” corrosion inhibitors. Corrosion Sci., 2010, 52: 2104-2113.

[18] Sahoo R R, Biswas S K. Frictional response of fatty acids on steel. J. Colloid Interf. Sci., 2009, 333: 707-718.

[19] Raman R, Gawalt E S. Selfassembled monolayers of alkanoic acid on the native oxide surface of SS316L by solution deposition. Langmuir, 2007, 23: 2284-2288.

[20] R K Singh. Building materials corrosion control by fiber reinforced polymers. Journal of Powder Metallurgy and Mining, 2015, 4(2): 1-5.

[21] Li D G, Chen S H, Zhao S Y. The corrosion Inhibition of the self-assembled Au and Ag nanoparticles films on the surface of copper. Colloid. Surface A, 2006, 273: 16-23.

[22] Cristiani P, Perboni G, Debenedetti A. Effect of chlorination on the corrosion of Cu|Ni 70|30 condenser tubing. Electrochim. Acta, 2008, 54: 100-107.

[23] Cristiani P. Solutions fouling in power station condensers. Appl. Therm. Eng., 2005, 25: 2630-2640.

[24] R K Singh, Rajeev Kumar. Study corrosion and corrosion protection of stainless steel in phosphate fertilizer industry, American Journal of Mining and Metallurgy, 2014, 2: 27-31.

DOI: https://doi.org/10.30564/jmmr.v3i2.2403

BILINGUAL
PUBLISHING CO.
Pioneer of Global Academics Since 1984

Journal of Metallic Material Research

Aims and Scope

Journal of Metallic Material Research is a peer-reviewed, open-access journal dedicated to the research of metallic materials. As a critical component of the human civilization, metal has been infused into many aspects of our lives. The journal is focused on innovations in the research of metallic materials.

The scope of the Journal of Metallic Material Research includes, but is not limited to:

- Properties of metallic materials (Physical/Mechanical/Electrical/Chemical)
- Functions of metallic materials
- Applications of metallic materials
- Alloys
- Recycling

Bilingual Publishing Co. (BPC)

Tel:+65 65881289

E-mail:contact@bilpublishing.com

Website:www.bilpublishing.com

About the Publisher

Bilingual Publishing Co. (BPC) is an international publisher of online, open access and scholarly peer-reviewed journals covering a wide range of academic disciplines including science, technology, medicine, engineering, education and social science. Reflecting the latest research from a broad sweep of subjects, our content is accessible worldwide——both in print and online.

BPC aims to provide an analytics as well as platform for information exchange and discussion that help organizations and professionals in advancing society for the betterment of mankind. BPC hopes to be indexed by well-known databases in order to expand its reach to the science community, and eventually grow to be a reputable publisher recognized by scholars and researchers around the world.

BPC adopts the Open Journal Systems, see on ojs.bilpublishing.com

Database Inclusion

Asia & Pacific Science Citation Index

Creative Commons

China National Knowledge Infrastructure

Google Scholar

Crossref

MyScienceWork

BILINGUAL
PUBLISHING CO.
Pioneer of Global Academics Since 1984

Tel:+65 65881289
E-mail:contact@bilpublishing.com
Website:www.bilpublishing.com

ISSN 2630-5135
02
9 772630 513205
Price: S$30.00